Electron Identification with the TRT and the W Boson Mass Measurement at ATLAS

Thesis submitted for the degree of
Candidatus Scientiarum in Physics

by

Sascha Mehlhase

1st February 2007

Experimental High Energy Physics Group
Niels Bohr Institute
University of Copenhagen

Abstract

This thesis covers two physics analyses for the ATLAS experiment at CERN.
The first one, describing the mapping and optimisation of the electron identification in the TRT subdetector system, introduces new methods utilising the, so far unused, dE/dx information, carried in the time-over-threshold variable, as well as possible ways of combining this with the current algorithms. Based only on real data, its results will also be of use as input for a tuning of the Monte Carlo simulation of the system. Introducing a probability based approach for particle identification the overall pion rejection factor reaches value from 25 to 70. Especially at low energies an improvement, compared to the current method, of up to 300% is reached.
In the second analysis the systematic error in the W boson mass measurement, due to the theoretical description of real photons emitted by the final states in leptonic decays, is characterised. By observing the effect on parameters used for the mass measurement for successive theory improvements (orders in QED), the overall systematic error has been estimated to be about 8 MeV (5 MeV) for electrons (muons).

Contents

Chapter 1

Introduction

In the near future, starting 2008, the Large Hadron Collider (LHC) at CERN, the European Laboratory for Particle Physics, will be the centre of particle physics. The LHC, along with its four experiments, will allow physicist to do high energy physics in energy regimes and with statistics never seen before. The two major goals of the LHC experiments are to find the Standard Model (SM) Higgs particle, and therefore understand the mechanism of electroweak symmetry breaking to answer the question of how the elementary particles obtain their masses, and to discover possible new physics, like described in the Minimal Supersymmetric extension of the Standard Model (MSSM). Along with these measurements the LHC will provide precision measurements of a number of SM parameters, such as the top-quark mass. One very interesting SM parameter to be measured at the LHC is the mass of the W boson, since in addition to the verification of the SM predictions, it can be used to test the SM against a possible MSSM and to put a contraint on the SM Higgs or MSSM light-Higgs mass, respectively. Therefore it provides a cross check for the intended *direct* measurements of the Higgs boson mass. These direct Higgs boson searches will require, among other things, high-resolution measurements of electrons, photons and muons, as well as precise secondary vertex-detection for τ-leptons and b-quarks.

An overview on the SM, with a special emphasis on the electroweak sector and the physics of the gauge bosons, is given in Part I. Theoretical predictions for gauge boson masses will be derived on the basis of the SM and possible production mechanisms will be accosted. Common strategies for the measurement of the W boson mass will be explained.
One of the experiments at the LHC, designed to investigate a broad range of physics is the ATLAS detector. The two subsequent analyses in this thesis are based on this experiment, therefore a general overview on the design concept, including all its subdetectors, is given in Part II. The description, putting special emphasis on the detector parts used in the analyses, is prefixed by a short introduction to CERN and the LHC and perorated by a section on Monte Carlo (MC) detector simulation.
The two studies presented in Part III, describe the mapping and optimisation of the Particle Identification (PID) in the Transition Radiation Tracker (TRT), based on real data from the Combined Test Beam (CTB) runs, and the influence of Final State Radiation (FSR) on the W boson mass measurement. A proper electron identification, possibly achieved by using the results from the first study, is a key ingredient for a precise W boson mass measurement in the according channel ($W \to e\nu$). In addition it is essential, especially for low energy electrons, for the tagging/identification of b-quarks, used for direct Higgs boson searches. Another key

ingredient for an accurate determination of the W boson mass is the characterisation of the systematic errors. Within all systematics the effect of Final State Radiation (FSR) plays an increasing role, due to growing statistics reducing the effect of numerous other systematic errors, such as the lepton resolution and the boson recoil model.
The results of both studies are summarised in Chapter 8.

Part I

Physics

Chapter 2

The Standard Model

Most known and observed phenomena in particle physics are well described by the Standard Model (SM) of elementary particles and their fundamental interactions. The particles described within the SM can be divided into two types: fundamental (matter) particles and intermediate interaction particles. The first group, also referred to as fermions, carry a spin $s = 1/2$ and are grouped into leptons and quarks. Due to their spin, fermions can appear in $2s + 1 = 2$ states of spin projection or handedness (left and right-handed). The leptons, carrying an integral electric charge, and the quarks, carrying fractional electric charges, are again subdivided into three generations of two leptons and two quarks each (see Table 2.1). The quarks carry an additional quantum number, called colour, allowing each quark flavour to appear in three different states, denoted as $q_i, i = 1, 2, 3$. Since colour is a property not observed for any matter particles, quarks are forced to combine (hadronise) into *colourless* particles, called hadrons. These hadrons can consist of a quark-antiquark pair (mesons) or a combination of three quarks (baryons)[1]. Examples of a meson and a baryon are the π^+ $(u\bar{d})$ and the proton (uud), respectively.
All objects of our daily life's are build out of fermions of the first generation (e^-, u, d), whereas the particles of the other generations are only created in processes with high energy densities,

[1] Other combinations of quarks are possible, but much beyond the scope of this thesis.

Type \ Generation	1^{st}	2^{nd}	3^{rd}	Charge [|e|]
Lepton flavours	$\begin{pmatrix} e^- \\ \nu_e \end{pmatrix}_L$	$\begin{pmatrix} \mu^- \\ \nu_\mu \end{pmatrix}_L$	$\begin{pmatrix} \tau^- \\ \nu_\tau \end{pmatrix}_L$	-1 0
	$\bar{e_R}$	$\bar{\mu_R}$	$\bar{\tau_R}$	-1
Quark flavours	$\begin{pmatrix} u \\ d \end{pmatrix}_L$	$\begin{pmatrix} c \\ s \end{pmatrix}_L$	$\begin{pmatrix} t \\ b \end{pmatrix}_L$	$+2/3$ $-1/3$
	u_R	c_R	t_R	$+2/3$
	d_R	s_R	b_R	-1/3

Table 2.1: The three generations of the Standard Model fermions. There is an associated anti-fermion for each fermion, carrying the opposite charge. The left-handed and right-handed fields transform as doublets and singlets of $SU(2)_L$ respectively and are defined using the chirality operator γ_5 through: $l_L = \frac{1}{2}(1 - \gamma_5)l, l_R = \frac{1}{2}(1 + \gamma_5)l$.

Interaction	Gauge Bosons	Gauge Group	Mass [GeV/c^2]	Charge [|e|]	Range [m]	Acts on
Electromagnetic	photon (γ)	U(1)	0	0	∞	electric charge
Weak	$W^{\pm}$, Z^0	SU(2)	80.4, 91.2	±1, 0	10^{-18}	flavour
Strong	8 gluons (g)	SU(3)	0	0	10^{-15}	colour charge
Gravitation	graviton		0	0	∞	mass

Table 2.2: The fundamental interactions of the Standard Model and the force carrying bosons and their properties. As one of the four fundamental forces, gravitation, not being part of the Standard Model, is added.

such as in collider experiments, and decay into the members of the first. An overview on all lepton and quark flavours, including their electrical charge Q, is given in Table 2.1.
The second group of intermediate interaction particles, also referred to as bosons, are mediators of the fundamental interactions and carry an integral spin. The electromagnetic interaction, acting on electrical charged fermions, is mediated by the massless photon, γ. The mediators of the strong interaction are eight massless gluons, $g_\alpha, \alpha = 1..8$. The fact that the gluons carry colour charges themselves allows them to interact among each other and gives rise to effects like the colour confinement mentioned above. The bosons corresponding to the weak interaction are the three massive $W^{\pm}$ and Z^0 bosons, which because of their masses restrict this interaction to ranges below 10^{-18} m. Like the gluons, the bosons of the weak interaction are also self-interacting. The last fundamental interaction, the gravitational interaction, is not described by the SM and the predicted boson, called graviton[2] has not been experimentally observed. An overview on all fundamental interactions and their mediating bosons is given in Table 2.2.
From a theoretical point of view the SM is a quantum field theory (QFT) based on the gauge symmetry $SU(3)_C \times SU(2)_L \times U(1)_Y$. This gauge group contains both the symmetry group of strong interactions $SU(3)_C$ and the symmetry group of electroweak interactions $SU(2)_L \times U(1)_Y$. The latter one will be discussed in more detail in Section 2.2, since it is more relevant for this thesis. The symmetry group of the electromagnetic interaction, $U(1)_{em}$, is, by a unification with the weak interaction, included in the electroweak symmetry group.
In addition to this fermionic sector of the SM there is an unconfirmed scalar sector, indicated by the fact that the massive bosons of the weak interaction can only obtain their masses through a process of spontaneously symmetry breaking (SSB). In other words $SU(2)_L \times U(1)_Y$ is not a symmetry of the vacuum and is therefore broken down according to:

$$SU(3)_C \times SU(2)_L \times U(1)_Y \rightarrow SU(3)_C \times U(1)_{em}$$

The purely theoretical formalism responsible for the SSB, is called Higgs mechanism and provides the weak boson masses. Furthermore it introduces a new scalar and electrically neutral particle, the Higgs boson, that has not yet been observed, though indirect signs have been found [lep03].

[2]The graviton is expected to carry a spin $s = 2$.

2.1 Weak Interactions

The first evidence for weak interactions was found in nuclear β-decays ($n \to pe^-\bar{\nu}_e$) in 1930. The energy of the emitted electrons showed a continuous spectrum, which, assuming a two-body decay, would contradict energy conservation. To overcome this problem W. Pauli predicted the, at this time unknown, neutrino to be emitted together with the electron [Pau30][3]. In 1934, E. Fermi proposed a theory describing the β-decay as a four-fermion-point interaction (see Figure 2.1). In this approximation, which was later shown only to be valid at momentum transfers $q^2 \ll m_W^2$, he introduced the so-called Fermi constant $G_F = 1.167 \times 10^{-5} GeV^{-2}$, indicating the effective dimensionful coupling of the weak interactions, and the Lagrangian[4]

$$\mathcal{L} = -\frac{G_F}{\sqrt{2}} \left[\bar{p}(x)\gamma_\lambda n(x)\right] \left[\bar{e}(x)\gamma^\lambda \nu_e(x)\right] + h.c.$$

Due to the strict vector structure, the Fermi Lagrangian could not explain the parity violation observed in weak interaction.

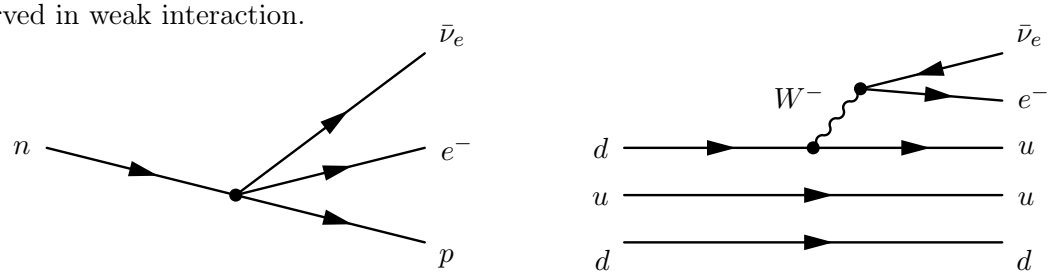

Figure 2.1: Nuclear β-decay in the four-fermion-point interaction model (left) and in nowadays model, including the intermediate W^- boson and the two spectator quarks (right).

2.1.1 Parity Violation and V-A Theory

The non-conservation of parity in weak interactions was proposed by Lee and Yang in 1956, after looking at data from several experiments [LY56]. Experimentally, parity violation was observed in 1957 by Wu *et al.* [W+57]. Looking at the nuclear beta decay of ^{60}Co nuclei ($^{60}Co \to {}^{60}Ni^* e^- \bar{\nu}_e$) in a magnetic field, they found a forward-backward asymmetry in the relative electron intensities, when measuring along and against the magnetic field. This implies a parity nonconservation, which could be explained by the fact that neutrinos, produced by charged currents, always occur in left-handed helicity states[5]. This restriction to the left-handed helicity states was shown experimentally by Goldhaber *et al.* in 1958 [G+58]. The fact that no right-handed neutrinos have been observed at all, indicates a maximal parity violation and thereby a vector minus axial vector (V-A)[6] structure for the charged weak current:

$$J_\mu \sim V_\mu - A_\mu = \bar{\psi}\gamma_\mu\psi - \bar{\psi}\gamma_\mu\gamma_5\psi$$

[3] Pauli originally named the particle neutron, which got changed into neutrino four year later by Fermi.

[4] The hermitian conjugate (h.c.) or conjugate transpose of an experession A in quantum mechanics is defined as $A^\dagger$. $(A^*)_{i,j} = \bar{A}_{j,i}$

[5] Anti-neutrinos always occur in right-handed helicity states. The discovery of neutrino-oscillations (e.g. [F+98]) suggest that this is only an approximation, albeit a very good one!

[6] Operators are categorised by their behaviour under Lorentz-transformation: Scalar (S) $\bar{\psi}\psi = \psi^\dagger\gamma_4\psi$, Four-vector (V) $\bar{\psi}\gamma_\mu\psi$, Tensor (T) $i\bar{\psi}\gamma_\mu\gamma_\nu\psi$, Axial four-vector (A) $\bar{\psi}\gamma_\mu\gamma_5\psi$, and Pseudo-scalar (P) $\bar{\psi}\gamma_5\psi$.

This restriction can also be seen when rewriting the leptonic current in terms of the field components:

$$J_\mu \sim V_\mu - A_\mu = \bar{\nu_e}\gamma_\mu(1-\gamma_5)e = 2(\bar{\nu_e})_L\gamma_\mu e_L$$

Following this structure E. Sudarshan introduced the V-A theory in 1957 [S+57] (published by R. Feynman and M. Gell-Mann in 1958 [FGM58]). This theory, based on Fermi's previous description, was able to explain the parity non-conservation, still handling the current-current interactions as being contracted to a single space-time point. The Lagrangian for the first two fermion generations, still characterising the coupling by the Fermi constant G_F, is given by[7]

$$\begin{aligned} \mathcal{L}_{V-A} &= -\frac{G_F}{\sqrt{2}} J_\mu^{CC}(x) J_\mu^{CC+}(x) \\ J_\mu^{CC} &= \bar{\nu}_e\gamma_\mu(1-\gamma_5)e + \bar{\nu}_\mu\gamma_\mu(1-\gamma_5)\mu + \bar{u}\gamma_\mu(1-\gamma_5)d' \end{aligned} \tag{2.1}$$

The V-A theory, describing the phenomenology of charged weak interactions reasonably well, became obsolete[8] with the discovery of uncharged (neutral) weak currents, in the Gargamelle bubble chamber experiment at the proton-anti-proton collider, at CERN in 1973 [H+73a][H+73b].

2.1.2 Intermediate Vector Boson Theory

Due to this discovery and following proposals for the existence of intermediate vector bosons for both charged [LRY49] and neutral weak interactions [Gla61], the Intermediate Vector Boson (IVB) theory was born. This theory predicts two charged ($W_\mu^\pm$) and one neutral (Z_μ) vector boson, corresponding to the charged current (CC) and the neutral current (NC), respectively. All of these vector bosons carry a spin $s = 1$. In difference to the V-A theory, current-current interactions are not described as a four-fermion point interaction, but by the propagation of the intermediate bosons. The Lagrangian of the IVB theory is given by

$$\begin{aligned} \mathcal{L}_{IVB} &= \underbrace{\frac{g}{\sqrt{2}}\left(J_\mu W^{\mu+} + J_\mu^+ W^{\mu-}\right)}_{\mathcal{L}_{CC}} + \underbrace{\frac{g}{\cos\theta_w} J_\mu^{NC} Z^\mu}_{\mathcal{L}_{NC}} \\ J_\mu &= \sum_l \bar{\nu}_l\gamma_\mu\frac{1}{2}(1-\gamma_5)l + \sum_q \bar{q}\gamma_\mu\frac{1}{2}(1-\gamma_5)q' \\ J_\mu^{NC} &= \sum_{f=l,q} g_L^f \bar{f}\gamma_\mu\frac{1}{2}(1-\gamma_5)f + \sum_{f\neq\nu} g_R^f \bar{f}\gamma_\mu\frac{1}{2}(1-\gamma_5)f \end{aligned} \tag{2.2}$$

The weak angle θ_w, defining the rotation from the weak eigenstates to the mass eigenstates, also relates the dimensionless weak coupling g to the electromagnetic coupling e through

$$e = g\sin\theta_w$$

Being able to explain e.g. the neutral currents observed in experiments and thereby an extension of the V-A formalism, the IVB theory still does not work at higher energies ($\sqrt{s} \gg m_W$). This is also due to the fact that both are non-renormalisable theories, violating unitarity at high energies[9].

[7] d' is the weak interactions d-quark eigenstate, related to the mass eigenstate by $d' = \cos\theta_c d + \sin\theta_c s$. With $\theta_c s$ being the so-called Cabibbo angle [Cab63].

[8] The V-A theory can still be applied as an effective theory at low energies ($\sqrt{s} < 300GeV$).

[9] At 1 TeV the WW cross-section go to infinity.

2.2 Electroweak Theory

In 1961 Glashow proposed $SU(2)_L \times U(1)_Y$ as the symmetry group for the electroweak interaction [Gla61], with the intention to unify the electromagnetic and weak interaction, containing the $U(1)_{em}$ symmetry group. In his proposal, four physical vector boson states ($W^{\pm}$, Z, and γ), obtained from rotations of the weak eigenstates, were included. At this point the masses m_W and m_Z were parameters to be put in by hand (i.e. measured by experiment) and the Lagrangian is essentially the one of the IVB theory (see Equation 2.2).
To illustrate this we consider the first generation component of the charged weak currents

$$J_\mu^+ = \bar{\nu}\gamma_\mu \frac{1}{2}(1-\gamma_5)e = \bar{\nu}_L \gamma_\mu e_L = \bar{l}_L \gamma_\mu \sigma_+ l_L \tag{2.3}$$

$$J_\mu^- = \bar{e}\gamma_\mu \frac{1}{2}(1-\gamma_5)\nu = \bar{e}_L \gamma_\mu \nu_L = \bar{l}_L \gamma_\mu \sigma_- l_L \tag{2.4}$$

written in the lepton doublet notation, using the Pauli matrices σ_i and the *step-up/down* operators $\sigma_\pm$ (see Table A.1)

$$l_L = \begin{pmatrix} v_L \\ e_L \end{pmatrix} \quad , \quad \bar{l}_L = \begin{pmatrix} \bar{v}_L & \bar{e}_L \end{pmatrix}$$

From this, the generators of the $SU(2)$ group can be found to be $T_i = \sigma_i/2$. While the first two generators are used to form the charged weak currents, the third one implies the formation of a neutral weak current

$$J_\mu^3 = \bar{l}_L \gamma_\mu \frac{1}{2}\sigma_3 l_L = \frac{1}{2}(\bar{\nu}_L \gamma_\mu \nu_L - \bar{e}_L \gamma_\mu e_L) \tag{2.5}$$

not to be mistaken for one of the two physical known neutral currents, J_μ^{em} and J_μ^{NC}. The group generated by all T_i is called the weak isospin group $SU(2)_L$. The group added for the unification was called the weak hypercharge group $U(1)_Y$. Having one generator $\frac{Y}{2}$, it implies a neutral weak hypercharge current, J_μ^Y, and a conserved weak hypercharge Y.
The relation between the electrical charge Q, the weak hypercharge Y and the weak isospin T_3 and thereby also for the associated currents is given by

$$Q = T_3 + \frac{Y}{2} \quad , \quad \underbrace{J_\mu^{em}}_{Q\bar{\psi}\gamma_\mu\psi} = \underbrace{J_\mu^3}_{T^3\bar{\psi}\gamma_\mu\psi} + \underbrace{J_\mu^Y}_{Y\bar{\psi}\gamma_\mu\psi} \tag{2.6}$$

Using (2.3) - (2.5) and Table 2.3 one can determine J_μ^Y and its orthogonal combination J_μ^{NC}

$$\begin{aligned} J_\mu^Y &= 2(J_\mu^{em} - J_\mu^3) = \underbrace{(-1)}_{Y(e_L)} \bar{e}_L \gamma_\mu e_L + \underbrace{(-2)}_{Y(e_R)} \bar{e}_R \gamma_\mu e_R + \underbrace{(-1)}_{Y(\nu_L)} \bar{\nu}_L \gamma_\mu \nu_L \\ J_\mu^{NC} &= \cos^2\theta_w J_\mu^3 - \sin^2\theta_w \frac{J_\mu^Y}{2} \\ &= \left(-\frac{1}{2} + \sin^2\theta_w\right) \bar{e}_L \gamma_\mu e_L + \left(\sin^2\theta_w\right) \bar{e}_R \gamma_\mu e_R + \left(\frac{1}{2}\right) \bar{\nu}_L \gamma_\mu \nu_L \end{aligned}$$

Lepton	$\mathbf{T}$	$\mathbf{T}^3$	Q	Y	Quark	$\mathbf{T}$	$\mathbf{T}^3$	Q	Y
ν_e	1/2	1/2	0	-1	u_L	1/2	1/2	2/3	1/3
e_L^-	1/2	-1/2	-1	-1	d_L	1/2	-1/2	1/3	1/3
					u_R	0	0	2/3	4/3
e_R^-	0	0	-1	-2	d_R	0	0	-1/3	-2/3

Table 2.3: Weak isospin ($\mathbf{T}$) and hypercharge (Y) quantum numbers of leptons and quarks in the first generation. The fermions in the other two generations have the same quantum numbers as the corresponding ones in the first generation. [HM84]

with θ_w being the weak angle.
The more general form of the weak currents,

$$J_\mu = \sum_f \bar{f}_L \gamma_\mu \sigma_+ f_L \tag{2.7}$$

$$J_\mu^Y = \sum_f Y_{f_L} \bar{f}_L \gamma_\mu f_L + \sum_f Y_{f_R} \bar{f}_R \gamma_\mu f_R \tag{2.8}$$

$$J_\mu^{NC} = \sum_f g_L^f \bar{f}_L \gamma_\mu f_L + \sum_{f \neq \nu} g_R^f \bar{f}_R \gamma_\mu f_R \tag{2.9}$$

$$J_\mu^{em} = \sum_f Q_f \bar{f}_L \gamma_\mu f_L + \sum_f Q_f \bar{f}_R \gamma_\mu f_R \tag{2.10}$$

$$J_\mu^3 = \sum_f T_3^f \bar{f}_L \gamma_\mu f_L \tag{2.11}$$

including contributions from all fermions and the weak neutral couplings $g_L^f = T_3^f - Q_f \sin^2\theta_w$ and $g_R^f = -Q_f \sin^2\theta_w$ finally leads to the electroweak interaction Lagrangian

$$\mathcal{L}_{int} = \underbrace{\frac{g}{\sqrt{2}}\left(J_\mu W^{\mu+} + J_\mu^+ W^{\mu-}\right)}_{\mathcal{L}_{CC}} + \underbrace{\frac{g}{\cos\theta_w} J_\mu^{NC} Z^\mu}_{\mathcal{L}_{NC}} + \underbrace{e J_\mu^{em} A^\mu}_{\mathcal{L}_{em}} \tag{2.12}$$

So far the theory is a gauge theory with a global $SU(2)_L \times U(1)_Y$ symmetry of the electroweak Lagrangian in (2.12) and includes three fermion quantum numbers Q, T_3 and Y (see Equation 2.6), four generators $T_i, i = 1,2,3$ and $\frac{Y}{2}$, and four gauge bosons $W_\mu^i, i = 1,2,3$ (weak bosons of $SU(2)_L$) and B_μ (hypercharge boson of $U(1)_Y$). To go from a global to a local symmetry, derivations are replaced by their covariant derivatives

$$D_\mu f = \left(\partial_\mu - i g_{\mathrm{SU(2)_L}} \mathbf{T} \cdot \mathbf{W}_\mu - i g_{\mathrm{U(1)_Y}} \frac{Y}{2} B_\mu\right) f \tag{2.13}$$

2.2.1 Spontaneously Symmetry Breaking and the Higgs Mechanism

Proposed by Y. Nambu in 1960 [Nam60] and proven by Goldstone in 1961 [Gol61][GSW62], the Goldstone theorem, stated that *massless scalars occur whenever a continuous symmetry*

of a physical system is "spontaneously broken" (or, more accurately, is "not apparent in the ground state") [HM84].
In 1966, P. W. Higgs introduced a mechanism for the spontaneous breakdown of gauge symmetries, like the electroweak local (gauge) symmetry $SU(2)_L \times U(1)_Y \to U(1)_{em}$, which is now referred to as the Higgs mechanism [Hig66].
Spontaneous symmetry breaking (SSB) is induced by a scalar field acquiring a vacuum expectation value (v.e.v.) different from zero. This gives rise, both to massive intermediate vector bosons and fermions, but also to a neutral scalar field, referred to as the Higgs particle.
Up to now this particle has not been observed in any experiment and it has to be mentioned that this so-called Higgs mechanism is not the only way to implement a symmetry breaking sector (SBS) into the SM.
To illustrate the process of SSB one can consider the Lagrangian of a scalar field, keeping only the first two possible terms in the expansion of the potential $V(\phi)$

$$\mathcal{L} = \frac{1}{2}\left(\partial_\mu \phi\right)^2 - \left(\frac{1}{2}\mu^2\phi^2 + \frac{1}{4}\lambda\phi^4\right) \tag{2.14}$$

In the case of $\lambda > 0$ and $\mu^2 > 0$ the ground state is $\phi = 0$ and the Lagrangian is symmetric, while at $\mu^2 < 0$ the Lagrangian has a negative mass term and two minima at $\phi = \pm\sqrt{-\mu^2/\lambda} = \pm v$. Including quatum fluctuations $\eta(x)$ around these minima, by applying $\phi(x) = v + \eta(x)$, the field translates to $\sqrt{-\mu^2/\lambda}$ and the Lagrangian (equivalent to $\mathcal{L}$) is then given by

$$\mathcal{L}' = \frac{1}{2}\left(\partial_\mu \eta\right)^2 - \lambda v^2\eta^2 - \lambda v\eta^3 - \frac{1}{4}\lambda\eta^4 + const. \tag{2.15}$$

where higher orders in η represent the interaction of the field with itself and a mass, "generated" by a SSB, can be extracted as

$$m_\mu = \sqrt{2\lambda v^2} = \sqrt{-2\mu^2} \tag{2.16}$$

2.2.2 The Symmetry Breaking Sector of the Electroweak Theory

It has to be mentioned that in this section only the simplest choice for a system Φ, responsible for the $SU(2)_L \times U(1)_Y \to U(1)_{em}$ breakdown in the SBS of the electroweak theory, will be outlined.
The system Φ has therefore been chosen to be a complex (isospin) doublet, carrying a hypercharge $Y = 1$. The self-interactions of Φ are given by the potential $V(\Phi)$, also responsible for the breaking described by a v.e.v. $\langle 0|\Phi|0\rangle \neq 0$. The according Lagrangian is called $\mathcal{L}_{SBS}$.

$$\begin{aligned} V(\Phi) &= -\mu^2\Phi^\dagger\Phi + \lambda\left(\Phi^\dagger\Phi\right)^2 \quad \text{with} \quad \lambda > 0 \\ \mathcal{L}_{SBS} &= \left(D_\mu\Phi\right)^\dagger\left(D^\mu\Phi\right) - V(\Phi) \end{aligned} \tag{2.17}$$

where,

$$\begin{aligned} \Phi &= \begin{pmatrix}\phi^+ \\ \phi_0\end{pmatrix} \quad \text{with} \quad \begin{matrix}\phi^+ \equiv \left(\phi_1 + i\phi_2\right)/\sqrt{2} \\ \phi_0 \equiv \left(\phi_3 + i\phi_4\right)/\sqrt{2}\end{matrix} \\ D_\mu\Phi &= \left(\partial_\mu - \frac{1}{2}ig\boldsymbol{\sigma}\cdot\mathbf{W}_\mu - \frac{1}{2}ig'B_\mu\right)\Phi \end{aligned}$$

Using the same notation as above, $\mathbf{W}_\mu$ and B_μ are the gauge fields and g and g' the according gauge couplings of $SU(2)_L$ and $U(1)_Y$ respectively. As introduced in the previous section the v.e.v. can have two possible solutions depending on the sign of $(-\mu)^2$.
In case $(-\mu)^2 > 0$ no symmetry is broken, since the minimum is at $\langle 0|\Phi|0\rangle = 0$ and therefore $SU(2)_L \times U(1)_Y$ symmetric. But in the case of $(-\mu)^2 < 0$ there is an infinite number of degenerated vacua, represented by an arbitrary $\arg\Phi$.

$$\langle 0|\Phi|0\rangle = \begin{pmatrix} 0 \\ v/\sqrt{2} \end{pmatrix} \quad \text{with} \quad v \equiv \sqrt{\mu^2/\lambda}$$

By choosing a random vacuum, e.g. $\arg\Phi \equiv 0$, the symmetry gets broken.
Summing up all information above, it is possible to write down the full SM Lagrangian, composed out of the fermion Lagrangian $\mathcal{L}_f$, the Lagrangian of the gauge fields $\mathcal{L}_G$, the SBS $\mathcal{L}_{SBS}$ Lagrangian and the Yukawa Lagrangian $\mathcal{L}_{YW}$.

$$\begin{aligned}
\mathcal{L}_{SM} = & \quad \textstyle\sum_f \bar{f} i \not{D} f & \longleftarrow \mathcal{L}_f \text{ using (2.13)} \\
+ & \quad -\tfrac{1}{4} W^i_{\mu\nu} W_i^{\mu\nu} - \tfrac{1}{4} B_{\mu\nu} W^{\mu\nu} + \mathcal{L}_{GF} + \mathcal{L}_{FP} & \longleftarrow \mathcal{L}_G \\
+ & \quad (D_\mu \Phi)^\dagger (D^\mu \Phi) + \mu^2 \Phi^\dagger \Phi - \lambda \left(\Phi^\dagger \Phi\right)^2 & \longleftarrow \mathcal{L}_{SBS} \text{ from (2.17)} \\
+ & \quad \lambda_e \bar{l}_L \Phi e_R + \lambda_u \bar{q}_L \tilde{\Phi} u_R + \lambda_d \bar{q}_L \Phi d_R + h.c. & \longleftarrow \mathcal{L}_{YW} \\
& \qquad + \text{other two generations}
\end{aligned} \tag{2.18}$$

Where $\mathcal{L}_G$ is written in terms of the field strength tensors $W^i_{\mu\nu} = \partial\mu W^i_\nu - \partial_\nu W^i_\mu + g\varepsilon^{ijk} W^j_\mu W^k_\nu$ and $B_{\mu\nu} = \partial_\mu B_\nu - \partial_\nu B_\mu$ and $\mathcal{L}_{YW}$ by using

$$l_L = \begin{pmatrix} \nu_L \\ e_L \end{pmatrix} \text{ and } q_L = \begin{pmatrix} u_L \\ d_L \end{pmatrix}.$$

$\mathcal{L}_{GF}$ and $\mathcal{L}_{FP}$ are the gauge fixing and Faddeev-Popov Lagrangian respectively, included for completeness but not relevant for the scope of this thesis.
Finally the masses of the vector bosons m_W and m_Z and of the fermions m_f, can be obtained from $\mathcal{L}_{SBS}$ and $\mathcal{L}_{YW}$ respectively. This will be illustrated for the vector bosons in the next section.

2.2.3 The Masses of the Gauge Bosons

Today's SM, including the phenomenological properties of previous theories, like the IVB theory discussed above, was formulated by S. Weinberg and A. Salam in 1967/68 [Wei67].
It is also a gauge theory based on the gauge symmetry of the electroweak interaction $SU(2)_L \times U(1)_Y$ and includes the four intermediate vector bosons ($W^\pm$, Z, and γ). But in difference to the IVB theory the gauge boson masses m_W and m_Z were not put in by hand, but are generated by the Higgs mechanism. By doing so the SM, and therefore the electroweak part of it, respects unitarity at all energies and is renormalisable.
A strong test for the accuracy of the SM was given with the discovery of the electroweak gauge bosons $W^\pm$ and Z at CERN in 1983 [UA183][UA283]. The masses of $W^\pm$ and Z can be derived from theory using the SM Lagrangian (2.18). Like illustrated in Section 2.2.1 the symmetry is broken by fixing a non-symmetric vacuum to e.g.

$$\langle 0|\Phi|0\rangle = \begin{pmatrix} 0 \\ \frac{v}{\sqrt{2}} \end{pmatrix}$$

The so-called physical spectrum (all particles and their corresponding masses) is produced by inducing *small oscillation* (by small fields $\boldsymbol{\xi}(x)$ and $H(x)$) around this value, described by

$$\Phi(x) = e^{i\frac{\boldsymbol{\xi}(x)\cdot\boldsymbol{\sigma}}{v}} \begin{pmatrix} 0 \\ \frac{v+H(x)}{\sqrt{2}} \end{pmatrix}$$

After performing certain gauge transformations (A.1) - (A.3) and applying the rotations (by the weak angle $\tan\theta_w \equiv \frac{g'}{g}$) between the mass eigenstates and the weak eigenstates:

$$\begin{aligned} W^{\pm}_{\mu} &= \frac{W'^{1}_{\mu} \mp i W'^{2}_{\mu}}{\sqrt{2}} \\ Z_{\mu} &= \cos\theta_w W'^{3}_{\mu} - \sin\theta_w B'_{\mu} \\ A_{\mu} &= \sin\theta_w W'^{3}_{\mu} + \cos\theta_w B'_{\mu} \end{aligned}$$

the masses (double underline) can be read from the SM Lagrangian (2.18)

$$\begin{aligned} (D_\mu\Phi)^\dagger (D^\mu\Phi) &= \underline{\underline{\left(\frac{g^2v^2}{4}\right)}} W^+_\mu W^{\mu-} + \frac{1}{2}\underline{\underline{\left(v^2\frac{g^2+g'^2}{4}\right)}} Z_\mu Z^\mu + \dots \\ V(\Phi') &= \frac{1}{2}\underline{\underline{(2\mu^2)}} H^2 + \dots \\ \mathcal{L}_{YW} &= \underline{\underline{\left(\lambda_e\frac{v}{\sqrt{2}}\right)}} \bar{e}'_L e'_R + \underline{\underline{\left(\lambda_u\frac{v}{\sqrt{2}}\right)}} \bar{u}'_L u'_R + \underline{\underline{\left(\lambda_d\frac{v}{\sqrt{2}}\right)}} \bar{d}'_L d'_R + \dots \end{aligned}$$

which finally yields the tree-level approximations

$$m_W = \frac{1}{2}vg \tag{2.19}$$

$$m_Z = v\frac{\sqrt{g^2+g'^2}}{2} \tag{2.20}$$

$$m_e = \lambda_e\frac{v}{\sqrt{2}} \quad , \quad m_u = \lambda_u\frac{v}{\sqrt{2}} \quad , \quad m_d = \lambda_d\frac{v}{\sqrt{2}} \quad , \dots \tag{2.21}$$

$$m_H = \sqrt{2}\mu \tag{2.22}$$

From (2.19), (2.20), $v \equiv \sqrt{\mu^2/\lambda}$, and $e = g\sin\theta_w = g'\cos\theta_w$ follows[10]

$$\frac{m_W}{m_Z} = \cos\theta_w \quad \Rightarrow \quad \rho^{tree} \equiv \frac{m_W^2}{m_Z^2\cos^2\theta_w} = 1 \tag{2.23}$$

To calculate the masses it is necessary to measure v and/or some SM parameters (α, G_F, $\sin^2\theta_w$) experimentally. This can be done by comparing the SM at low energies ($q^2 << m_w^2$) to e.g. the V-A theory, yielding the relations

$$\begin{aligned} \frac{G_F}{\sqrt{2}} &= \frac{g^2}{8m_W^2} = \frac{1}{2v^2} \\ m_W^{tree} &= \sqrt{\frac{\pi\alpha}{\sqrt{2}G_F}}\frac{1}{\sin\theta_w} \\ m_Z^{tree} &= \sqrt{\frac{\pi\alpha}{\sqrt{2}G_F}}\frac{1}{\sin\theta_w\cos\theta_w} \end{aligned} \tag{2.24}$$

[10] In agreement with the value measured experimentally by Kim *et al.* in 1981 [KLLW81].

The fine-structure constant α has been measured in atomic, molecular and nuclear physics experiments to be[11]

$$\alpha = 1/137.03599911 \pm 1/0.00000046 \quad \text{[PDG06]} \tag{2.25}$$

The Fermi constant G_F was obtained from μ-decay to be

$$G_F = (1.16637 \pm 0.00001) \times 10^{-5} GeV^{-2} \quad \text{[PDG06]} \tag{2.26}$$

while the weak-mixing angle $\sin^2\theta_w$ could be measured, e.g. in νN-scattering[12]

$$\sin^2\theta_w = 0.23122 \pm 0.00015 \quad \text{[PDG06]} \tag{2.27}$$

Inserting these values, the masses can be calculated at *tree level*, as

$$m_W^{tree} \approx 78 GeV \quad , \quad m_Z^{tree} \approx 89 GeV \tag{2.28}$$

For comparison, the present experimental values are

$$m_W^{exp} = (80.398 \pm 0.025) GeV \quad \text{[CDF07] and} \quad m_Z^{exp} = (91.1876 \pm 0.0021) GeV \quad \text{[PDG06]} \tag{2.29}$$

In difference to the gauge boson masses, the masses of the fermions and the newly introduced Higgs particle, may be included in, but are not predicted by the theory. The fermion masses are expressed in terms of the mass parameter v and the coupling constants, as given in (2.21) and have to be put into the model by hand, through experimental measurements.
The mass of the Higgs boson is given in 2.22 as a function of μ and is related to the mass parameter v through

$$\lambda = \frac{m_H^2}{2v^2}$$

Since the parameter μ is unknown, it is not possible to predict the Higgs boson mass directly. Including higher order contributions, by considering loop diagrams, changes relation (2.2.3) to

$$\rho^{tree} \equiv \frac{m_W^2}{m_Z^2 \cos^2\theta_w} \neq 1$$

and introduces a new term, related to the effects of radiative corrections ΔR, in the calculation of the W boson mass (see Equation 2.24) [TKTB01]

$$m_W = \sqrt{\frac{\pi\alpha}{\sqrt{2}G_F}} \frac{1}{\sin\theta_w \sqrt{1-\Delta R}} \tag{2.30}$$

The radiative corrections ΔR can be estimated by comparing the W mass, calculated at tree level, with the actual experimentally measured value. The tree level W boson mass is calculated (see Equation 2.24) using precision measurements of the Z boson mass m_Z, the Fermi constant G_F and the electromagnetic coupling constant α[13]. Within the SM the radiative corrections are caused by fermion loops as well as the Higgs boson loop. Since the

[11] At $q^2 = 0$. At $q^2 \approx m_W^2$ the value is $\sim 1/128$.
[12] Using the relation between the NC and CC cross-sections and the weak-mixing angle (Measured at the Z-pole, A.4)
[13] For this purpose α is calculated at $Q = m_Z$.

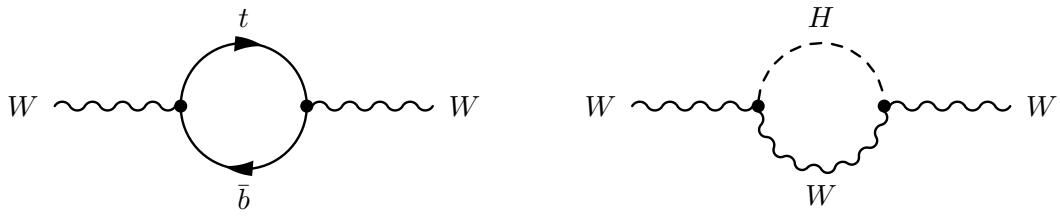

Figure 2.2: Lowest order radiative corrections to the W boson mass. The top quark mass affects the radiative corrections ΔR through $t\bar{b}$ quark loops (left) by $\Delta R \propto m_t^2$, while the Higgs boson mass only does by $\Delta R \propto \log m_H$.

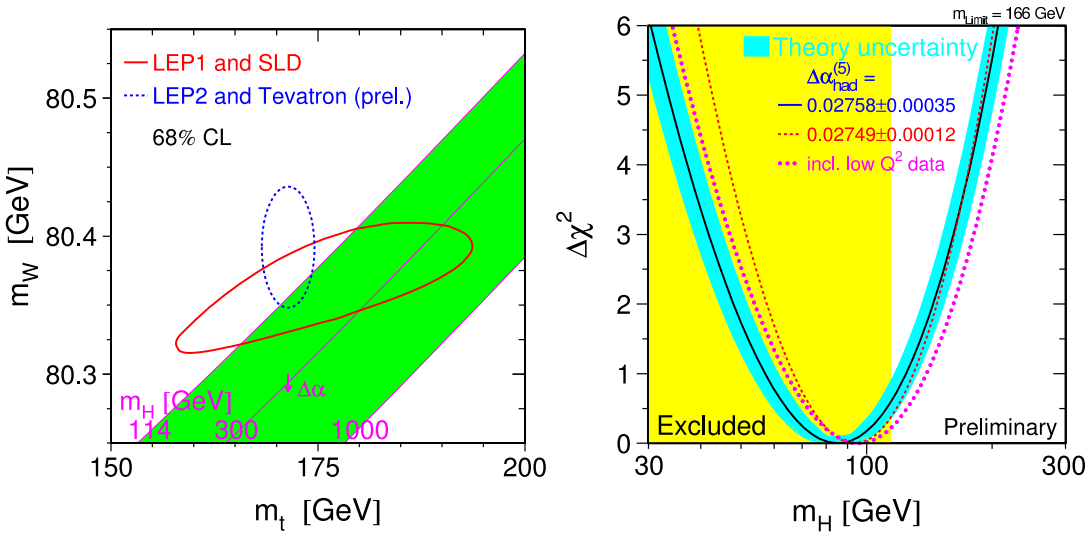

Figure 2.3: The plot on the left shows contraint on the Higgs boson mass based on the current measurements of m_t and m_W. The overlap between indirect (dashed red) and direct (solid blue) measurements indicates that a light Higgs boson is favoured. The plot on the right shows the $\Delta\chi^2$-curve derived from high-Q^2 precision electroweak measurements, performed at LEP and by SLD, CDF, and D0, as a function of the Higgs boson mass, assuming the Standard Model to be the correct theory of nature. The yellow background indicates the range excluded by direct measurements at LEP-2. [LE]

correction from the fermion loops depends on the difference in the squared fermion masses, the $t\bar{b}$ quark loop dominates this contribution. The Feynman diagrams for the two main loop contributions, the $t\bar{b}$ quark loop and the Higgs boson loop, are given in Figure 2.2. It can be shown that the radiative correction are proportional to the two masses like:

$$\Delta R \propto (\rho - 1) \propto m_t^2 \quad , \quad \Delta R \propto (\rho - 1) \propto \log m_H$$

Having a precision measurement of the top quark mass m_t, as performed at the Tevatron (see [PDG06] p. 516) or intended at ATLAS (see [TDR99a] p. 622), the W boson mass can be predicted within a range of 200 MeV depending on the assumed Higgs boson mass. Therefore the measurement of the W boson mass can provide a constraint to the Higgs boson mass. The constraint on the Higgs boson mass, based on the current measurements of m_t and

m_W, is illustrated in Figure 2.3 (left). To improve this constraint on the Higgs boson mass significantly, the precision on the W boson mass measurement has to be doubled roughly, for not being the decisive uncertainty compared to the top-quark mass. This means that Δm_W has to be reduced from about 25 MeV to below 15 MeV. Figure 2.3 (right) shows the $\Delta\chi^2$-curve derived from high-Q^2 precision electroweak measurements, performed at LEP and by SLD, CDF, and D0, as a function of the Higgs boson mass, assuming the SM to be the correct theory of nature. Values up to 114 GeV, including the minimum value of 85^{+39}_{-28} GeV, have already been excluded by direct measurements (yellow part) at the LEP-2 [LE]. In addition an accurate characterisation of the radiative correction, requirering a precise measurement of the W boson mass, might allow a disentanglement between the SM and a possible minimal supersymmetric extension of the SM (MSSM), since the latter one is expected to yield increased radiative corrections of up to 250 MeV [TKTB01].

Chapter 3

Physics of Electroweak Gauge Bosons

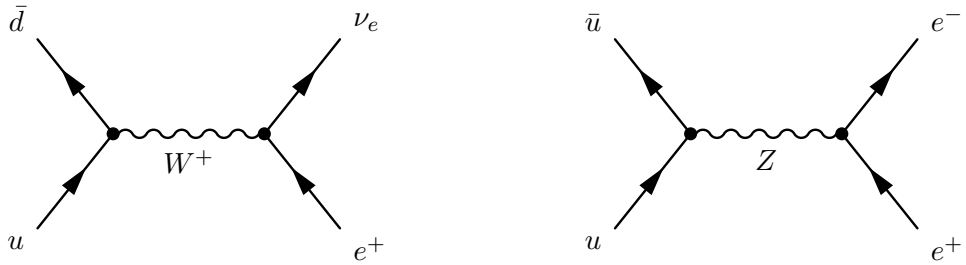

Figure 3.1: Lowest-order Feynman diagrams for the Drell-Yan processes $u\bar{d} \to W^+ \to e^+\nu_e$ and $u\bar{u} \to Z \to e^+e^-$.

The most important process for the production of electroweak gauge bosons is the so-called Drell-Yan process [DY70][DY71], which describes the production of lepton pairs through the decay of an intermediate boson, itself created in the annihilation of a quark and an anti-quark from a pair of interacting hadrons, protons in case of the LHC. Examples for the production of W and Z bosons, are illustrated in Figure 3.1 in terms of lowest order Feynman diagrams. Due to the relative movement of the partons inside the protons, only a fraction of the centre-of-mass energy s of the protons is available for the creation of particles. The actual invariant mass of the parton system $\hat{s}$ can be estimated, using the four-momenta of the protons, p_1 and p_2, and the momentum fractions carried by partons interacting, x_1 and x_2, as

$$\hat{s} = (x_1 p_1 + x_2 p_2)^2 \simeq x_1 x_2 s$$

Where the x_i are provided by the Parton Distribution Functions (PDF) $f(x)$ (see e.g. [CTEQ]). The probability to find a certain parton with a momentum fraction between x and $x + dx$ is given by the PDFs via $f(x)dx$.

3.1 W Boson Production

As mentioned above, the main process for W production is the Drell-Yan process. In proton-proton collisions, like at the LHC (see Section 4), the anti-quarks taking part in the interaction have to be sea-quarks, whereas the quarks may be either sea-quarks or valence-quarks. This is due to the internal structure of the proton (uud), which also gives rise to the larger cross-section for $u\bar{d}$ annihilation (W^+), relative to $d\bar{u}$ annihilation (W^-). In addition to the quarks

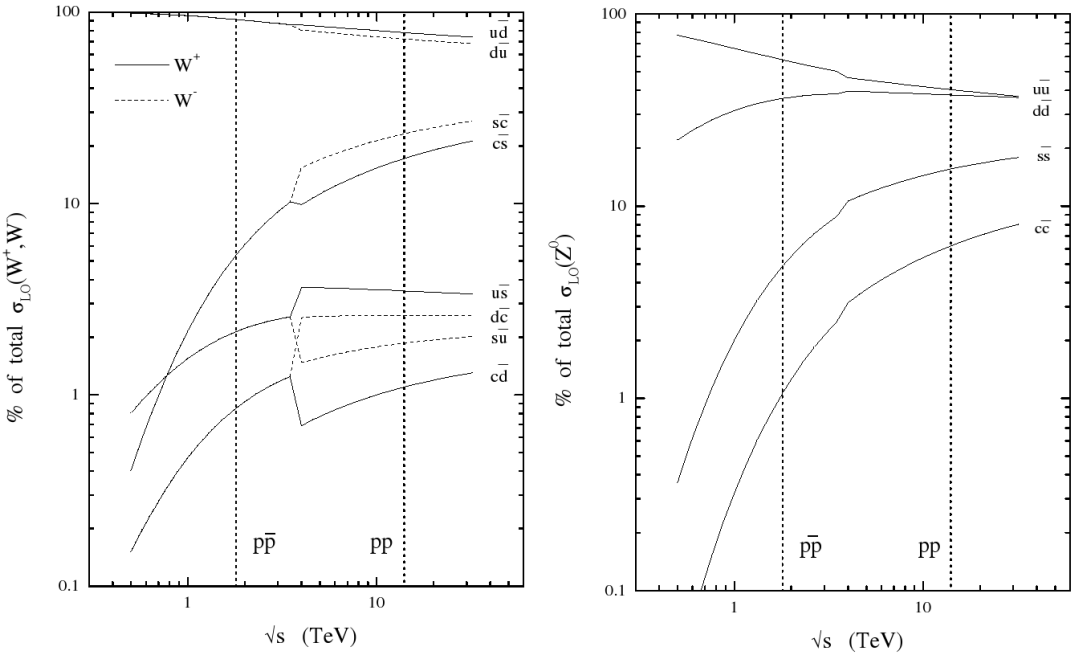

Figure 3.2: Flavour decompositions of $W^{\pm}$ (left) and Z^0 (right) cross-sections. In case of the W boson the solid lines represent the W^+ case, while the dashed refer to the W^- case. The dashed lines marked with $p\bar{p}$ and pp represent the cases for the Tevatron and the LHC, respectively. [MRST00]

of the first generation, there is also a contribution of about 10% from quarks of the second generation ($s\bar{c}$ and $c\bar{s}$). The complete flavour decomposition of the total cross-section for W production is given in Figure 3.2 (left).
In a leading-order approximation the W boson itself would not carry any transverse momentum p_T^W, but due to higher order corrections and the relative movement of the quarks, the W boson can reach transverse momenta up to about 100 GeV. Examples of higher-order Feynman diagrams, representing gluon or quark radiation in the initial state, are given in Figure 3.3. In the case of a W boson carrying a transverse momentum, the additional QCD contribution will cause a recoil $\vec{u}$ against the boson, observed as a jet in the detector.
From all possible decays, whose probabilities are given by the according branching ratios (see e.g. [PDG06] p. 362ff), the leptonic decays are of special interest:

$$u\bar{d} \to W^+ \to l^+\nu_l$$

Due to their clean signature, they are well suited for precision measurements of the properties of the W boson. An exemplary illustration of such a process, in terms of lowest-order Feynman diagrams, was already given in Figure 3.1 (left). The cross-section for $u\bar{d} \to l^+\nu_l$, in a leading-order approximation is given by

$$\left(\frac{d\sigma}{d\Omega}\right) = \frac{\alpha^2 |V_{ud}|^2}{192 \sin^4\theta_w \hat{s}} \frac{\hat{u}^2}{\left|\hat{s} - m_W^2 + i m_W \Gamma_W(\hat{s})\right|^2}$$

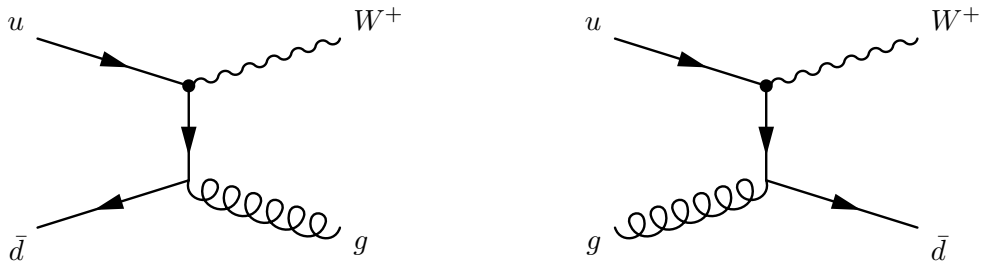

Figure 3.3: Higher-order Feynman diagrams for the W production, giving rise to gluon (left) or quark (right) in the final state. These will later on form the recoil against the W boson.

with the coupling *constant* $\alpha = \alpha(Q^2)$, the centre-of-mass energy $\hat{s}$, $\hat{u} = (p_u - p_l)^2 \sim (1+\cos\theta)$, the CKM matrix element V_{ud} and θ, the angle between the outgoing lepton and z axis in the Collins-Soper rest-frame [CS77]. The shape of this distribution is mainly given by the included Breit-Wigner distribution [BW36]. Using $d\Omega = |\sin\theta d\theta d\phi| = |d(\cos\theta)d\phi|$ this can be rewritten as

$$\frac{d\sigma}{d(\cos\theta)} = \underbrace{\frac{\pi\alpha^2|V_{ud}|^2}{24\sin^4\theta_w}\underbrace{\frac{\hat{s}}{|\hat{s} - m_W^2 + im_W\Gamma_W(\hat{s})|^2}}_{BW(\hat{s})}}_{\sigma_0(\hat{s})}(1+\cos\theta)^2 \tag{3.1}$$

In contrast to proton-anti-proton colliders, like the Tevatron, there is no forward-backward asymmetry A_{FB} in the W production at the LHC[1]. Therefore an additional term has to be added:

$$\frac{d\sigma}{d(\cos\theta)} \propto (1+\cos\theta)^2 + (1-\cos\theta)^2 \tag{3.2}$$

While not having a forward-backward asymmetry, there will be a asymmetry in the production rates of W^+ and W^-, which is due to the internal structure of the colliding protons (the availability of the different quark flavours), as mentioned earlier. Including higher order corrections, like the quark/gluon radiation in the initial state mentioned above, introduces changes in the helicity of the W boson and its transverse momentum p_T^W and therefore a different angular distribution (see e.g. [Mir92] for next-to-leading order expression).

3.2 Measurement of the W Boson Mass

The facts, that in hadronic collisions the initial quark momenta are unknown and that the experiment has a limited acceptance region (see ATLAS detector description in Chapter 5) implicate that the longitudinal components of particles moving down or close to the beam line (e.g. proton remnants) cannot be detected. Therefore numerous physics measurements are restricted to the so-called transverse plane, yielding quantities like the transverse energy E_T or the transverse momentum p_T. In case of the leptonic decay of the W boson, the difficulty of not being able to measure the longitudinal component of some constituents of the initial interaction gets even enhanced, due to the fact that the neutrino is not being detected by the experiment at all. Its energy can only be estimated through energy and

[1] At least, this is true in this leading order approximation.

momentum conservation laws from the measurement of energy and direction of the hadronic recoil $\vec{u}$ against the W boson (see Figure 3.4). Contrary to this all jets, created in case of hadronic decay into two quarks, can be measured in the detector. Still, due to the large QCD background, the hadronic decay channels are not used for precise W boson mass measurements. One quantity that is used to obtain the mass of the W boson, based on this somewhat error-prone measurement, is the transverse mass of the W boson m_T^W. It is derived following the calculation of the invariant mass, but using the two-momentum in the transverse plane instead of the three-momentum, i.e. treating all longitudinal components as zero.

$$\begin{aligned} m_{inv}^W &= \sqrt{(E^l + E^\nu)^2 - (\vec{p}^l + \vec{p}^\nu)^2} \\ m_T^W &= \sqrt{(E_T^l + E_T^\nu)^2 - (\vec{p}_T^l + \vec{p}_T^\nu)^2} \\ &\approx \sqrt{(p_T^l + p_T^\nu)^2 - (\vec{p}_T^l + \vec{p}_T^\nu)^2} \\ m_T^W &= \sqrt{2p_T^l p_T^\nu - 2\vec{p}_T^l \cdot \vec{p}_T^\nu} = \sqrt{2p_T^l p_T^\nu (1 - \cos\Delta\phi)} \end{aligned} \tag{3.3}$$

Where $\Delta\phi$ denotes the angle between the charged lepton and the neutrino, as illustrated in Figure 3.4. In the ideal case m_T^W always lies in the range $0 \leq m_T^W \leq m^W$, yielding a so-called Jacobian edge at $m_T^W = m^W$ [BMP83]. In reality this turns out to be a finite edge, due to a smeared $\hat{s}$-distribution, according to the PDFs, and a finite detector efficiency. The smearing is given by the W width Γ_W. Allowing a transverse momentum of the W boson ($p_T^W > 0$), by including higher order diagrams, results in further reduction of the sharpness of this edge. On the other hand, this implies that to first order, the transverse mass is independent of the W boson transverse momentum. The transverse momentum of the neutrino p_T^ν is estimated from p_T^l and the recoil against the boson $\vec{u}$ through

$$\vec{p}_T^\nu = -\vec{p}_T^l - \vec{u} \quad \text{with} \quad \vec{u} = -\vec{p}_T^W \tag{3.4}$$

Using (3.4) Equation 3.3 can be written, in terms of the lepton transverse momentum $\vec{p}_T^l$ and the recoil $\vec{u}$, as

$$m_T^W = \sqrt{2|\vec{p}_T^l||\vec{p}_T^l + \vec{u}| + 2\vec{p}_T^l \cdot (\vec{p}_T^l + \vec{u})} \tag{3.5}$$

In leading-order, the expansion of this expression as a Taylor series in u/p_T^l, yields

$$m_T^{W,LO} = 2p_T^l \tag{3.6}$$

The mass of the W boson is finally obtained by fitting multiple theoretical models (templates), assuming different W boson masses, to the transverse mass distribution. This method is therefore referred to as the template method. Thereby its necessary that the theoretical model is as complete and precise as possible. This includes the correct modelling of e.g. the cross-section, angular distributions, the recoil and the detector resolution. The obvious, main uncertainties in this measurement are introduced by the MC modelling of the data. Due to an additional smearing of the transverse neutrino momentum by the pile-up at high-luminosity, this method will most likely be limited to the low-luminosity phase.
Another possibility of measuring the W boson mass is over the lepton transverse momentum spectrum p_T^l. As indicated above (see Equation 3.6), the W boson mass can be extracted using the peak value of the p_T^l distribution. Similar to the transverse mass Jacobian peak at

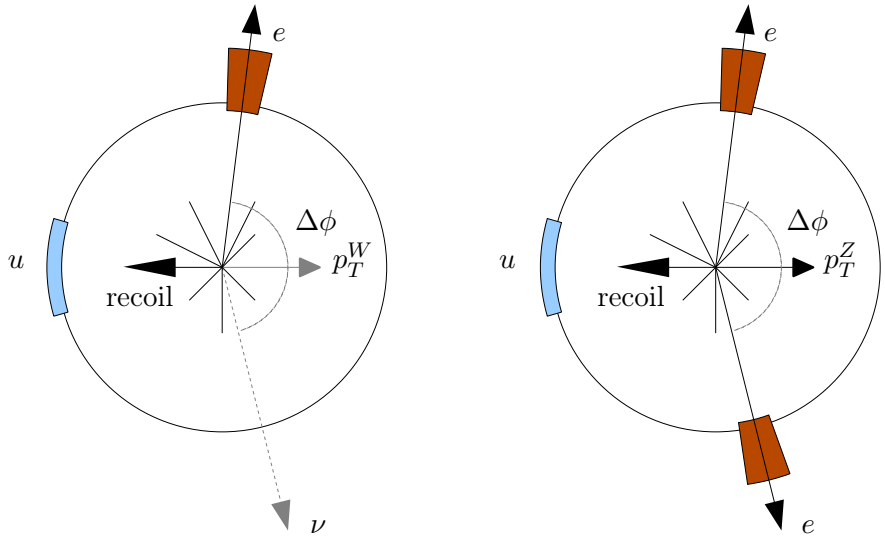

Figure 3.4: Illustration of a $W \to e\nu$ and a $Z \to ee$ event in the transverse plane. In both events the bosons carry a transverse momentum p_T, resulting in a recoil u against the boson. While the electrons and the recoil can be measured in the calorimeters (red and blue boxes) the neutrino stays undetected, yielding some missing transverse energy $\not{E}_T$. The angle between the electron and the neutrino/electron is given by $\Delta\phi$.

$m_T^W = m^W$, the transverse momentum distribution has a Jacobian peak at $p_T^l = m^W/2$, that is smeared due to e.g. higher-order QCD corrections [SvNV83]. Giving better resolution than the transverse mass method in case $p_T^W = 0$, due to less sensitivity to detector response to the recoil, it suffers more in cases where the W boson carries a transverse momentum. While the correction due to p_T^W is only quadratic $(p_T^W/m_W)^2$ for m_T^W, there is a linear correlation (p_T^W/m_W) between p_T^W and p_T^l [A+98].
Figure 3.5 illustrates the fact, that the transverse mass is mainly smeared by the missing energy resolution, while for the lepton transverse momentum distribution its the transverse momentum of the boson.
Regardless of the method used, the precise measurement of the lepton transverse momentum p_T^l is essential. In the latter case, the distribution of p_T^l is used directly, while in the former method, p_T^l appears in the transverse mass formula (3.3) both directly and indirectly over the estimation of the neutrino momentum (3.4). The recoil scale itself can be calibrated by using e.g. the Z boson as a reference (see Figure 3.4). Since both leptons are detectable in this case, the recoil can be calculated and the corresponding response of the calorimeters can be used as an input[2] for the W boson.
Another measurement strategy used to calculate the mass of the W boson, also utilising the Z boson as a reference and used for the purpose of this thesis, will be presented in Section 7.1.
The major backgrounds for the interesting leptonic decays ($W \to l\mu$, $l = e, \mu$) of the W boson are the step-wise decay $W \to \tau\mu$ and $\tau \to l\nu$, $l = e, \mu$, introducing a second undetected neutrino and the so-called *mimic* decays of Z bosons ($Z \to ll$, $l = e, \mu$), where one of the leptons is out of the detector acceptance. A less significant background is coming from di-jet

[2]Using the Z as a reference for the W requires an additional weighting factor.

$(q\bar{q})$ events, with mismeasured jets. The small influence of the latter ones is due to an expected jet rejection in the electron sample of about 10^4-10^5, closer to the latter [TDR99a].
The total cross-section for $pp \to W + X$ with $W \to e\nu/\mu\nu$ channels, at the LHC, is expected to be about 30 nb. This corresponds to about 300 million produced events in one year of low-luminosity data taking. At ATLAS the selection criteria for a clean W signature include: a) an isolated charged lepton with $p_T^l > 25$ GeV and with $\eta < 2.4$, b) a missing energy $\not{E}_T > 25$ GeV, c) no jets with $p_T^{jet} > 25$ GeV and d) a recoil satisfying $|\vec{u}| < 20GeV$ [TDR99b]. The latter two cuts are due to reject events with W bosons carrying too large transverse momentum p_T^W. The p_T^l-cut is due to the missing transverse energy resolution, not allowing for a precise estimate at lower energies. With the overall acceptance of the above cuts being about 25% and assumed reconstruction and identification efficiencies of about 90% and 80%, respectively, the total selection efficiency is expected to be about 20%. Still this results in approximately 60 million W bosons within the first year of data-taking at low luminosity (10 fb^{-1}), being 50 times higher than expected from the Tevatron Run 2.

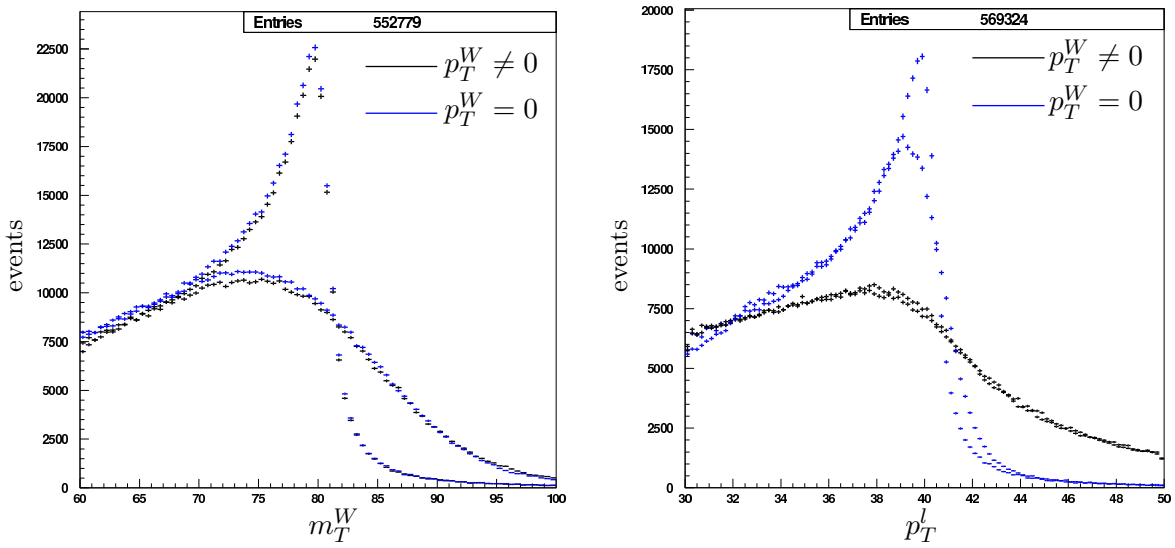

Figure 3.5: Figure showing the truth and the reconstructed distributions of m_T^W (left) and p_T^l (right). m_T^W is mainly smeared by the missing energy resolution, whereas p_T^l is mainly smeared by the transverse momentum of the W boson p_T^W. The missing energy is due to unmeasured, *roughly* estimated momentum of the neutrino.

3.3 Z Boson Production and Mass Measurement

The main production process for the Z boson is, like the W boson case, the Drell-Yan process. The lowest-order Feyman diagram for the exemplary process $u\bar{u} \to Z \to e^+e^-$ is shown in Figure 3.1 (right). The Z boson is produced by the annihilation of a quark and the according anti-quark. At the LHC, the anti-quark has to be a sea quark, while the quark can be both sea or valence quark. Due to the internal structure of the proton, the main contribution comes from $u\bar{u}$-annihilation. A detailed illustration of the flavour decomposition is shown in Figure 3.2 (right). In a similar manner as for the W boson, there are higher order contributions

representing gluon or quark radiation in the initial state (see Figure 3.3).
In contrast to the W boson, the Z boson has no clean V-A interaction and therefore also couples to the right-handed components of the leptons. In addition the Z boson can interfere with the photon.
The kinematics and properties (e.g. mass) of the Z boson are well known nowadays, mainly caused by the fact that it could be produced directly in the e^+e^--collisions at the LEP, the predecessor of the LHC (see Chapter 4), while the W boson could only be produced in W^+W^--pairs with low statistics, due to its electrical charge and the cross-section being proportional to $1/\hat{s}$, respectively.
The fact that both leptons, created in the decay of the Z boson, can be measured by the experiment (if within the detector acceptance) allows for the direct calculation of the Z boson mass, using the invariant mass formula:

$$m_Z = \sqrt{2\left(p_{l_1}p_{l_2} - p_{T,l_1}p_{T,l_2}\cos\Delta\phi - p_{z,l_1}p_{z,l_2}\right)} \tag{3.7}$$

In the same manner as for the W boson, the lepton transverse momentum spectrum and the transverse mass spectrum can be used as complemental measurements.
The total number of Z bosons produced at ATLAS in one year of data taking at low luminosity is expected to be about 33 million. The selection criteria for Z bosons are: a) an isolated electron with $p_T^l > 25$ GeV and with $\eta < 2.4$, b) two isolated electrons with $p_T^l > 25$ GeV and with $\eta < 2.4$ each, c) an isolated muon with $p_T^l > 20$ GeV and with $\eta < 2.4$, b) two isolated electrons with $p_T^l > 10$ GeV and with $\eta < 2.4$ each. With the overall acceptance of the above cuts, the reconstruction and identification efficiencies being similar to the W case in the previous section, the total selection efficiency is expected to be about 20%. This results in approximately 6.6 million Z bosons within the first year of the low-luminosity (10 fb^{-1}) phase. The ratio between Z and W events of about $N_Z/N_W = 1/10$ explains, that when using the Z boson as a reference in the W boson mass measurement, in fact the Z boson statistic is the *limiting* factor, even though the number of produced Z bosons is many times over the number ever produced before.

Part II

Accelerator and Detector

Chapter 4

The Large Hadron Collider

The European Laboratory for Particle Physics (CERN), situated at the French-Swiss border near Geneva, is the world's larges particle physics lab. Over 11 years, ending in 2000, CERN was running the Large Electron Positron (LEP), an electron-positron collider. Placed in a 27 km long circular tunnel, about 100 m under ground, the LEP produced collisions up to energies of 208 GeV, in centre of mass (CM).
Even though the LEP has been a large success, still many questions, about the Standard Model and possible new physics beyond, remained unanswered. Therefore it was decided, even before LEP stopped running, to build a new research facility at CERN, allowing to explore energy regimes far beyond LEP's capabilities.
Consisting of a new accelerator, the Large Hadron Collider (LHC), and four experiments to study the physics of the collisions, it is currently being build and scheduled for first physics results in 2008. The LHC as well as the ATLAS experiment will be described in the following sections, putting special emphasis on the subsystem used in the analyses presented in this thesis.

4.1 The Accelerator

The Large Hadron Collider (LHC) is a proton-proton collider, situated in the former LEP tunnel. A hadron collider was chosen to overcome the limiting factor of the LEP, the energy loss due to synchrotron radiation. Since this loss is in inverse proportion to the particle mass cubed, protons, compared to electrons and positrons, can be accelerated to higher energies, using the given physical dimensions of the LEP tunnel. Due to the requirement on very high luminosity a proton-proton collider was chosen. Whilst a proton-antiproton collider has the advantage of being able to keep both counter-rotating beams in the same beam pipe, the production of the enormous amounts of antiprotons, required for the high luminosity, is not realistic and would be more expensive than the proton-proton solution with separate beam pipes. Since at the energies of the LHC it is mainly sea quarks and gluons colliding, there is no real difference in the physics between both types of colliders.
The protons will be preaccelerated to an energy of 450 GeV, by the existing accelarator facilities at CERN. After the injection into the LHC ring they will be further accelerated to 7 TeV, allowing for a CM energy of 14 TeV. The energy of the protons and thereby the CM energy is limited by the strength of the magnetic field holding the beam inside the ring. This magnetic field, of about 8 T, will be produced by about 5000 superconducting niobium-

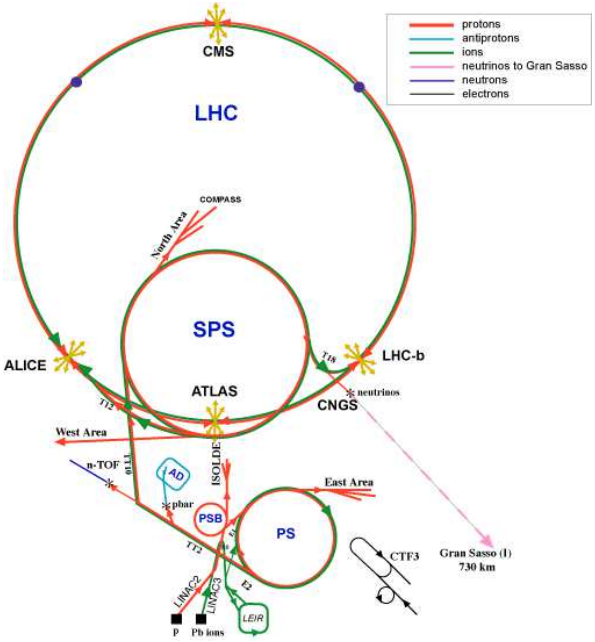

Figure 4.1: The CERN accelerator complex. Showing the Large Hadron Collider (LHC), the four detectors (ALICE, ATLAS, CMS, LHCb) and the existing accelarator facilities [ATLa].

titanium magnets, cooled by super-fluid Helium [TDR99b]. To collide two equally charged proton beams, circulating in opposite directions, the magnet system is designed to have two separate beamlines, filled with a maximum number of 2835 bunches[1], containing about 10^{11} particles each. The two proton beams will be brought to cross at four interaction points, determining the position of the four experiments planed for LHC.
In addition to proton-proton collisions, the LHC is also capable of accelerating and colliding heavy nuclei. Figure 4.1 shows a schematic drawing of the CERN accelerator complex as well as the position of the four detectors along the LHC.

4.2 Experiments at the Large Hadron Collider

The four experiments, currently being build at the LHC, can be devided into two categories: general and special purpose detectors. ALICE (A Large Ion Collider Experiment), designed for the study of quark-gluon plasma created in heavy nuclei collisions, and LHCb (Large Hadron Collider beauty experiment), build for the study of CP-violation in the b-quark system, belong to the latter group. ATLAS (A Toroidal LHC ApparatuS) and CMS (Compact Muon Solenoid), both being designed for a broad study of SM physics and possible new physics beyond, are therefore general purpose detectors.
The beams of protons will be collided at the experiments with a design luminosity of $L_{low} = 10^{33} cm^{-2} s^{-1}$ in the initial phase and $L_{high} = 10^{34} cm^{-2} s^{-1}$ during the later high luminosity phase. After the initial phase, which is planed to take three years, the integrated luminosity is expected to be about 30 fb^{-}1 [TDR99b]. Since the LHC beam comissioning at the energy

[1]This number of bunches will not be used from the very beginning.

of the injector ring (450 GeV) is scheduled for the end of 2007, the first physics measurements in the experiments cannot be expected before summer 2008. During the first phase of low luminosity, interactions are expected to happen with a rate of up to 40 MHz. The number of observed events n_{obs} for a specific channel in one of the experiments can be derived from the process' cross section σ, the branching ratio BR for the specific decay, the overall running time of the experiment t and the efficiency of that experiment to detect this particular process ε, using the formula:

$$n_{obs} = L \cdot \sigma \cdot BR \cdot t \cdot \varepsilon. \tag{4.1}$$

Chapter 5

The ATLAS Detector

The two studies presented in this thesis are both related to the ATLAS experiment and therefore the ATLAS detector will be described in this chapter. After an introduction to the general layout of detectors in particle physics, the ATLAS design concept as well as all subsystems will be presented. Special emphasis will be put on the Transition Radiation Tracker (TRT), due to the fact that one of the studies presented in this thesis requires more detailed knowledge of this subdetector of ATLAS. Still this chapter will not impart full knowledge on all the subsystems of ATLAS, therefore the reader is referred to [TDR99b] and [TDR97] (also being the basis for this chapter, if not stated differently) for a more complete description. In the end some remarks on the simulation of the ATLAS detector will be given.

5.1 General Detector Layout

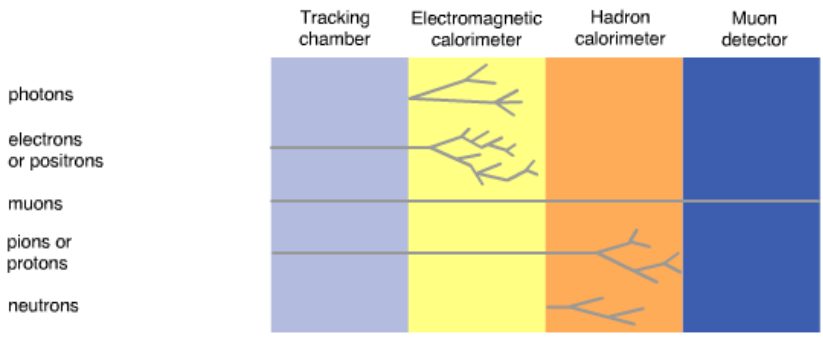

Figure 5.1: Schematic drawing of a general purpose detector with its layers of subdetectors. The response to different particle types is illustrated for all subdetectors.

The overall task of a general purpose particle detector, like ATLAS or CMS, is to reconstruct the primary interaction. This includes knowledge about the position of the primary vertex as well as the participating particles and their properties, like mass and momentum. To be able to access this information it is necessary to collect all possible information on the final outcomes. These final states can be of all kind, but mainly due to their lifetime boil down to photons, electrons, muons, neutrinos, hadrons (e.g. pions or neutrons) and jets. Where jets are narrow cones of mainly hadrons, created by the hadronisation of a quark or gluon, due to

QCD confinement. Therefore a mixture of different types of subdetectors is needed to identify these particles and reconstruct their properties. Not to loose any information, general purpose particle detectors are often designed in a 4π symmetry, consisting of a barrel and two end-cap parts[1]. This division is usually passed on to all subdetectors.
In general, particle detectors can be categorised in two groups: either they may measure the position of a passing particle, allowing to reconstruct the path the particle took and, by the help of a magnetic field, calculate the momentum of the particle, or they may measure the energy of the particle. In modern particle physics, general purpose particle detectors are build in layers following the scheme illustrated in Figure 5.1.
The innermost subdetector is a tracking detector, belonging to the first group mentioned above. By detecting the ionisation particles produced by a charged particle along its path through the detector, the track and therefore the origin of these particles can be obtained. In the presence of a magnetic field, the tracking detector allows for the measurement of the momentum carried by a particle, due to its deflection by the magnetic field. To optimise the tracking and the determination of the initial vertex, the tracking detector contains as little as possible material to disturb the particles and is build as close as possible to the interaction point, respectively. The tracking detector can again be composed out of different subdetectors, using slightly different detection techniques, or taking advantage of other physics effects, like transition radiation, to add particle identification abilities.
The next layer of a general purpose particle detector is the calorimeter system (see Figure 5.1), belonging to the second group of detectors. It allows for the energy measurement as well as the identification of, both charged and neutral, particles. Through interaction with the material most particles will be fully absorbed, allowing for an estimate of the particle's energy. In addition, secondary particles will be created, forming a shower following the direction of the initial particle. Since the shape is different for showers produced by electrons/photons and hadrons, it is possible to distinguish different particle types. Usually electromagnetic showers ($e^{\pm}, \gamma$) are narrow and self-contained and due to the fact that QED processes are relatively well understood, the energy of the initial particle can be reconstructed to a high precision. In contrast to this, hadronic showers are formed by nuclear interactions (creating e.g. $K^{\pm}, \pi^{\pm}, \gamma$), resulting in a deeper penetrating, broader and more complex shower shape. Due to these differences the calorimeter system is typically build of a thinner high resolution electromagnetic calorimeter in front of a hadronic calorimeter (see Figure 5.1).
The outermost layer is an additional tracking detector specially designed to identify and measure the momentum of muons. Since muons are very weakly interacting particles, they will not be absorbed by the calorimeters (in case p_T^{μ} >5 GeV).

5.2 ATLAS Design Concept

Following the scheme, given in the previous section, the ATLAS experiment consists of several subdetectors placed as cylindrical layers, centred around the interaction point. The innermost part is the Inner Detector (ID) with a length of 7 m and a radius of 1.5 m. It is contained in a solenoidal magnetic field of 2 T, which allows for momentum measurements in the ID. The intermediate layer is given by an electromagnetic and a hadronic calorimeter, including the solenoid flux-return iron yoke. The outermost layer is represented by the Muon Spectrometer, also defining the overall dimensions of ATLAS to be about 42 m in length and 22 m in

[1] For fixed-target experiments this is not the case.

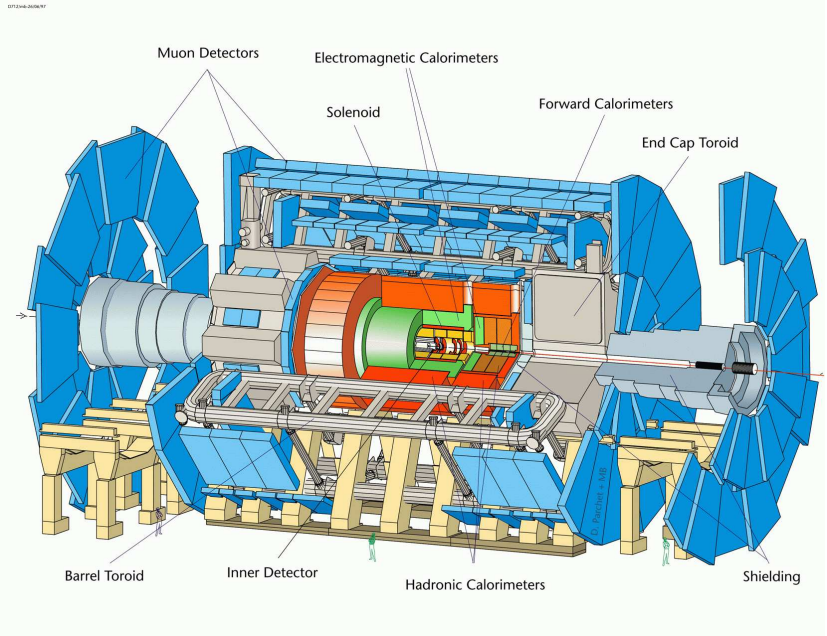

Figure 5.2: Schematic drawing of the ATLAS detector [TDR99b].

diameter. Figure 5.2 shows a schematic drawing of the ATLAS Design Concept, with all mentioned subsystems, being adumbrated in the following sections. This chapter will only cover general features and capabilities to such an extend that the reader is more than capable of following the discussion, while central but technical information will not be included.
To parametrise a point in space, a special ATLAS Coordinate System, shown in Figure 5.3, has been introduced. The z-axis is defined by the beam direction and the x-y-plane is the one transverse to that. Whereas the positive x-axis is pointing towards the centre of the LHC and the positive y-axis is pointing upwards. Alternatively, space points can be described by a radial distance r to the interaction point, an azimuthal angle ϕ, measured around the beam axis (in the x-y-plane) and a polar angle θ, being the angle to the beam axis.
Due to some simplifications under Lorentz boosts, the pseudorapidity η, defined as

$$\eta = -\ln\left[\tan\left(\theta/2\right)\right], \tag{5.1}$$

was introduced in exchange for the polar angle θ. This gives a measure having a small absolute value $|\eta|$ for particle being almost perpendicular to the beam axis and large $|\eta|$ for those close to the beam axis. This variable will, in the following sections, also be used to characterise the coverage of each of the subsystems.

5.3 Magnet System

The ATLAS Magnet System consists of two major components, a Central Solenoid (CS) and a toroidal part, generating the magnetic field for the muon spectrometer. The CS, having a peak field of 2.6 T, provides the magnetic field for the ID, allowing for momentum measurements. It is positioned just in front of the Electromagnetic Calorimeter, sharing the same vacuum vessel

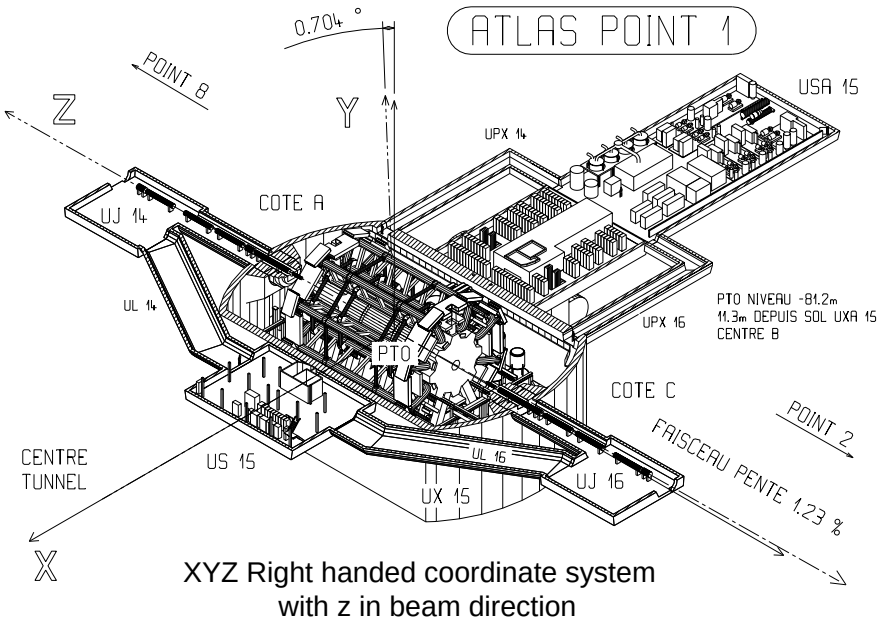

Figure 5.3: The ATLAS Coordinate System [ATLa].

to reduce the amount of material. The toroidal part, being the first of its kind and certainly not conventional, is build out of three segments, a Barrel Toroid (BT), having a peak field of 3.9 T and two EndCap Toroids (ECT), with a peak field of 4.1 T. Each of the three is build out of eight coils located radially and symmetrically around the beam axis. Thereby the ECT is rotated, relative to the BT, by 22.5°, to gain an overlap and with this a better performance in that region. Due to economical reasons such a low number of coils was chosen, with the drawback of having large variations in the magnetic field and a slight breaking in the phi symmetry. But still, thanks to the toroidal design, particles will traverse the field almost perpendicular at all η values and thereby allow for the best momentum resolution.

5.4 Inner Detector

The ATLAS Inner Detector (ID), shown in Figure 5.4, is build out of three parts in cylindrical layers: a central barrel part and one of two identical endcaps on each side. The inner part of the ID consists of high-resolution semi-conducting detectors, whereas the outer part, a straw tube tracker (TRT), delivers continuous tracking. The combination of both techniques provides high precision measurements in ϕ and z, without having too much material in front of the calorimeters and within economical feasibility. In addition this design, by the use of the large number of hits in the outer part of the ID, allows for a precise momentum measurement and, by detection of transition radiation in the TRT, for electron identification (see Section 5.4.3 and Chapter 6).

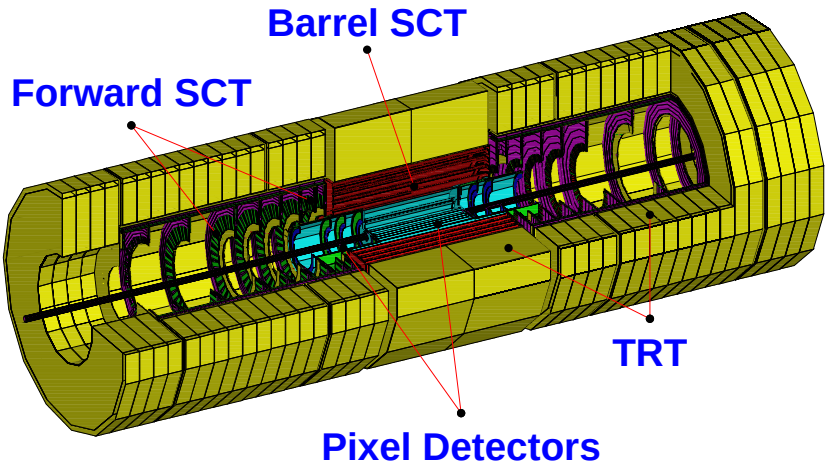

Figure 5.4: A schematic 3D drawing of the ATLAS Inner Detector [TDR97].

5.4.1 Pixel Detector

The Pixel Detector, being the innermost part of ATLAS, is build with a high granularity to allow for high-precision measurements, as close as possible to the interaction point, even at large track densities. It consists of three overlapping barrel layers (at radii of ∼4, 11 and 14 cm) and four discs at each side (with radii of 11 and 20 cm). Designed with a two-dimensional segmentation, with pixels of a size of $50 \times 400 \mu$m, it is expected to give three precise tracking points for each track. Even at high luminosity the Pixel Detector will provide good vertexing for the expected 25 initial interactions per bunch crossing and secondary vertexes (b, c , τ, etc.).

5.4.2 Semiconductor Tracker

The Semiconductor Tracker (SCT), positioned in the intermediate radial range in the ID, is build out of eight layers of silicon microstrip detectors. Each of these 6.36×6.40 cm^2 p-on-n detectors, is designed to provide a precise measurement of the $R\phi$ coordinates. Modules of four detectors, with two forming a strip and being rotated by a 40 mrad angle with respect to the other two, allow for the additional measurement of the z coordinate. With an overall area of 63 m^2 of silicon detectors, the SCT is expected to provide eight precise measurements per track, with a coverage of $|\eta| \leq 2.5$, including the forward modules. These forward modules are arranged in 9 disks in each end-cap and are constructed in a similar manner, while having a different geometrical layout.

5.4.3 Transition Radiation Tracker

The outermost part of the ID is the Transition Radiation Tracker (TRT). The TRT is build after the concept of a straw detector combined with transition-radiation detection. Due to its position further away from the interaction region, the loss in resolution compared to semiconductor trackers was favoured because of economical reasons. In addition the detection of transition-radiation (TR) photons, produced in a radiator between and measured by the

use of Xe gas in the straws, allows for electron identification capabilities, not available in semiconductor trackers.

Detector Layout

The TRT consists of a barrel and an end-cap part, covering the ranges $|\eta| < 0.8$ and $0.8 < |\eta| < 2.5$, respectively. The about 50000 straws in the barrel part are divided in two at the centre, creating effectively twice the number, in order to reduce the occupancy and read out at each end. For the same reason the first six radial layers of straws are inactive over the central 80 cm. The barrel covers $\pm$ 75 cm in z and consists of three radial sections, each with 32 modules. The end-cap part, in the original design consisting of 18 wheels (6 Type A, 8 Type B, 4 Type C), contains about 320000 radial straws. Due to economical reasons the C wheels will miss their electronics in the initial layout. The difference in the layout between the barrel (straws parallel to the beam axis) and the end-caps (straws perpendicular to the beam axis) ensures that particles will hit as many straws as possible and as perpendicular as possible.

Basic Detector Properties

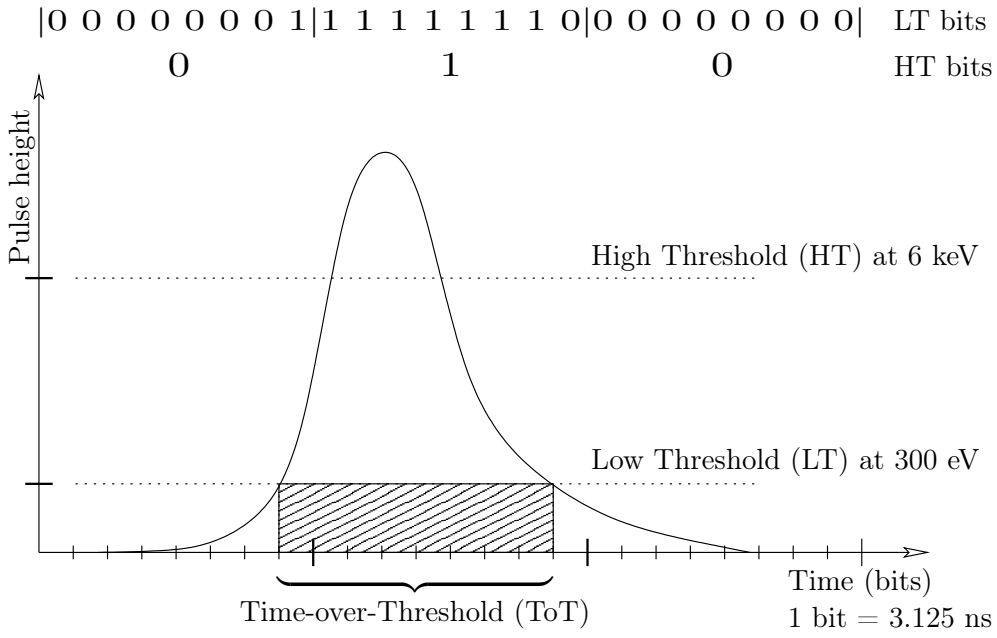

Figure 5.5: Example of a TRT pulse including its LT and HT bit response.

Each of the in total 420000 channels provides a drift-time measurement, with a spatial resolution of 170μm per straw, and two independent thresholds, illustrated in Figure 5.5. These thresholds allow the detector to discriminate between tracking hits, which pass the lower threshold (LT), and transition-radiation hits, which pass the higher threshold (HT). The information about these thresholds over a 75 ns window is encoded in a 27 bit pattern, yielding a simple boolean information for the HT, in three regions of 25 ns each, and a discrete time-over-threshold (ToT) information for the LT. An exemplary TRT pulse and the according LT and HT bit response is shown in Figure 5.5.

Tracking in the TRT

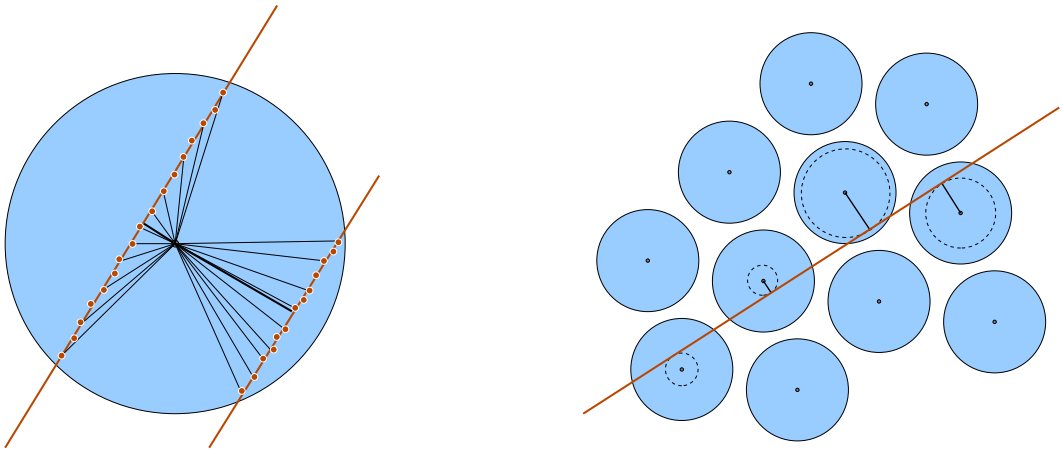

Figure 5.6: Left: Schematic drawing of the ionisation electrons (red dots) created by charged particles traversing a TRT straw (red lines). The shortest distance between the anode wire and the particle track is indicated by thick black lines and is directly proportional to the measured drift-time. Right: Schematic drawing of the tracking principle in the TRT. A 2-dimensional track (red line) can be reconstructed from the radii (dotted circles) obtained from the drift-times of the various straws (circles).

The TRT is designed to measure on average 36 LT hits per track, in the range $|\eta| < 2.5$ (see Figure 6.7a). Each of the drift tubes is constructed as a straw of 4 mm in diameter with a 30 μm tungsten wire in the centre. The tubes are filled with gas mixture of about 70% Xe, 30% CO_2 and very little O_2. Charged particles traversing through the straws will ionise the gas along their track. The ionisation electrons will drift towards the anode wire in the centre of the straws, yielding a signal proportional to the amount of ionisation and the length the particle traversed through the straw (L). The leading edge of this signal, representing the arrival time of the ionisation electrons, allows the measurement of the radial distance of the track at its closest approach to the wire (R), as shown in Figure 5.6 (left). Having this information from various straws along the particle's trajectory, it is possible to reconstruct the track as illustrated in Figure 5.6 (right). Figure 5.7 shows the relation between the distance of the closest approach (R and the total distance in a straw (L), which will be used later on.

Particle Identification in the TRT

Even though the straw spacing has been optimised for tracking instead of the identification of electrons, the TRT still offers this feature, mainly via the detection of transition radiation (TR). TR, basically photons in the X-ray region, is produced when a relativistic particle traverses a boundary between materials of different dielectric constants. The total energy loss of a charged particle on the transition depends on its Lorentz factor $\gamma = E/mc^2$, while the angular distribution is peaked forward with a sharp maximum at $\theta = 1/\gamma$. Since a Lorentz factor above 1000 is needed and thus essentially only electrons produce TR, this allows for the separation of electrons and hadrons (mainly pions), at highly relativistic energies. The large fraction of Xe in the gas mixture has been chosen to intensify this effect, since Xe is a

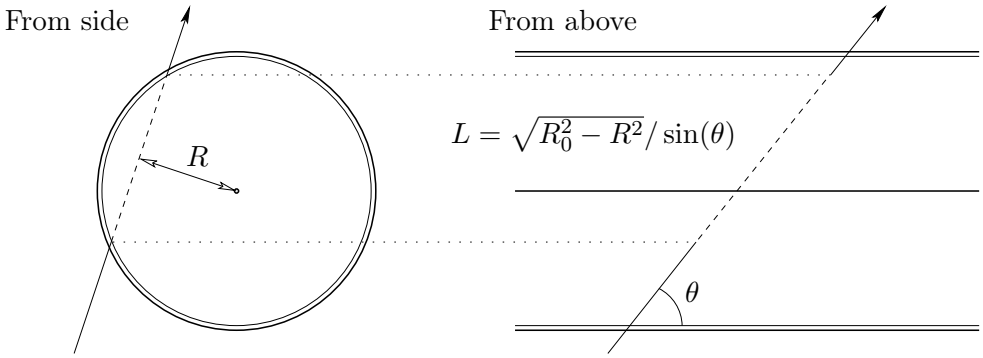

Figure 5.7: Illustration of the path length of a track L in a straw (R_0 being the straw radius).

good X-ray absorber. To increase the amount of TR, produced by the charged particle, the straws are interleaved with a material containing a lot of boundaries. This so called radiator, being polyethylene/polypropylene, is implemented as a regular foil between the straws in the end-cap parts and fibres squeezed between the straws in the barrel region.
In a very basic approach, the two discriminator levels, LT for tracking hits and HT for a TR induced hits, can be used to identify electrons by requirering a certain number of HT hits on a track. This and more advanced methods will be discussed in Chapter 6.

5.5 Calorimeters

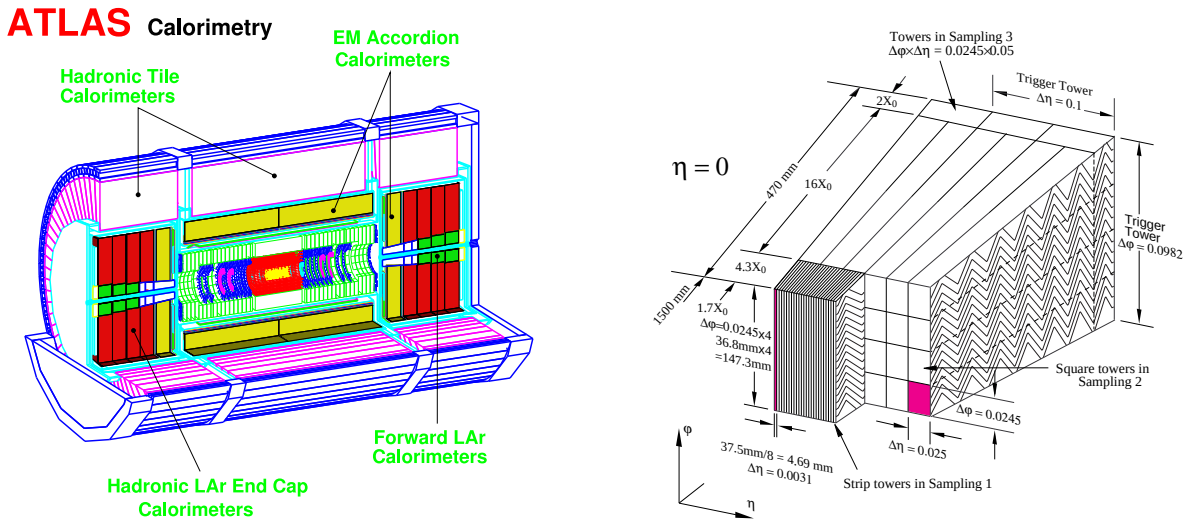

Figure 5.8: A schematic 3D drawing of the ATLAS Calorimeters (left) and the barrel electromagnetic calorimeter (right). [TDR99b].

A schematic 3D drawing of the ATLAS Calorimeters is shown in Figure 5.8 (left). Located in a region of low magnetic field, due to the design of the Magnet System (see Section 5.3), the

ATLAS calorimetry allows for the detection of particle showers without further broadening. The Electromagnetic (EM) Calorimeter as well as the three components of the Hadronic Calorimeter will be described in the following sections.

5.5.1 Electromagnetic Calorimeter

The EM calorimeter is a lead liquid argon (LAr) detector build in an accordion like geometry to provide full ϕ symmetry. It is a sampling calorimeter made of alternating layers of lead (absorber) and LAr (active material) and consist of a barrel part ($|\eta| < 1.5$) and two end-cap wheels on each side (outer wheel: $1.375 < |\eta| < 2.5$, inner wheel: $2.5 < |\eta| < 3.2$). Up to the outer wheel the EM calorimeter is segmented into three longitudinal sections (samplings), shown in Figure 5.8 (right).
The first sampling is a preshower detector designed to separate π^0s and photons. It has the highest granularity in η (see Figure 5.8, right) and a depth of about 4.3 radiation lengths [2](X_0).
The second sampling, with a depth of about 16 X_0s, is the largest section of the EM calorimeter and therefore most of the energy will be deposited in there. Compared to the first sampling the granularity in η is reduced by factor of about eight, whereas in ϕ it is increased by a factor of four, allowing for precise position measurement in both coordinates.
The third sampling, with a depth of about 2 X_0s, was designed to have half the resolution in η, due to the anyway wide spread of EM showers at this depth.
Due to the larger amount of material in front of the EM calorimeter in the barrel region ($|\eta| < 1.8$) the first sampling is preceded by an additional layer. This, so called presampler, is a single layer of LAr, added to correct for the energy loss in the ID and the cryostat.

5.5.2 Hadronic Calorimeters

The ATLAS Hadronic Calorimeter system (see Figure 5.8, left) is composed out of four subsystems, using two different calorimeter techniques. This is due to the high radiation level close to the beam pipe. The barrel and extended barrel calorimeters (Tile), covering the range $|\eta| < 1.7$, are made out of alternating plastic scintillator tiles, as active material, and iron tiles, as absorber material, whereas the hadronic end-cap calorimeter (HEC) and the forward calorimeter (FCAL) use the LAr technique. In difference to the EM calorimeter, copper is used as absorber material in the HEC ($\sim 1.5 < |\eta| < 3.2$) and a copper-tungsten combination in the FCAL ($3.1 < |\eta| < 4.9$).
With depths between about 9.5 interaction lengths [3] (λ) in the FCAL and about 11 λ at $\eta = 0$, the Hadronic Calorimeters provide measurements with large angular coverage and therefore allow for good E_T^{miss} measurements.

5.6 Muon Spectrometer

The ATLAS Muon Spectrometer, shown in Figure 5.9, is designed to measure muon tracks deflected by a magnetic field (see Section 5.3). With two interleaved detector designs it allows for

[2]The mean distance over which a high-energy electron loses all but 1/e of its energy or 7/9 of the mean free path for pair production by a high-energy photon.
[3]The mean free path of a particle before undergoing an interaction that is neither elastic nor quasi-elastic (diffractive), in a given medium.

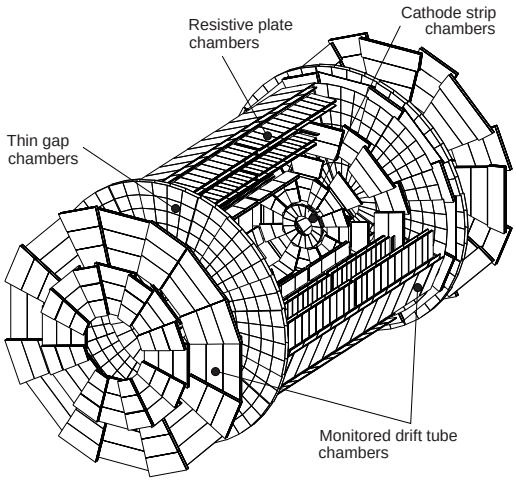

Figure 5.9: A schematic 3D drawing of the Muon Spectrometer [TDR99b].

fast responding trigger decisions as well as high-precision tracking. Both the barrel ($|\eta| < 1$) and the end-cap ($1 < |\eta| < 2.7$) region, consisting of three respectively four layers of detectors, allow for precise position and momentum measurements of the traversing muons. For these measurements a precise matching with the ID is important and an energy loss between one and three GeV, due to material in the calorimeters, has to be taken into account. The upstream material, especially in the hadronic calorimeter, is also what makes the muon system a PID system, since hadrons hardly make it through. The inner part of the muon system is made out of Monitored Drift Tubes (MDTs), while at higher η Cathode Strip Chambers (CSCs) are used, due to the higher radiation level. The MDTs are aluminium drifttubes with a central W-Re wire, 30 mm in diameter and filled with a 93% Ar and 7% CO_2 gas mixture. The CSCs are multiwire proportional chambers with cathode strip readout. Thereby the coordinates are obtained by measuring the induced charge on the segmented cathode formed by the avalanche, created close to the anode, and by the cathod's segmentation as well as charge interpolation between neighbouring strips. With average drifttimes, of 300 ns for the MDTs and 30 ns for the CSCs, being to long compared to the 25 ns between two bunch-crossings, these detector types can not be used as trigger input.
The trigger chambers, covering the range $|\eta| < 2.4$, therefore consist of Resistive Plate Chambers (RPCs) and Thin Gap Chambers (TGCs) at higher η, again due to the higher radiation level. The RPCs are gaseous detectors consisting of parallel resistive bakelite plates, alternating with narrow gas gaps. In which the signal, being read out via capacitive coupling, is obtained from ionisation electrons, multiplied into avalanches by a high electrical field. With drifttimes around 10 ns, both the RPCs and the TGCs, being slightly modified multi-wire proportional chambers, provide fast enough readout to be used for the trigger.

5.7 Trigger System

The ATLAS Trigger System consists of three levels of online event selection: the level-1 (LVL1) and level-2 (LVL2) triggers and Event Filter (EV). Each of the levels refines the decision made by the previous one and/or applies additional selections. This system of trigger level has to assure an excellent efficiency for rare new physics events and still reduce the event selection rate from an initial bunch-crossing rate of 40 MHz (at high luminosity) to about 100 Hz for long-term storage. This requires an overall rejection factor of 10^7 against 'minimum bias' events.
The LVL1, reducing the initial interaction rate to about 100 kHz, provides the initial selection based on information of a subset of detectors: the trigger chambers (RPCs, TGCs) of the muon spectrometer to select high p_T muon events and reduced-granularity information from all calorimeters to select high p_T electron, photon, jet, τ-lepton decaying into hadron and large E_T^{miss} and E_T events. To keep the latency (time to make the trigger decision) small the LVL1 trigger is hardware based and located at the front-end electronics. Events accepted by the LVL1 trigger are, together with a region-of-interest (RoI), passed on to the LVL2 trigger. The LVL2 trigger refines the selection by making use of the RoIs and, if necessary, full detector information within these. Thanks to the RoIs, the amount of data passed on to the LVL2 trigger can be reduced to a few percent of the full event data. Events accepted by the LVL2 trigger are then passed on to the EF, with a rate of about 1 kHz.
In the end, the EF does the final refinement based on the full event data and more precise and detailed parameters, reducing the event rate to about 100 Hz. This final data is then transferred to long-term mass storage for later offline analysis.

5.8 Detector Simulation

Monte Carlo (MC) simulations are one essential part of experimental high energy physics. By using all knowledge about the detector and the physics behind, MC simulations *try* to emulate the outcome of particle collisions, to the highest precision possible. Thereby MC simulations can be used to study the detector and physics performance in detail. A general MC simulation consists of three parts: Event Generation, Detector Simulation and Digitisation.
The output created in the end should essentially look the same as the output produced by the real experiment, with the difference that the simulated data contains additional *truth* information about the particles generated in an event.
However, in reality even the optimal simulation might not completely agree with the data. Therefore the resulting data-MC mismatch is considered as a systematic error of the simulation, that has to be evaluated and minimised using e.g. control samples.

5.8.1 Event Generation

The main purpose of MC event generators is to simulate the details of a real *proton-proton* collision as precise as possible. This includes proper simulation of elastic scattering processes, multiple interactions, beam remnants effects and for hadronic interactions, the non-perturbative processes of parton showering and hadronisation and QED bremsstrahlung in the initial and final states.
In general, the theoretical calculations used in MC event generators are based on Quantum Field Theory (QFT), both Quantum Electrodynamics (QED) and Quantum Chromodynamics

(QCD) group theory as well as additional models predicting *new physics*. The most important methods used in these calculations are based on perturbative expansions. Using perturbative expansions, formulae for certain physical quantities (e.g. the cross-section of a specific channel) can be rewritten as an infinite sum of terms converging to an exact value or expression. This allows to approximate a formula to any precision, depending on the number N of subsequent terms included in the sum (asymptotic approximation). In QFT this expansion is usually done in powers of the coupling constants ($X = X_0 + X_1\alpha + X_2\alpha^2 + \ldots + X_N\alpha^N + \ldots$).
As an example, the *leading order* (0^{th} term) in QED already yields good approximations, due to the small value of the coupling constant $\alpha_{QED} \simeq \frac{1}{137}$ and in general it is not practicable to go above 3^{rd} order in QED.
In some cases the sum can be simplified and/or optimised (faster convergence) by taking into account only the leading terms up to a higher order, or by summing these leading terms up to infinite order into an analytical expression. The so-called *leading logarithms* approximation is just one common example.
One generator model based on this leading logarithms approximation is the model of parton showers. In this model the event is described in a first step as a $2 \to n$ partons process, followed by a second step where additional partons are generated from the incoming and outgoing parton lines limited by the energy scale of the event. These secondary partons are, due to correlation effects, arranged in cones around their *ancestor*-partons, yielding a shower-like structure and giving the model its name. After this step, the event contains a various number of quarks and gluons as well as other particles (e.g. leptons) produced in the hard process. In a final step, called hadronisation, the quarks are grouped to form hadrons (e.g. protons). Examples for parton shower generators (PSG) are PYTHIA [Sjo] and HERWIG [CKM+01], both differing in the way limiting the showering process.
For reasons of completeness another group of MC event generators, called matrix-element generators (MEG), being based on complex tree-level calculations and yielding *exact*, systematic expansions in α_{QCD}, should be mentioned.
In addition to the classification into PSGs and MEGs, MC event generators can be grouped into *universal* and *dedicated* generators. The former ones, such as PYTHIA or HERWIG, cover a wide range of processes at the price of demanding a significant number of approximations. While the latter ones, such as KORALZ or TAUOLA, are dedicated to a small set of related physical processes, including higher-order corrections and therefore yielding more precise results.
Finally, there are so-called *content-enhancing* generators, which complement the output of a universal host-generator. One of these generators, adding QED radiative corrections in particle and resonance decays in form of photons to the event, is called PHOTOS [GW06]. Since a combination of PYTHIA and PHOTOS was used for the purpose of this thesis, a more detailed discussion will be given in Section 7.2.
For convenience and consistency the event-generation phase is usually not part of the full simulation chain, but run separately, to create input that can be used several times.

5.8.2 Full Simulation

In the ATLAS Full Simulation the initial information obtained from the event-generation level is passed through a computer simulation of the detector, provided by the GEANT package [GEANT93]. This includes a *precise* description of the detector geometry (position, dimension and material of all detector parts) as well as a simulation of all sorts of physics processes,

caused by the interaction of the particles with the detector material. Processes from energies in the eV region (e.g. ionisation in gases) up to the TeV region are taken into account, to provide a detector-response model as realistic as possible. Due to this very sophisticated process (especially the shower simulation in the calorimeters) the detector simulation is a very time-consuming step in the ATLAS simulation chain.
In the following Digitisation step, the previously obtained information is now re-processes in order to emulate the original detector electronics output, produced by the real experiment. As a result of this Digitisation the same reconstruction and physics analysis tools can be used for simulated and real data.

5.8.3 Reconstruction

The reconstruction process is done in two sequential steps. In a stand-alone reconstruction step, data from single detector parts is used to reconstruct e.g. track segments in the Muon System or the ID, or the E_T^{miss} vector from the calorimeter cells. In the following combined reconstruction step information from several detectors is combined, e.g. matching of track segments of two different detectors, to provide an accurate measurement and identification of final objects, such as photons, leptons and jets.

5.8.4 Fast Simulation

To overcome the problems of the very time and CPU-time demanding full simulation, a Fast Simulation, called ATLFAST [ATLb], has been created. It allows for fast and easy detector-performance studies as well as estimations of signal to background rates for specific channels. In addition it is also the only practical way for high-statistics studies.
Instead of simulating all ATLAS subdetectors and their individual response, ATLFAST uses simplifications and smearing routines, based on detector-dependent parameters, estimated by full simulation and reconstruction. Due to the fact that not all detector effects can be easily parametrised and only a simple detector model is used, in fast simulation some effects, like the energy isolation of leptons, are only roughly simulated.
Since the event reconstruction is already included in the Fast Simulation, its output can directly be used for physics analyses.
One specific implementation of ATLFAST combined with PHOTOS was used for the purpose of this thesis and is therefore discussed in more detail in Section 7.2.1.

Part III

Analyses

Chapter 6

Analysis on Combined Test Beam

This study describes the mapping and optimisation of the Particle Identification (PID) in the Transition Radiation Tracker (TRT) of ATLAS. The TRT and other subdetectors of ATLAS, used in this study, have previously been described in Sections 5.4 and 5.5. This analysis is based on real data measured, at the H8 beam line at CERN, during the Combined Test Beam (CTB) running period in fall 2004. The differences and commonalities between the CTB and the real ATLAS setup will be pointed out in the following section.
Based on the fact that the simulation of the TRT, yet does not correspond to the CTB data and that a non-TRT separation between electrons and pions can be obtained by using other detectors in the CTB setup, this study waives on simulated data and can rather be used as an input to reach a more accurate simulation of the TRT response.
The primary goal of the TRT PID is the separation between electrons and hadrons, mostly pions[1]. In addition it might also be used to distinguish electrons from jets of particles. Due to tracking inefficiency, low charged particle multiplicity and large fractions of electromagnetic energy (photons from π^0 decays), these jets can appear like electrons. However, the e/jet separation to a large extend boils down to the e/π separation. Owing to the obvious lack of jets in CTB this is not part of this study. Finally, the TRT PID should be efficient at finding (possibly soft) electrons in b-jets, again requiring good e/π separation. Especially at low energies the TRT plays an essential role, as the calorimeter is not very efficient in that range.

Figure of Merit

The optimal figure of merit in this study is the pion efficiency (ε^π) or pion rejection ($R_\pi \equiv 1/\varepsilon^\pi$) as a function of electron efficiency (ε^e). These plots, containing all information regarding separation, will be used to compare the performance of different methods, whereas R_π or ε^π at 90% ε^e will be used when comparing performance as a function of energy. R_π at 90% ε^e is expected to be 15-200, depending on η [TDR97][2].

[1] Here and in the following, "pions" will be used as a generic word for "hadrons".
[2] These numbers can not be compared directly, since they are based on a different type of electronics.

6.1 Combined Testbeam 2004 Setup

During the CTB data-taking phase a phi sector of the ATLAS ID and calorimeter barrel was placed into beams of various particle types and energies (see Section 6.2). Due to economical reasons only the Pixel Detector, represented by six modules in three layers, and the SCT, represented by eight modules in four layers, were place inside a magnetic field. The TRT, in difference to the real ATLAS setup (see chapter 5), was kept outside the magnetic field and moved away from the SCT, due to the extension of the magnet coil. The TRT phi sector consisted of six modules in two barrel wedges and three layers (see Figure 6.2). During the considered data taking period two TRT setups were used, such that the straight beam was centred to the three lower modules at low energy (up to 9 GeV) and to the three upper ones at high energy (20 GeV and above).
Runs were taken with and without magnetic field (in Pixel and SCT) and with and without additional material inserted into the beam between the ID parts. At low energies the magnetic field was set proportionally to the beam energy such that 9 GeV runs had a B-field of 1.4 Tesla, while at higher energies this value was simply maintained. The material inserted into the beam, consisting of two aluminium plates, one in front (10 mm plate) and one behind (20 mm plate) the SCT, correspondes roughly to a doubling of the total ID material.
A schematic drawing of the CTB beamline setup, illustrating the position of the various elements, is shown in Figure 6.1. A more complete description of all elements in the CTB setup can be found in [DGGK05].

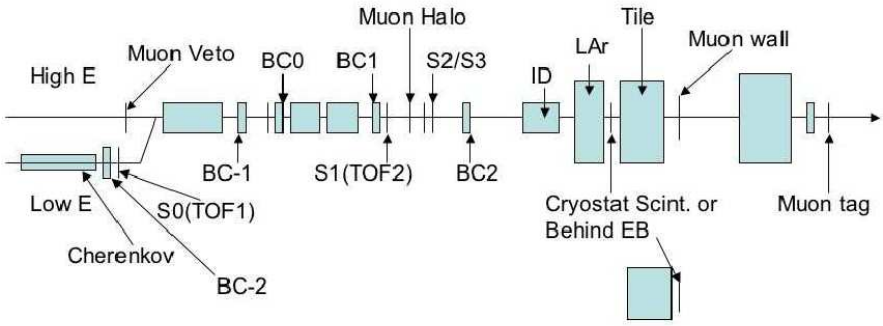

Figure 6.1: A schematic drawing of the beamline setup in CTB 2004 [DGGK05]. All elements are represented by blocks not drawn to scale.

6.2 Data Sets

The data used for the study on e/π separation covers the energy range from 2 to 180 GeV and therefore allows to gain good knowledge of the energy sensitivity. If available, runs with and without B-field and additional material were used for each energy, to study a possible effect on the PID.
For the measurement of the Transition Radiation (TR) onset additional muon runs at 150 and 350 GeV were included and due to the lack of intercalibration data between the two TRT setups, some corrections have been applied (see Section 6.5).

Run	$E[GeV]$	$B[T]$	M	$\langle N_{LT} \rangle$	N_{run}	N_{cuts}	N_π	N_e	N_μ
115	2	0.00	out	36.38±0.03	50000	25105	3178	15755	157
164	2	0.00	in	35.40±0.05	50000	13771	1908	7733	134
118	2	0.33	out	34.43±0.03	50000	21603	3500	8692	130
149	2	0.33	in	33.36±0.05	50000	10601	2309	3224	93
098	3	0.00	out	37.17±0.03	50000	26873	5547	16684	0
162	3	0.00	in	36.15±0.04	50000	19714	4737	10978	11
114	3	0.49	out	34.45±0.03	50000	27146	7264	9761	11
147	3	0.49	in	33.72±0.04	50000	15314	5509	4039	3
097	5	0.00	out	37.41±0.03	50000	32316	12092	14190	0
163	5	0.00	in	36.82±0.03	50000	26101	10972	10094	2
106	5	0.82	out	35.10±0.02	50000	33862	15598	7660	2
151	5	0.82	in	34.47±0.03	50000	20886	16872	3	4
103	9	0.00	out	37.44±0.02	50000	39649	14134	8369	113
139	9	0.00	in	37.21±0.03	50000	31371	11563	5696	87
107	9	1.40	out	33.16±0.02	50000	38830	13196	5146	5
150	9	1.40	in	33.47±0.02	50000	26769	12165	7	5
397	20	0.00	out	32.83±0.02	50000	41500	2378	31817	271
305	20	0.00	in	32.81±0.03	39074	21323	1941	14918	214
446	20	1.40	out	27.98±0.31	45794	241	2	140	0
297	20	1.40	in	28.90±0.32	50000	314	2	153	0
410	50	0.00	out	33.75±0.02	50000	39815	6105	27254	12
291	50	0.00	in	34.19±0.02	50000	26557	6422	15885	11
400	50	1.40	out	27.68±0.19	50000	733	45	562	0
292	50	1.40	in	28.94±0.15	50000	1178	53	879	0
454	80	0.00	out	34.38±0.02	50000	39156	6989	24891	33
452	80	1.40	out	27.71±0.07	50000	3772	913	2105	6
398	100	0.00	out	33.89±0.02	40000	32031	8017	16520	509
249	100	0.00	in	34.25±0.02	50000	29315	10817	11497	853
399	100	1.40	out	27.76±0.05	50000	7769	2577	3422	176
245	100	1.40	in	28.14±0.06	50000	6426	2437	2026	290
433	150	0.16	out	36.10±0.02	27219	24683	414	0	21590
434	150	0.16	out	35.78±0.02	29486	26922	2919	0	21300
461	180	0.00	out	33.95±0.02	50000	44097	20683	6090	2439
217	180	0.00	in	34.39±0.02	50000	32808	21548	0	2938
462	180	1.40	out	32.73±0.02	49265	31977	16181	3010	1967
463	180	1.40	out	31.25±0.02	50000	27920	13223	2433	2172
541	180	1.40	out	33.64±0.03	50000	15915	243	0	15087
195	180	1.40	in	31.03±0.02	50000	24730	11365	883	5842
730	350	0.16	out	35.42±0.01	50000	48589	61	0	46029
731	350	0.16	out	34.57±0.02	30494	29543	47	0	27932
728	350	1.40	out	34.57±0.02	46416	45098	62	0	42671

Table 6.1: Table showing all used runs, with their run-number (2102*), energy (in GeV), B-field (in T), material status, average number of LT hits, number of events N_{run}, number of events after cuts N_{cuts} and numbers of pions, electrons, and muons (N_π, N_e, N_μ)

All data has been reconstructed into Combined Ntuples (CBNT[3]) using the ATLAS software version 11.0.42. A complete list of runs used in this analysis, including their energy E, B-field, material status M, average number of LT hits $\langle N_{LT} \rangle$, number of events in file N_{file} and after cuts N_{cuts}, and statistics for each particle sample (N_π, N_e, N_μ) is given in Table 6.1. The reconstruction efficiencies are very low at runs with high energy and magnetic field, which was due to an error in the recontruction code [InD] [Dri].

6.2.1 Data Quality Assurance

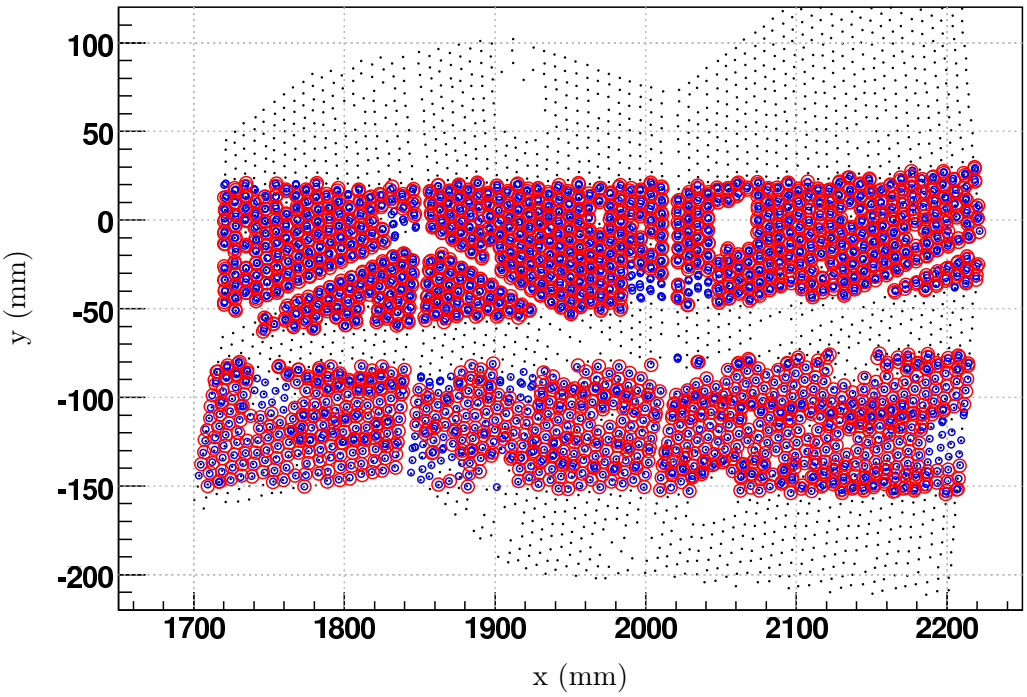

Figure 6.2: TRT modules and mapping of straws in three classes: straws hit at least once (black dot), straws hit at least one hundred times (small blue circle) and straws fulfilling all quality criteria and used for analysis (big red circle). The lower ones at low energies (2, 3, 5 and 9 GeV), the upper ones at high energies (20, 50, 80, 100, 150, 180 and 350 GeV) or at low energies with B-field.

To exclude noisy, dead, and miscalibrated straws from this analysis certain quality requirements had to be fulfilled for each individual straw in the TRT. As a statistical requirement, only straws with at least 100 identified electron and pion hits were considered. Furthermore, only straws with a probability to have a HT hit for an electron (p_e^{HT}) being at least 50% higher than that for a pion (p_π^{HT}) and the latter one being below 12.5% are kept for this study. These two cuts are illustrated in Figures 6.3a and 6.3b, showing scatter plots of the straw hit statistics and HT probabilities for electron and pions, respectively. As can be seen, there is a linear correlation of about 30% between the HT probability for electrons and pions. This is due to small variations in the setting of the actual HT value in the DTM/ROC chips

[3] An assignment of variable names used in this text to CBNT variables can be found in Table B.1.

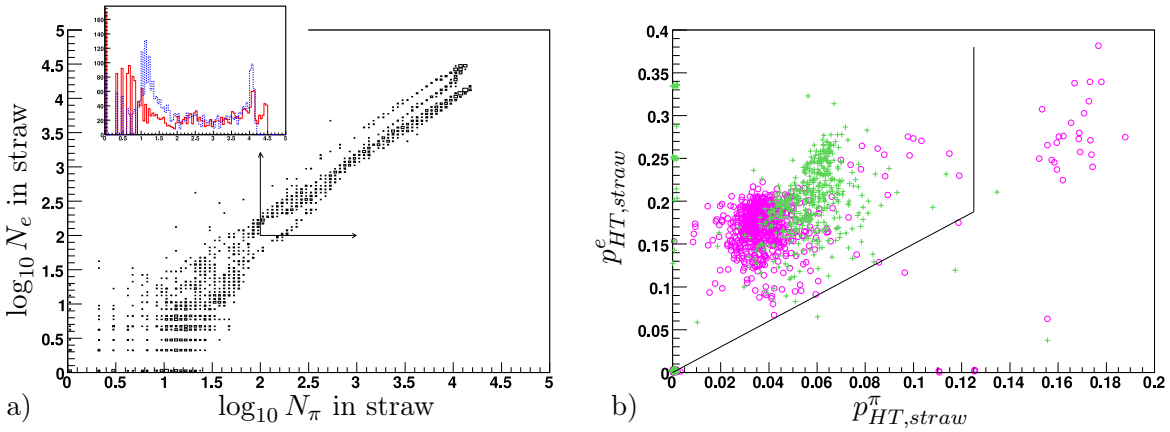

Figure 6.3: Distribution of (a) hit statistics and (b) HT probabilities for electrons and pions in straws. To assure the straw quality, each straw is required to have at least 100 electron and pion hits, p_e^{HT} at least 50% higher than p_π^{HT}, and $p_\pi^{\mathsf{HT}} < 12.5\%$. [$\pi$: dashed blue, e: solid red; low energies: purple circles, high energies: green crosses]

on the front-end electronics.
In addition to this straw based quality requirement, only events with exactly one global track (i.e. a track seen and matched between the Pixed detector, the SCT, and the TRT) with at least 20 quality TRT hits have been selected[4]. Thereby avoiding interference from other effects and assuring sufficient statistics, respectively.
Figure 6.2 shows a mapping of all straws involved in this study. Of the 3284 straws in the six TRT modules, 2911 show activity, i.e. have at least one hit (black dots). Only 1355 of those pass the requirement of sufficient statistics (blue circles), since not all straws were exposed to the direct beam. Applying the straw quality requirement this number reduces to 1272, the final number of straws used for the analysis (red circles).

6.2.2 Non-TRT Separation

Name	Description	Typical e	Typical π	Typical μ
EMF1	Energy fraction in 1. LAr calo. sampling	0.45/0.18	0.02/0.005	0.005/0.0
LArF	Energy fraction in LAr calo.	0.84/0.93	0.17/0.08	0.05/0.0
HadF	Energy fraction in Tile calo.	0.0	0.25-0.45	0.2/0.0
Cher	Number of Cherenkov counts	650-2000	570±20	570±20
MuTag	Muon tag from muon system	400±15	400±15	520-900

Table 6.2: Non-TRT separation variables from the Liquid Argon (LAr) calorimeter, the Tile calorimeter, the Cherenkov counter, and the Muon system. Typical values are quoted for electrons, pions, and muons, with ranges indicated with a "-", energy changes with a "/", and specific peaks with a "±".

[4]The 20 quality TRT hits on a sigle track requirement is very loose and allows almost all events to enter the analysis.

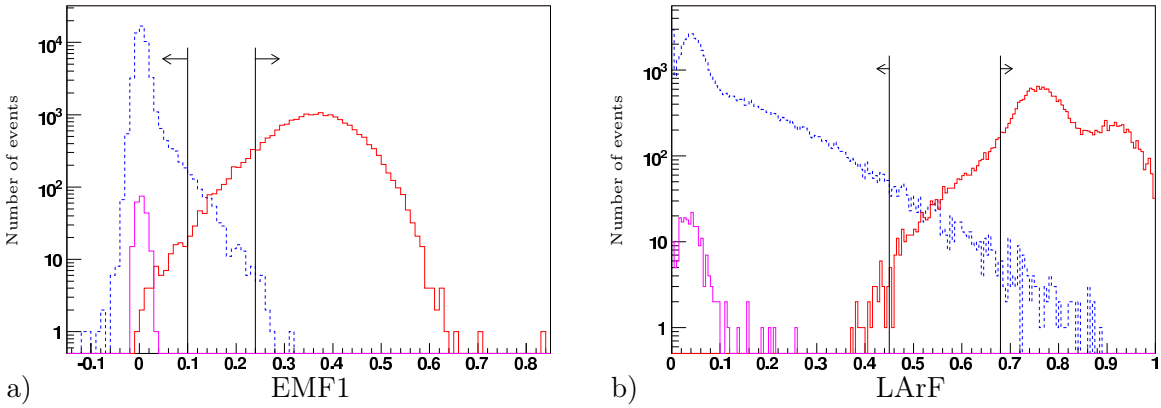

Figure 6.4: Distribution of the fraction of energy deposited a) in the first sampling (EMF1) and b) the entire cluster (LArF) in the Liquid Argon calorimeter at 9 GeV. Each curve is obtained by applying cuts to the three other separation variables. The cuts on the variable shown are indicated with vertical lines and arrows. [π: dashed blue, e: solid red, μ: solid violet]

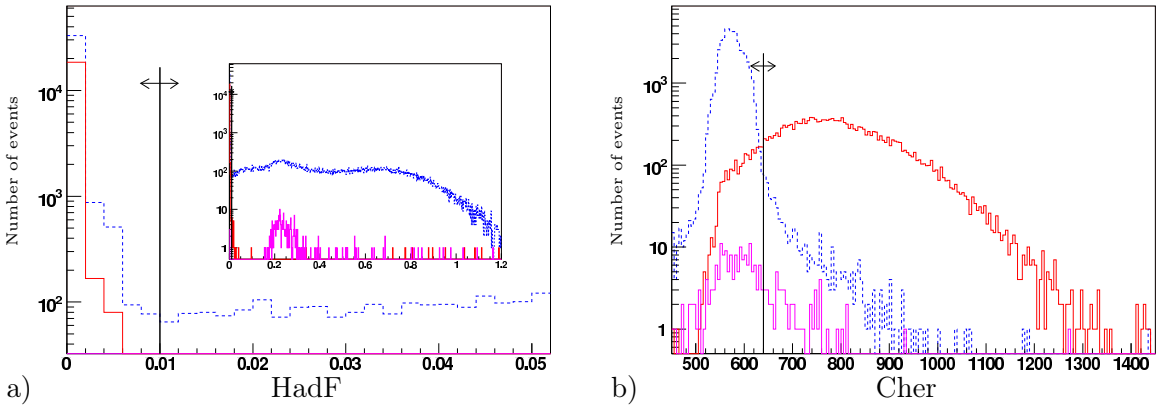

Figure 6.5: Distribution of a) the energy fraction in the Tile calorimeter (HadF) and b) the Cherenkov variable (Cher) at 9 GeV. Each curve is obtained by applying cuts to the three other separation variables. The cuts on the variable shown are indicated with vertical lines and arrows. [π: dashed blue, e: solid red, μ: solid violet]

To be able to test the TRT PID without simulated data one needs large clean separate samples of electrons and pions, obtained from non-TRT discriminating variables. For this purpose the ATLAS calorimeters, also being part of the CTB setup, as well as additional CTB detectors were used. The fraction of energy deposited in the first sampling and the entire cluster in the Liquid Argon calorimeter, described by the variables EMF1 and LArF, respectively, provide good separation. Additional information is provided by a Cherenkov counter (Cher) at lower energies (2-20 GeV) and the energy fraction in the hadronic calorimeter (HadF) at higher

energies (20-180 GeV). The Cherenkov counter is not used at high energies since no separation is obtained in that region. Since almost no energy is deposited the Tile calorimeter at low energies, the same is to be deemed for the HadF variable for <20 GeV runs. The fraction of energy deposited in the first sampling (EMF1) decreases for both, electrons and pions, but faster for the latter, since more and more pions traverse through the electromagnetic calorimeter into the tile calorimeter. This is also the reason why LArF variable yields an increasing separation with rising energy.
To obtain clean samples of muons, used in the TR onset study (see Section 6.5), a muon tag (MuTag), provided by the CTB muon setup, was used.
By considering each variable in turn, the cutting values were obtained in an iterative process. Reasonable cuts were applied to all variables but the one in question, thereby yielding the distribution of this one and allowing for a tuning of its cut value. In the same manner the cut values have been optimised for all variables and particle types. A fairly optimal and well understood separation can be obtained by repeating the process until stable cuts are found. Since most cuts are energy dependent this optimisation was performed at all energies.
The distribution of the four e/π separating variables, EMF1, LArF, HadF, and Cher, with the relevant cuts applied to the other three variables for electrons and pions are shown at 9 GeV in Figures 6.4 and 6.5. The corresponding plots at other energies can be found in [MP06], [MP] and Appendix B (2 and 180 GeV). From these plots it can be seen that e.g. for electrons the total energy deposited in the electromagnetic calorimeter (LArF) increases with energy, while the fraction deposited in the first sampling (EMF1) decreases, in accordance to the selection cuts.
As always, choosing cuts is an interplay between efficiency and purity. The cuts chosen for this study, providing reasonably large samples (>1000 events) with good purities (> 98%), are given in Table B.2.
By measuring the signal and background efficiency (ε and β) for electrons and pions at each energy[5], shown in Table B.3, the purities of the data sample can be found. By comparing the number of events passing all other cuts than the one in question ($N^{e/\pi}_{\text{uncut}}$) with the number of events after that cut ($N^{e/\pi}_{\text{cut}(e/\pi)}$), four quantities can be calculated:

$$\varepsilon^{\pi} = N^{\pi}_{\text{cut}(\pi)}/N^{\pi}_{\text{uncut}}, \quad \varepsilon^{e} = N^{e}_{\text{cut}(e)}/N^{e}_{\text{uncut}},$$
$$\beta_{\pi} = N^{\pi}_{\text{cut}(e)}/N^{\pi}_{\text{uncut}}, \quad \beta_{e} = N^{e}_{\text{cut}(\pi)}/N^{e}_{\text{uncut}}.$$

As can be seen, each of the EM calorimeter variables reject more than 99% of the electron background in the pion sample, while retaining 90% of the pions. In addition, the Cherenkov counter (at lower energies) and the hadronic calorimeter (at high energy) further reject 90% and 99% of the electrons, respectively. Likewise, the pion background in the electron sample is reduced by 98% by each of the EMF1 and LArF cuts, the latter increasing with energy to more than 99%, while maintaining 90% efficiency. Again Cherenkov counter and hadronic calorimeter remove an additional 90% of the background at low and high energy, respectively. The muon sample, used in the TR onset study, is mainly based on the powerful MuTag variable, but has been cross checked by the LArF, HadF, and Cher variables.
Under the assumption of uncorrelated variables the overall purities could be obtain by a direct product of the background efficiencies multiplied by the ratio of the number of each particle type, as shown in the bottom two rows of Table B.3. Even though this assumption would be too optimistic, the linear correlations given in Table B.4, have been found to be

[5]This process was done on a run to run basis.

modest. A degradation of 5.5 in the separation has been numerically calculated using Gaussian distributions and the largest of the correlations (between EMF1 and LArF at 2 GeV) [MP06]. Taking this into account the sample purities have been assured to be better than 99.8%, which is more than needed for this purpose.

6.3 Variables and Methods

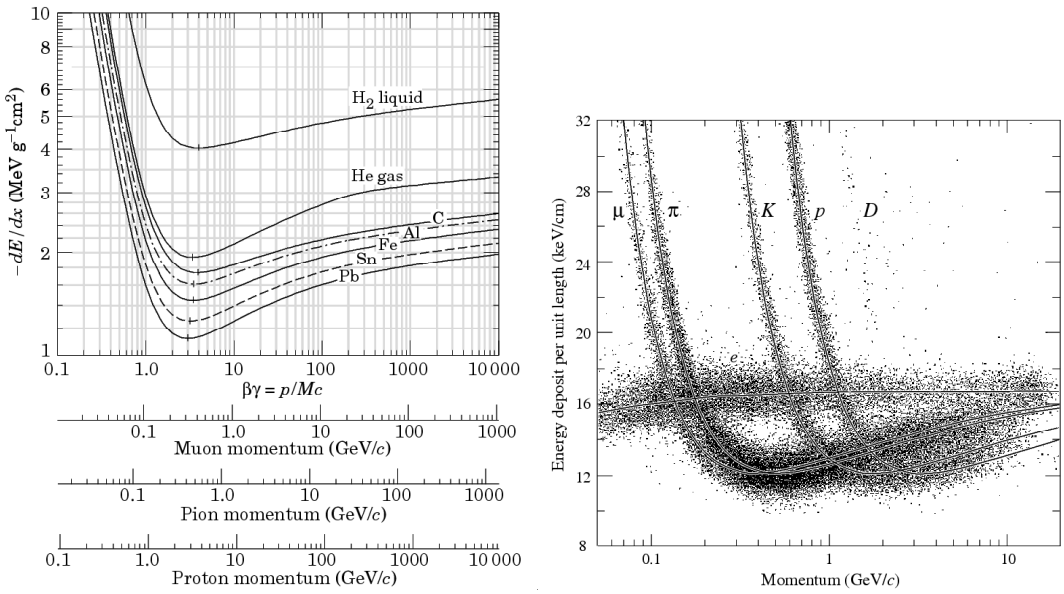

Figure 6.6: Plots illustrating the energy loss per unit length (dE/dx) for different particle types. Both plots do not contain the exact gas mixture of the TRT, but the shape (left) and the relative position of the graphs (right) would look the same. Left: Mean energy loss rate in liquid (bubble chamber) hydrogen, gaseous helium, carbon, aluminium, iron, tin, and lead. Radiative effects, relevant for muons and pions, are not included. [PDG06] Right: PEP4/9-TPC energy-deposit measurements (185 samples 8.5 atm Ar-CH_4 80-20%) in multihadron events. [PDG06]

Particle identification with the TRT is primarily based on the high threshold (HT) hits, mainly produced by transition radiation (TR), as discussed in Section 5.4.3. In addition to this the time-over-threshold (ToT) provides secondary separation, most notably at low energies.
This due to the different dE/dx (energy loss per unit length) behaviour of electrons and pions, illustrated in Figure 6.6. While at low momentum, electrons have already reached the Fermi plateau and are therefore *well* separated from pions, at higher momenta both particle types converge, resulting in worse separation.
In the following sections the two variables and their associated methods, as well as a possible combination, will be described separately. Due to obvious correlations between the two variables special care has to be taken when combining them. This issue will be discussed in more detail in Section 6.3.2 and 6.3.3.
Distributions shown in these sections are all at a representative energy of 9 GeV, obtained from runs with neither magnetic field nor material inserted into the beam. This is due to the fact that this was the best understood configuration, with least interference from other effects,

such as multiple scattering and tracking. Plots and results for all energies and the other three configurations can be found in Appendix B (2 and 180 GeV) and in [MP].

6.3.1 High Threshold Information

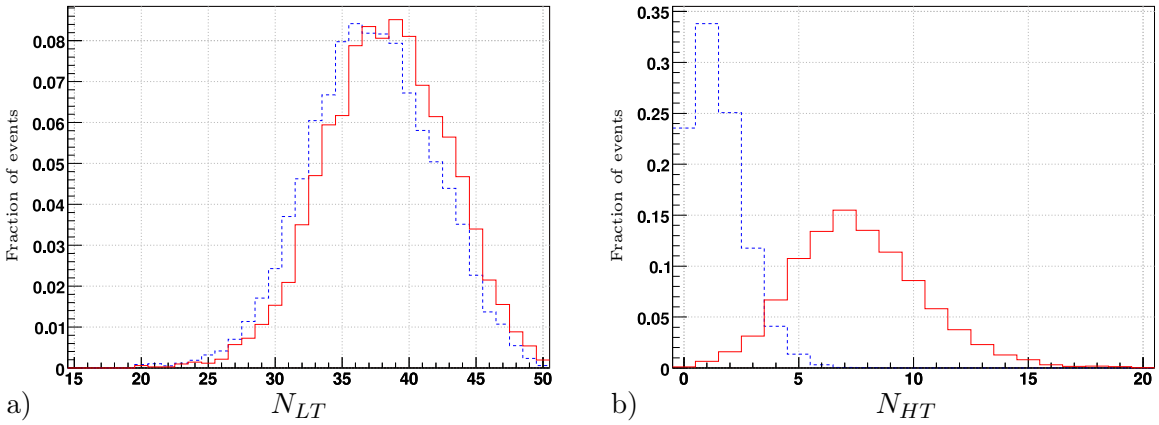

Figure 6.7: Distribution of number of LT and HT hits on tracks at 9 GeV. a) Number of LT hits on track, b) Number of HT hits on track [π: dashed blue, e: solid red]

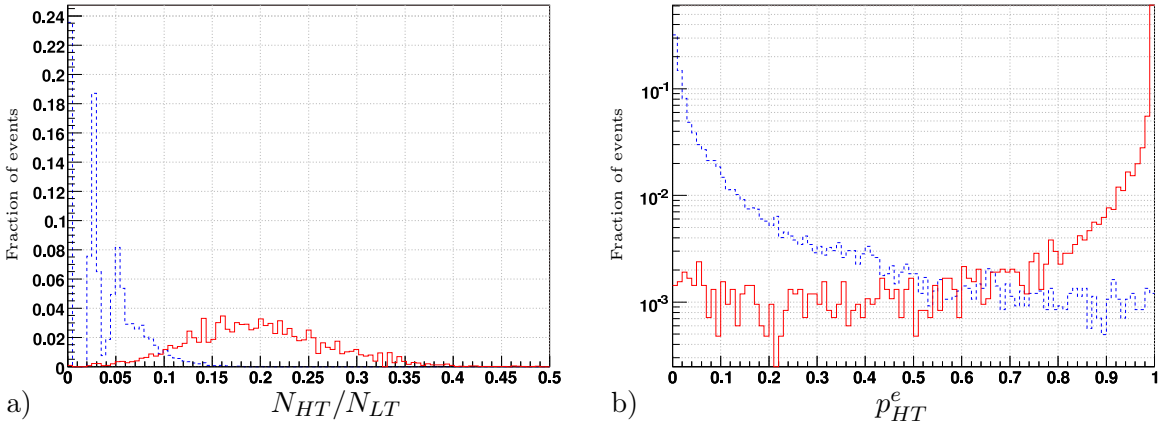

Figure 6.8: Distribution of a) N_{HT}/N_{LT} and b) likelihood variable using the HT information for electrons and pions at 9 GeV. [π: dashed blue, e: solid red]

As mentioned before, the occurrence of a HT hit in a straw signifies an increased amount of TR, essentially only emitted by electrons. Based on this, the number of HT hits on a track (N_{HT}) can be used for electron identification. However, HT hits can also be produced by other particles, mostly because of Landau fluctuations in the dE/dx and/or δ-rays[6], which as

[6]Electrons, knocked out of atoms by fast energetic charged particles, that have sufficient energy to ionize further atoms through subsequent interactions on their own.

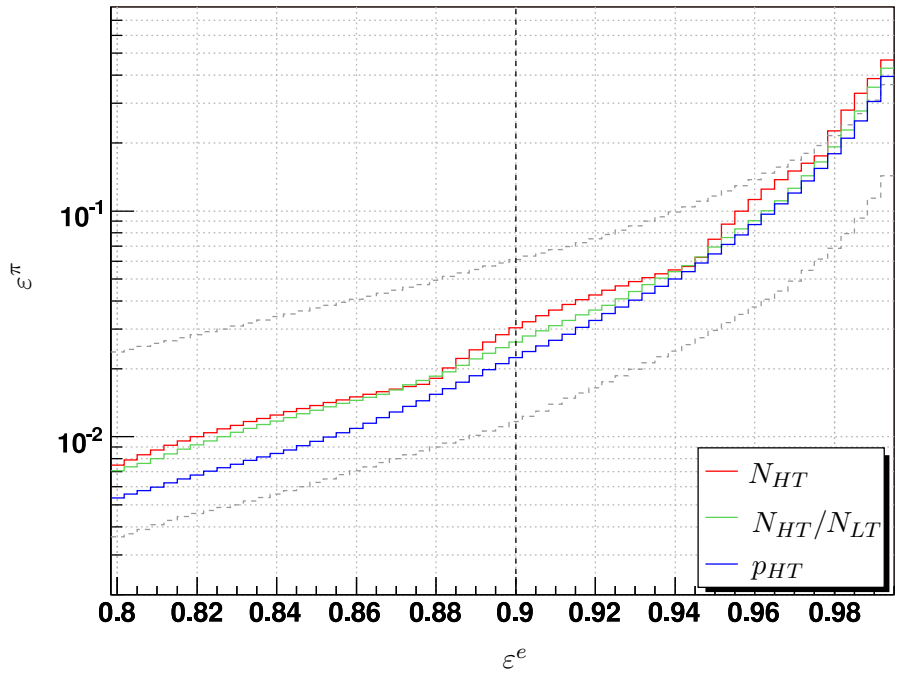

Figure 6.9: π-efficiency over e-efficiency for HT methods at 9 GeV. The dashed grey lines represent 2 and 2.5σ separation.

a result decreases the separation. A typical distribution of N_{HT} for both pions and electrons, is shown in Figure 6.7b.

While providing reasonable (and currently the only) separation, this very simple variable has two shortcomings. First of all, each track does not hit the same number of straws (see Figure 6.7a), and secondly not all straws have the same probability of giving a HT hit, as shown later in this section.

The first shortcoming can be eliminated by normalising N_{HT} with the number of low threshold hits N_{LT} on track (see Figure 6.8a). Using the N_{HT} as a discriminator corresponds to using the same (average) electron and pion probability for all straws. This is valid, but the larger the variations between straws, the less optimal does the counting of HT hits become.

The second, more subtle deficiency requires knowledge of the electron and pion HT hit probabilities in each single straw, $p^e_{HT,i}$ and $p^\pi_{HT,i}$. Having a map of these probabilities, the probability for a track to originate from an electron can be calculated from a likelihood as follows:

$$p^e_{HT} = \frac{\prod_i p^e_{HT,i}}{\sum_{j=e,\pi} \prod_i p^j_{HT,i}}. \tag{6.1}$$

Thereby the product of probabilities is normalised to the probability of all possible particle types, being only electrons and pions in this study. It is actually the variations of the probability for a HT hit between the straws (see Figure 6.3b) that the likelihood variable p^e_{HT} includes to get a better e/π separating. An exemplary distribution of p^e_{HT} is shown in Figure 6.8b for both electrons and pions.

A comparison of all HT based methods, given by a π-efficiency over e-efficiency plot, is shown

in Figure 6.9. As can be seen the normalisation gives a slight improvement, but still the likelihood method yields the best separation (about 2.3σ) of all HT based methods.

Parametrisation of the HT hit probability

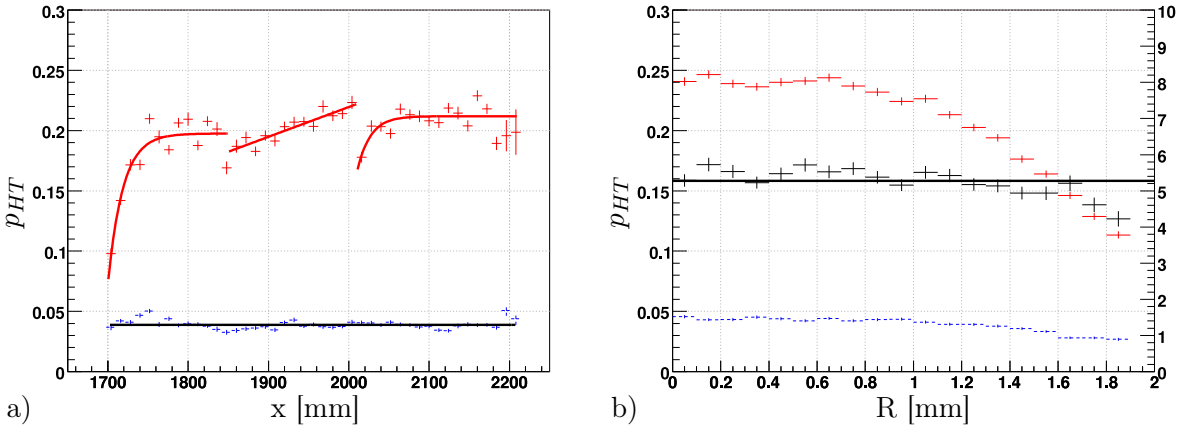

a) b)

Figure 6.10: Geometric dependency of the HT probability at 9 GeV, a) as a function of x (depth in the detector). $\frac{\chi^2}{N_{Dof}}(e) = \frac{91.3}{10}, \frac{14.6}{10}, \frac{55.3}{14}$. $\frac{\chi^2}{N_{Dof}}(\pi) = \frac{152.9}{42}$. b) as a function of R (distance track-anode). $\frac{\chi^2}{N_{Dof}}(\pi) = \frac{66.4}{18}$. [$\pi$: dashed blue, e: solid red, ratio between e and π: black]

The likelihood approach requires knowledge of the HT probability for each particle type in each straw. This can be realised by using a database of HT probabilities for each particle type and straw, or a parametrisation of these. The latter one is only possible in case the HT probability variations are due to global effects and not simply individual variations between straws. Still this approach would require the database values to obtain the parametrisation by fitting to them. The advantage of a parametrisation would be a loss of sensitivity against statistical fluctuations.

The most distinct HT probability variation is with the distance a particle had to build up TR. This is primarily given by the distance to the last TR photon absorbing *wall* between the modules of the TRT. The TR requires some distance to build up, and in the same manner the HT probability. Due to the setup of the TRT (see Figure 6.2), basically only the walls between radial sequenced modules play an important role in CTB. This means that in reality a variation with the TRT entry position could be possible. The HT probability as a function of r (simply x in CTB) is given in Figure 6.10a, indicating the position of these dividing walls and the caused subsequent build-up. The fit (also shown in the figure) is performed at each energy, as p^e_{HT} varies slightly with the momentum of the particle. It also shows that the pion probability is flat and therefore caused by noise and that the single straws are not alike, thus favouring the single straw likelihood approach.

Another parameter that has in influence on the HT probability is the track distance to the anode (R), as shown in Figure 6.10b. However, since the ratio between electrons and pions (black curve in the figure) remains constant with R, this can be regarded a purely geometrical effect, not containing any PID information.

It has also been invertigated whether the probability for a HT hits is influenced by the occurance of a HT hit in the straw in front of the one in question. Since the TR takes some length to build up (as seen in Figure 6.10a), the loss of TR photons yielding a HT hit might reduce the probability for a HT hit in the following straw. It could be shown that this is not the case and that no significant difference is obsevred:

$$p^e_{HT}(\text{without hit in front}) = 0.1670, \quad p^\pi_{HT}(\text{without hit in front}) = 0.0403,$$
$$p^e_{HT}(\text{with hit in front}) = 0.1743, \quad p^\pi_{HT}(\text{with hit in front}) = 0.0486.$$

Other less significant effects, such as the angle (i.e. the path length) in the straw (see Figure 5.7), or the B-field changing the drift path in the straws, could in principle also vary the HT probability, but have not been investigated in this study, since the data with these variation was not available.

6.3.2 Time-over-Threshold Information

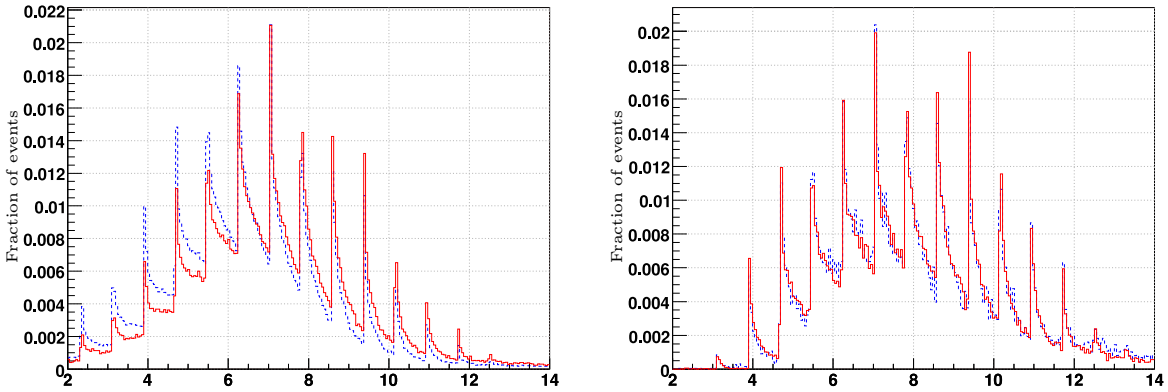

Figure 6.11: ToT normalised by the length the track traversed through the straw for straws a) without and b) with a HT hit for electrons and pions at 9 GeV. As can be seen, the straws with a HT hit does not carry any more separation power in the ToT variable (i.e. the electron and pion curves are the same). The jagged structure is due to the discrete ToT values. [π: dashed blue, e: solid red]

One essential part of this study was the idea to include information based on the ToT variable, since it was expected to increase the separation, especially at low energies.
The ToT is very dependent on the length a particle traversed through a straw, since that is proportional to the number of ionisations in the gas. In this study the length of the according track in the straw (L) is used to normalise the ToT, and thus compensating for this geometrical effect. By doing so, only the part that is due to the difference in dE/dx between electrons and pions can be extracted from the ToT.
An illustration and calculation of L is shown in Figure 5.7, assuming $\sin\theta \simeq 1$ for the CTB setup. Figure 6.11 shows the distribution of the normalised ToT (ToT/L) for the two cases where only hits that a) did not have a HT tag and b) did have a HT tag where considered.

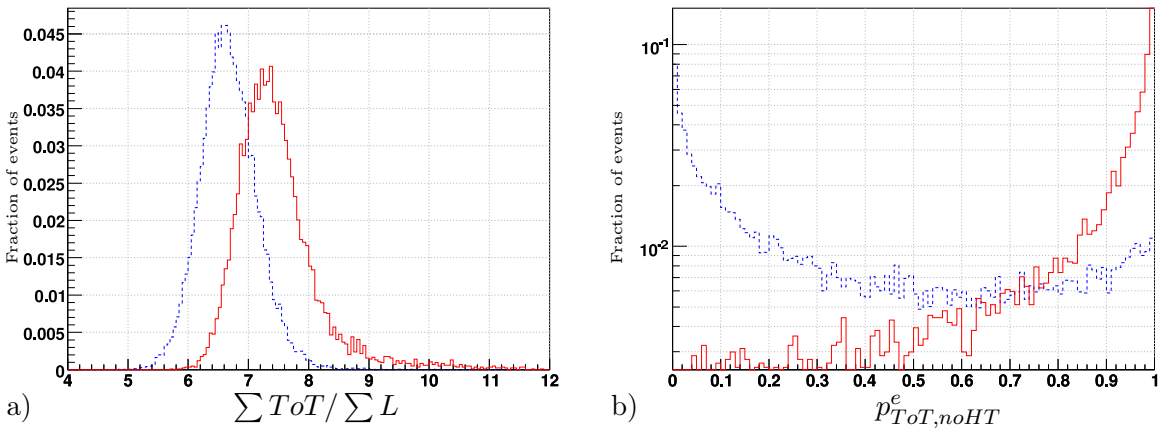

Figure 6.12: a) ToT sum of all hits on track normalised by the sum of all L (length of track in straw), and b) probability for being an electron using a HT likelihood method for electrons and pions at 9 GeV. [π: dashed blue, e: solid red]

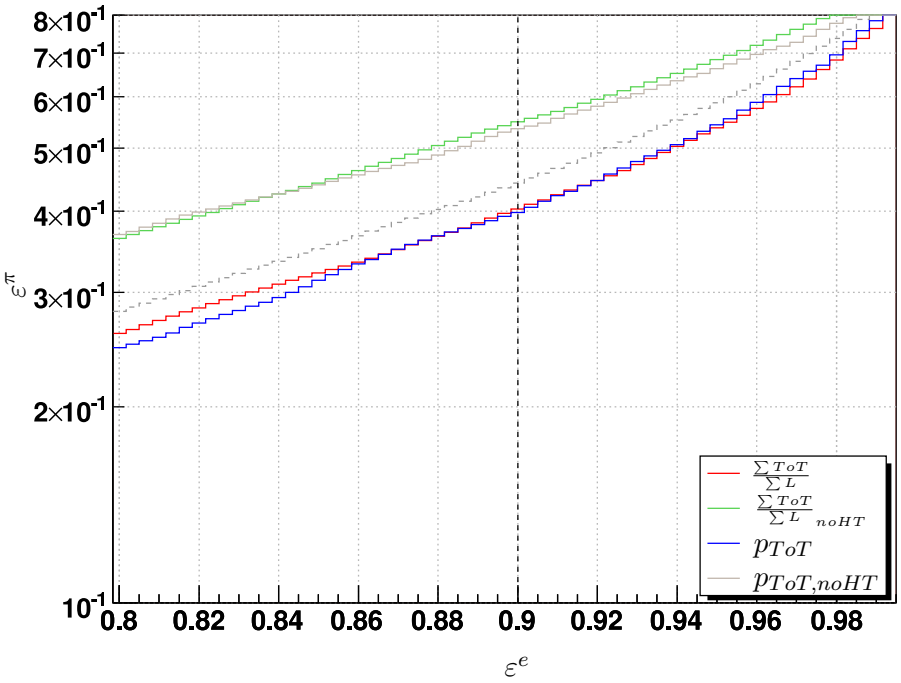

Figure 6.13: π-efficiency over e-efficiency for ToT methods at 9 GeV. The dashed grey line represents 1σ separation.

The momentum dependency of the ToT is almost negligible for electrons, but plays an important role for pions. Due to its rise with momentum, the dE/dx of large momenta pions approaches the one of the electrons and thereby diminishes the separation between the two, based on ToT (see Figure 6.6).

Given the ToT and the track length in straw (L) for all hits on track (N_{LT}), several possible discriminating variables, such as $\sum ToT/N_{LT}$, $\sum ToT/L$ and $\sum ToT/\sum L$, have been investigated, showing that only the latter one gives reasonable good separation. An example distribution of $\sum ToT/\sum L$ is shown in Figure 6.12a.
However, similar to the HT case, a more powerful method can be obtained by using the information from each single straw in a likelihood approach:

$$p^e_{ToT} = \frac{\prod_{i,noHT} p^e_{ToT,i}}{\sum_{j=e,\pi} \prod_{i,noHT} p^j_{ToT,i}}. \tag{6.2}$$

Again, this requires a database (map) of, in this case, TRT ToT responses. Contrary to the HT case, the ToT information is a detailed distribution and thus much more disk space and computing time demanding. Even though it would certainly not reach the level of e.g. the Liquid Argon consumption, the effort can be reduced under the assumption that all straws behave the same way, in terms of ToT/L at the same energy. However, due to the non-negligible impact of the large HT signal on the ToT, a distinction is made between straws that did not or did have a HT hit, shown in Figure 6.11a and 6.11b, respectively. The distribution of likelihoods obtained with the ToT method not using HT hits, is shown in Figure 6.12b.
A comparison of all ToT based methods (with reasonable separation) is given in Figure 6.13. It can be seen from the plot that excluding the straws, having a HT hit, lowers the separation in both methods by approximately the same factor. The advantage of still using theses methods will be discussed in the next section.

6.3.3 Combined Approach

Knowing the optimal separation methods based on both the HT and the ToT information, a combination of them might offer the best pion rejection possible. A straight forward combination can only be done, in case the two variables are largely uncorrelated. To ensure this, only straws that did not have a HT hits were included in the ToT likelihood product (see Equation 6.2). Since it has been shown that ToT information of the straws with HT hits does not carry significant separation (see Figure 6.11b) the advantage of reducing the correlation overcomes the disadvantage of a slightly smaller separation (see Figure 6.13). The linear correlations between $p^{e,\pi}_{HT}$ and $p^{e,\pi}_{ToT,noHT}$ are given in Table B.5 as a function of energy.

$$p^e_{all} = \frac{p^e_{HT} p^e_{ToT}}{\sum_{j=e,\pi} p^j_{HT} p^j_{ToT}} \tag{6.3}$$

The distribution of the combined discrimination variable, calculated in Equation 6.3, is shown in Figure 6.14 (insert). A final comparison of all methods of interest, including the combined one, is given in Figure 6.14, in form of a π-efficiency over e-efficiency plot.

6.4 Discussion

The algorithms for e/π separation described and illustrated, for an representative energy of 9 GeV, in the previous sections were applied at all energies. Using the pion efficiency at 90% electron efficiency (indicated by a vertical dashed black line in all efficiency comparison plots) as a figure of merit, the separation as a function of energy is given in Figure 6.15. As can

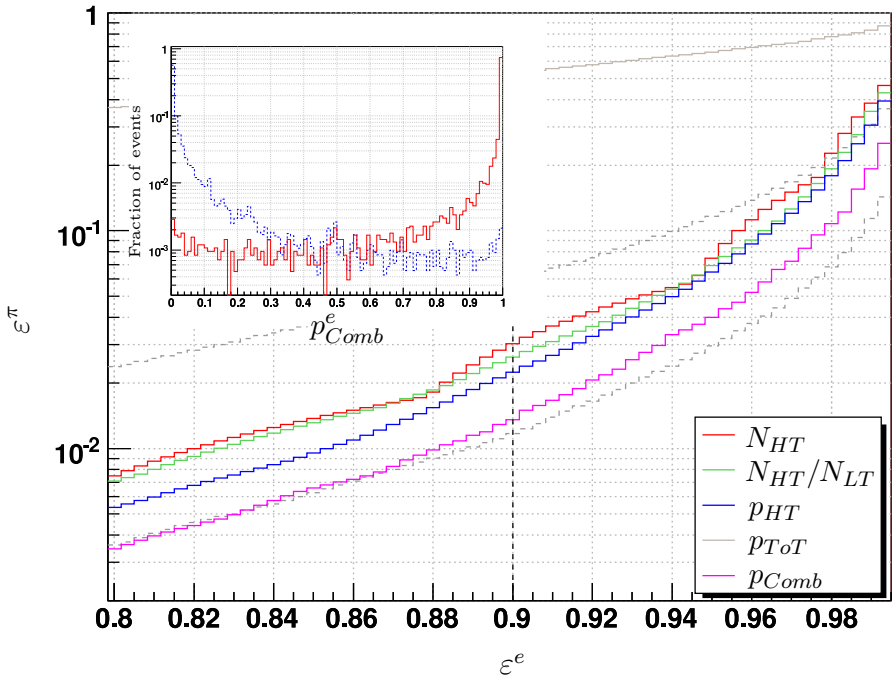

Figure 6.14: Distribution of the p^e_{Comb} (insert) and π-efficiency over e-efficiency plot for all methods at 9 GeV. The dashed grey lines represent 2 and 2.5σ separation.

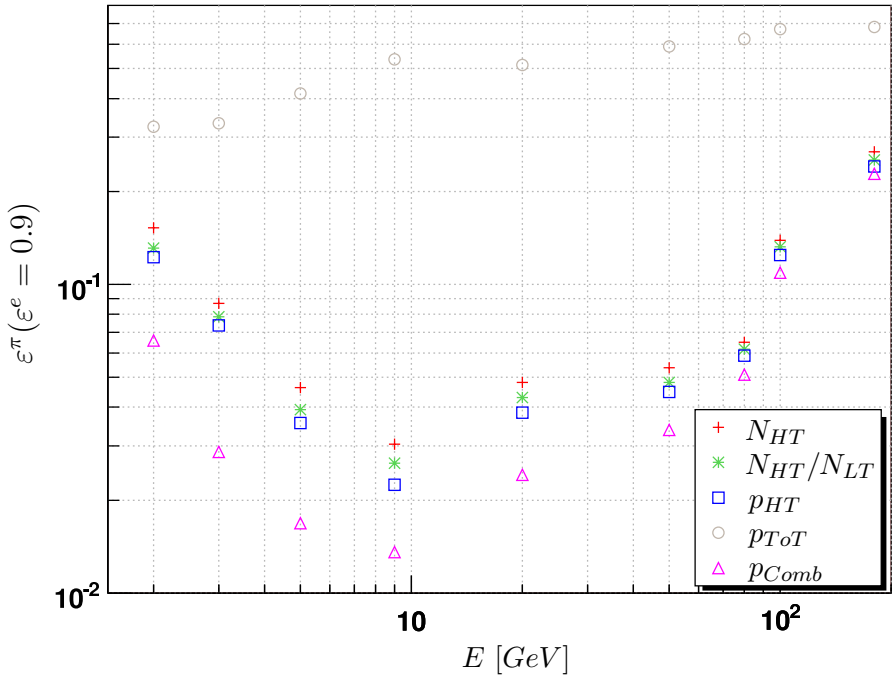

Figure 6.15: π-efficiency at 90% e-efficiency in absolute values as a function of energy.

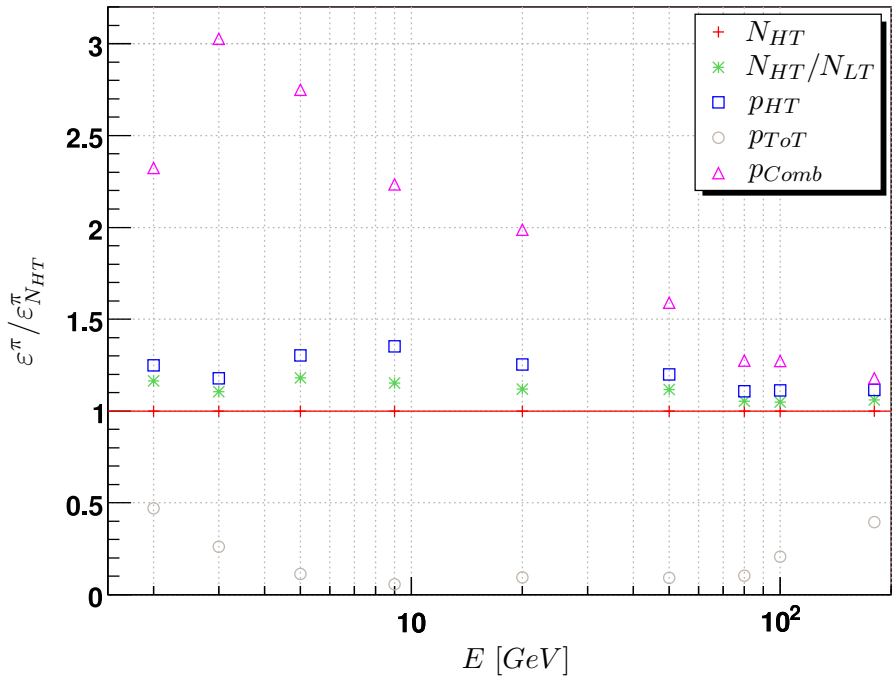

Figure 6.16: π-efficiency at 90% e-efficiency for final methods compared to the N_{HT}-method.

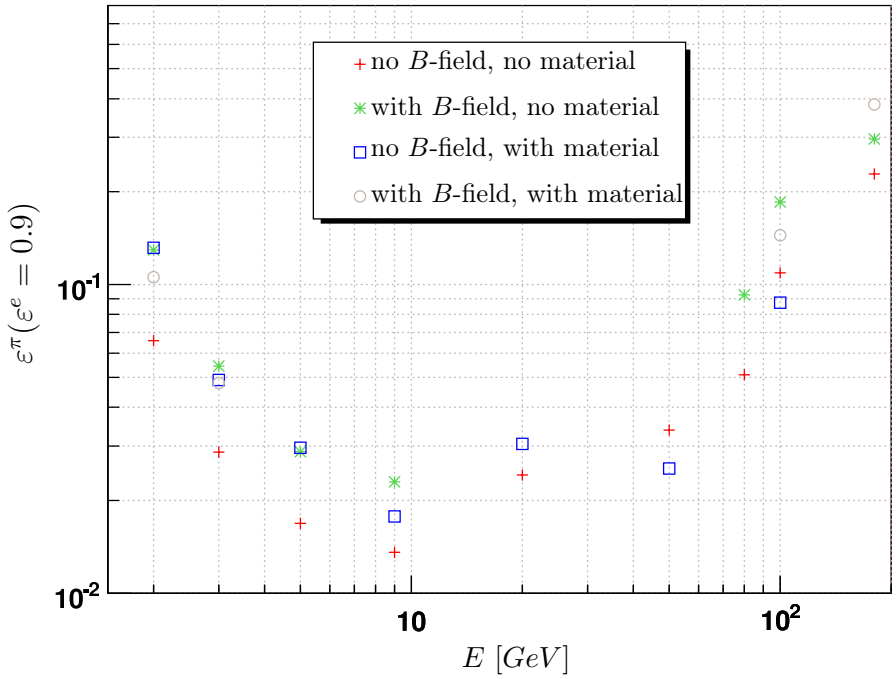

Figure 6.17: ε^{π} at $\varepsilon^{e} = 90\%$ as a function of energy for all configurations of B-field and material.

be seen, the optimal e/π separation for the TRT is in the range from 3 to 30 GeV, with best performance at about 10 GeV. In this region about 97% of the pions are rejected, when retaining 90% of the electrons. Still being significant, the rejection reduces slightly outside this range, due to the onset of TR for pions and electrons (see Section 6.5). The improvements of the different separation methods relative to the current, cutting on the number of HT hits (N_{HT}), as a fuction of energy are shown in Figure 6.16.
These plots show that, by using the simple N_{HT}/N_{LT} method, the e/π separation can be improved by an average factor of 12%. For the HT based likelihood method pion rejection factors of 9 to 40 can be achived, representing an average improvement of about 19% compared to the current method. By including the ToT information in a combined method of both likelihoods, this can be increased up to 300%, especially at low energies, yielding pion rejection factors of up to 70. The separation power reduces at higher energies, due to the rise of the pions' dE/dx curve.
Figure 6.17 finally shows the pion efficiency at 90% electron efficiency of the best method (combined approach) for all setups (with ample statistics) as a function of energy. It can be seen that the general structure is the same for all setups and that, especially at low energies, introducing additional material or switching on the magnetic field reduces the separation slightly. Due to missing input data and/or statistics not all setups are available at all energies.

6.5 Measurement of the Transition Radiation Onset

Using the same data and selection as described in the previous sections as well as additional muon runs at 150, 180 and 350 GeV (see Table 6.1), the TR dependence on the γ factor was measured. Due to the irregular structure of the radiator material in the TRT barrel, reliable calculations of the TR buildup are difficult and need verification/tuning from data. The TRT endcap wheels have regular radiator material, and thus this measurement is unique to the barrel.
The probability for a HT hit was determined (along with its almost negligible statistical error) for each run and particle type (π, e, μ), in case the sample had very high purity, thus omitting samples with low statistics and lack of equivalent "control" samples at the same or nearby energies. An average for each energy was obtained, using the RMS as a measure of the uncertainty due to variations in running conditions. The systematic error from the straw quality requirement is determined by applying two alternative requirements (1: $p^e_{HT,i}$ is significantly (1σ) greater than $p^\pi_{HT,i}$. 2: 35 of the straw in question results in at least 1 σ e/π separation), and the RMS of the variation is considered a systematic error.
At low γ factors (< 500), the HT probabilities are expected to be constant (and low), since these probabilities are the result of noise and fluctuations in the Landau tail of the dE/dx. However, due to the two different geometry configurations at low and high energy (see Section 6.1), the HT probability changes and a correction has to be made.
The correction can be calculated by comparing the average HT probability for pions and muons at low energy (2-9 GeV, 5 values) with that at high energy (20-50 GeV, 3 values), where no change is expected. The averages $\langle p^{\pi+\mu}_{HT}(low\ E)\rangle = 0.0402$ and $\langle p^{\pi+\mu}_{HT}(high\ E)\rangle = 0.0350$ compared to the overall average of $\langle p^{\pi+\mu}_{HT}(all\ E)\rangle = 0.0383$ yields corrections of -0.0020 and 0.0033 at low and high energy, respectively. Half of the correction is used as a systematic error.

Result and Conclusions

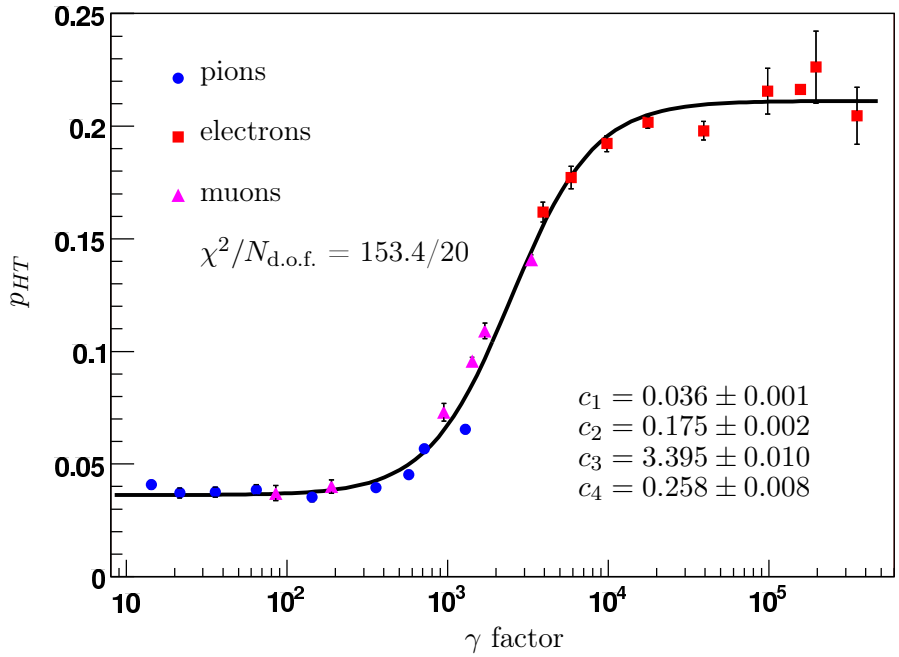

Figure 6.18: HT Probability as a function of γ factor for electrons (red squares), muons (purple triangles) and pions (blue circles) in the energy range 2-350 GeV. The curve is a fit to a turn-on function.

The average values along with their errors, obtained at each energy, were then fitted with a generic turn-on function: $p_{HT}(\gamma) = c_1 + \frac{c_2}{(1.0+\exp(-(\log_{10}\gamma - c_3)/c_4)}$ with $\gamma \in [1, 500000]$. An illustration of this fitted turn-on function, including the data points and the fit parameters, is given in Figure 6.18.

As can be seen in the plot, the data from the three particle types can be well described by the fit, thereby showing that the HT probability only depends on the γ factor and not on the particle type. Due to the fact that not all systematics have been and/or can be determined, larger errors would be expected. In fact, increasing the errors by a factor of 2.5, which seems reasonable, would improve the currently bad χ^2 of the fit.

It can also be seen that in contrast to current simulations, the curve does not saturate until $\gamma \sim 20000$. From this and the fact that the onset starts at $\gamma \sim 1000$ one can see that: 1) low energy electrons have not reached the maximum HT probability and will thus be less separated from pions[7] and 2) even at high energies pions do not emit much TR, and can thus be separated from electrons up to energies of 200-300 GeV.

Finally, and perhaps most importantly, this measurement enables a precise tuning of the TRT simulation. Even though it has to be mentioned that this value can only be tuned for the barrel part, due to theiven data.

[7] Fortunately, it is at these energies that additional separation can be gained from the ToT information (see Section 6.3.2).

Chapter 7

Analysis of the ATLAS W Boson Mass Measurement Potential

This study describes the precision measurement of the W boson mass at ATLAS, putting a special emphasis on the influence of QED radiative corrections. An analysis characterising the systematic error done by considering an incorrect theoretical model for the emission of real photons from the final states, Final State Radiation (FSR), will be presented. The different models are represented by successive theory improvements, or in other words, orders in QED. As an introduction, the general measurement strategy along with a short overview on all considered systematic errors, will be given in Section 7.1. In the following Section 7.2, a more detailed description of QED radiative corrections, in particular FSR, and its modeling utilising the PHOTOS algorithm will be presented, following [Gol06].
In Section 7.4, two studies, giving an estimate for the systematic error, are depicted and the results are summarised in Section 7.5.

7.1 Measurement Strategy

Besides the strategy introduced in Section 3.2 there is another method to measure the W boson mass, utilising the Z boson as a reference. Using this method the measurement gets as independent of the theory and the detector as possible. The properties of the Z boson are well known and measured with high precision and its physics is well understood. Compared to the W boson mass, the Z boson mass is measured with a precision 15 times higher. This is mainly due to large-scale measurements at LEP and the fact, that the leptonic decay of the Z boson leaves a clean signature in the detector and therefore offers a fully definable final state[1]. By not having a missing energy approximation, like in the W boson case, one of the main systematics is left out. In addition, the direct production of Z bosons in a collision of electrons and positrons allowed for a Z boson mass measurement, using a resonance fit. Due to charge conservation this is not possible for the W boson, leaving only the production of W boson pairs as a lower statistics/precision alternative. In more detail, the W boson mass is extracted by the direct comparison of W and Z boson events, introducing a scaling factor between the masses. This is the main difference to the template method, introduced in Section 3.2, where the W boson distributions are fitted to templates instead of weighted Z boson distributions.

[1] The fully definable final state refers only to the charged leptons coming from the Z.

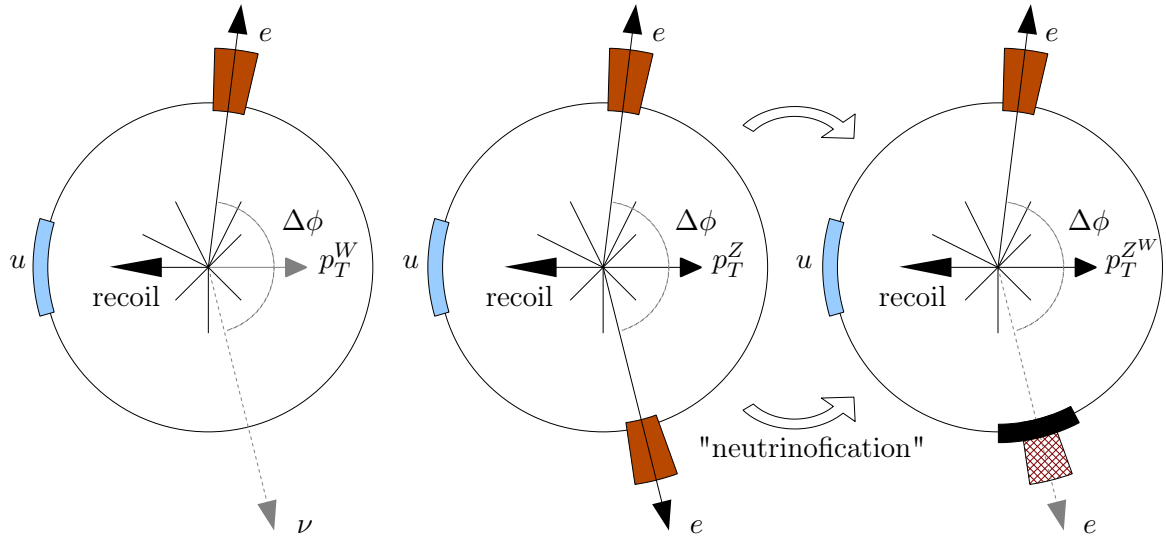

Figure 7.1: Illustration of a $W \to e\nu$ (left) and a $Z \to ee$ (middle) event in the transverse plane. Treating the Z event like a W event (right) is done by a "neutrinofication" of one of the electrons. The detector is *blinded* (black box) against the lepton (in this case electron). While the electrons and the recoil can be measured in the calorimeters (red and blue boxes) the neutrino and the electron after "neutrinofication" (hashed red box) stays undetected, yielding large missing transverse energy $\not\!\!E_T$. The angle between the electron and the neutrino/electron is given by $\Delta\phi$.

Still, since Z boson events are used to tune the simulation of the templates, even the template method utilises the Z boson to some extend.
Since W and Z events are very similar in their theoretical description, in an approximation Z events can be treated as W events. This involves treating one of the charged leptons, coming from the Z boson, like a neutrino and thereby mimic a W boson event. Without going into too much detail, in this procedure, sometimes referred to as "neutrinofication" or lepton removal, the calorimeter response given by the charged lepton is replaced, e.g. by a standard noise signal[2], to blind the detector as illustrated in Figure 7.1. Finally the W boson mass can be extracted by using e.g. the transverse mass distribution of both, the W and the Z boson. When using the neutrinofication it is advantageous to use the transverse mass distribution, in favour of the transverse lepton momentum, to extract the W boson mass, due to the smaller dependence on the transverse momentum of the boson (see Section 3.2) and its higher sensitivity to statistics, though facing the drawback of additional systematic errors from the missing-momentum usage.
By directly fitting[3] the distribution of the W boson to the scaled (by a factor m_W/m_Z) one of the Z boson, the W boson mass is obtained by multiplying the scale factor, that optimises the fit, with the Z boson mass. Due to the scaling with the factor m_W/m_Z this method is referred to as ratio method.
Being less sensitive to uncertainties in the W and Z boson production model, this method has the drawback of a larger statistical error, compared to the template method introduced

[2]This might also be a copy of the signal measured by another ϕ-sector in the same event [Kli06].
[3]A possible method is to derive the Kolmogorov-Smirnov probability for the congruity of two distributions.

in Section 3.2. But due to the enormous statistics of both W and Z boson events at the LHC, this *shortcoming* is expected to be overcome, making this method at least competitive to the conventional one. Another possible approach is to use the difference, of the distributions of the two bosons, instead of the ratio, even though it has the disadvantage of being more sensitive to the lepton energy scale, which cancels to first order in the ratio method.
Apart from all benefits, it is still necessary to characterise the differences in the production of the two bosons and the applied model, to derive a systematic error for the approximation of treating the Z boson like a W boson. The systematic uncertainties are mainly due to differences between the two bosons. While at first order the W and the Z boson are essentially alike, discrepancies show up starting from the second order. Differences appear in the production model, in scale and resolution of the lepton and the recoil, and in the backgrounds.

Source	Effect	Impact on m_T^W	Impact on p_T^l
Production model	W width	1 MeV	1 MeV
	PDFs	. in progress, expected to be 4-8 MeV .	
	FSR, QED	..... see Section 7.5	
	Polarisation	. unknown, but considered very small .	
Lepton reconstruction	EM scale	4 MeV	5 MeV
	EM resolution	3 MeV	5 MeV
	EM linearity	4 MeV	5 MeV
	Lepton efficiency	..... in progress	
Recoil reconstruction	Recoil scale	5 MeV	—
	Recoil resolution	3 MeV	—
	Recoil linearity	in progress	—
	Lepton removal	in progress	—
Backgrounds	$W \to \tau\nu$	.....in progress, but small.....	
	$Z \to l(l)$	.....in progress, but small.....	
	QCD events	.....in progress, but small.....	
Statistics		1.8 MeV	3.2 MeV
Total		<15 MeV !?	< 15 MeV !?

Table 7.1: Table giving an overview on the current status of the systematic uncertainties in the W boson mass measurement at ATLAS. They differ slightly between m_T^W and p_T^l. All numbers are still preliminary.

Systematic effects in the production model include uncertainties coming from the parton distribution functions (PDFs), the transverse boson momentum p_T^W model, the width Γ_W as well as the later discussed QED radiative corrections, mainly FSR. It has been shown that varying the PDF sets causes changes in W boson mass, even though this effect is been reduced by correlations between the two bosons [BBP+07]. The transverse boson momentum p_T^W, so far a theoretical uncertainty, might be modeled, again utilising the Z bosons, and can be included in the mass fit [Pet]. To lowest order p_T^W and p_T^Z are essentially the same. In a first order approximation, where $p_T^W = p_T^Z \cdot \frac{m_W}{m_Z}$, the fit works reasonable well for small transverse boson momenta. Knowing p_T^W to a high precision would allow a W boson mass measurement without any missing energy estimation.
While most of the systematics are reduced with increasing statistics, the PDF and the FSR/QED

uncertainties, being of purely theoretical kind, will not (or just slowly, in case of the PDFs) decrease with increasing statistics. Therefore the importance of these uncertainties is enhanced in future experiments like ATLAS.
The scale and resolution of the transverse lepton momentum p_T^l can be obtained by fitting Z boson events, taking existing correlations into account by concurrent fits of both parameters. Even though this uncertainty has been found to be almost negligible [BB05], the linearity of the scale remains questionable. To obtain the right scale for all momenta, the dependence of the truth scale on the one measured at the Z boson peak needs to be found. This can be achieved, because of the very high statistics, by fitting the Z boson peak in bins of p_T and η. Finally the missing transverse momentum scale, as well as the recoil can also be calibrated by the use of Z boson events. This again expresses the fact that essentially all calibration for a W mass measurement depends on the Z mass.
Recently the CDF collaboration published [CDF07] a new measure for W boson mass, including a characterisation of all systematic uncertainties, but facing the problem of insufficient Z boson statistics (see Sections 3.2 and 3.3). In the analysed 200 pb^{-1} sample they only end up with about 3000 $Z \to ee$ and 5000 $Z \to \mu\mu$ events. The long time between the data taking period and the publication of their measurement also reflects the severity of understanding the detector to this level, which ATLAS will have to face, too.
Table 7.1 shows a summary of the expected contributions to the uncertainty on the W mass measurement at ATLAS. The backgrounds, mentioned in Table 7.1, correspond to about 3-4% in W events and are essentially negligible for Z events (see Section 3.2).

7.2 QED Radiative Corrections and PHOTOS

Radiative corrections described by Quantum Electrodynamics (QED) are, due to their phenomenology, often referred to as bremsstrahlung[4]. While the term bremsstrahlung generally describes the emission of electromagnetic radiation caused by the acceleration of charged particles, QED radiative corrections in particular only include the appearance of electromagnetic radiation in the initial or final state of a high energy interaction. In terms of Feynman diagrams this corresponds to additional photons (QED) or gluons (QCD) on top of the original interaction, resulting in a different initial process described by another diagram. In the case of bremsstrahlung through nuclear interaction, the initial process remains unchanged (same Feynman diagram). Therefore the latter one is in no respect different between W and Z bosons, while QED radiative correction might with increasing order. In fact, if the W boson emits (unmeasured) FSR photons, which the Z boson does not, or vice versa, this will bias the mass measurement. The aim of this analysis is therefore to estimate this bias and the related systematic error.
Additional quanta may appear as virtual particles, creating loops, or as real particles, surviving in the final state. The emission of gluons and photons in the initial state (Initial State Radiation, ISR), the latter one being illustrated in Figure 7.2, is described by readjusting the parton distribution functions (PDFs). The topic of ISR is not within the scope of this thesis and its correct description within the MC generators is assumed. Apart from that it has been shown [BKW98] that the effect of ISR is much smaller than the one expected from

[4] In the following the term bremsstrahlung refers only to the bremsstrahlung-like emission of photons by the final state. It will be mentioned explicitly when referring to bremsstrahlung in terms of the emission of electromagnetic radiation due to nuclear interaction.

FSR. In the following only FSR, mainly the emission of real photons from the final state, will be discussed in more detail. Examples for the leptonic decay of the W boson in terms of

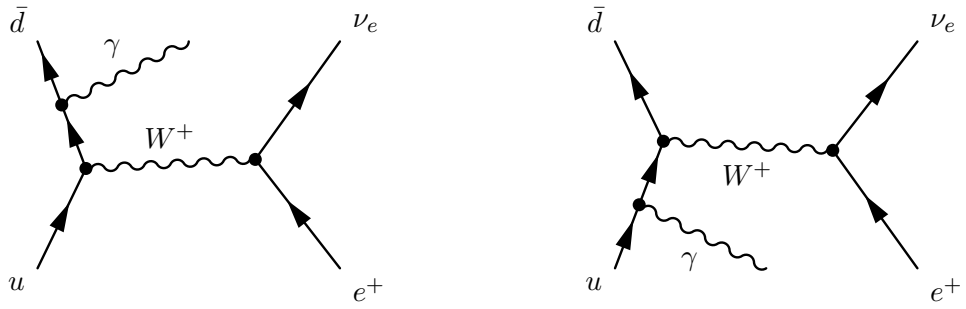

Figure 7.2: Higher order Feynman diagrams for the leptonic decay of the W boson, including the emission of a real photon in the initial state.

Feynman diagrams, including QED radiative corrections in the form of real photons emitted in the final state (Final State radiation, FSR), are illustrated in Figure 7.3.
To a small amount, (QED) radiative corrections affect the calculation of partial widths and cross-sections. The potential effect of FSR as a systematic error in the theoretical predictions in high-precision measurements related to the determination of the W boson mass, will be discussed later in this chapter.
The PHOTOS algorithm, used for this study, is a so-called *afterburner* MC algorithm that adds QED radiative corrections, for particle decays and resonances, to events created by a so-called host generator, e.g. PYTHIA. Therefore the host generator should be set up not to simulate effects related to QED radiative corrections[5]. FSR photons are added in a fraction of events, taking the event topology and momentum conservation into account. For reasons of simplicity QED radiative corrections are usually not considered explicitly, but only calculated for inclusive quantities. This is also due to the non-existence of an analytical, semi-analytical or MC form of exact fixed-order fully-differential formulae, with spin amplitudes or matrix elements squared, for most decay channels. It was shown that carrying out strict, system-

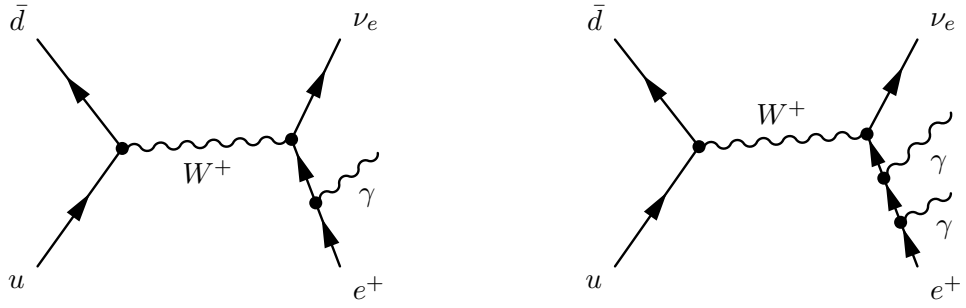

Figure 7.3: Higher order Feynman diagrams for the leptonic decay of the W boson, including the emission of one (left) and two (right) real photons in the final state, corresponding to a first and second order effect, respectively.

atic calculations order-by-order in perturbation theory is in many cases not the most efficient

[5]In PYTHIA this is done by setting the parameter PARJ(90) to a large value, e.g. 20000 (in CSC11) or 99999 (in ATLFAST/PHOTOS). See the PYTHIA manual [SMS06] for details.

way of including the effects of QED radiative corrections. The most widely used technique in QED, to improve the convergence of the perturbative expansion, is called exponentiation. Exponentiation is a well defined way of reshuffling the dominant terms between orders of the expansion. In the so-called leading-log approximation, factorisation properties of QED can be revealed by using partially inclusive formulae. In other words, matrix-element formulae for particle decay along with FSR photons can be factorised into a product of Born-level terms and a bremsstrahlung factor. Using similar techniques, this can be applied to fully differential formulae for Lorentz-invariant phase space for particle decays along with numerous photons. The advantages of this parametrisation, the full phase-space coverage and the exact treatment, are opposed by the drawback of introducing a complicated way of gauge fixing. This complication is due to the fact that each added photon is defined in individual rest frames, separated by boosts. Regardless of these complications, all fully differential cross-section formulae, for any particle-decay process including FSR photons, can be approximated by a product of a cross-section formula, without any QED radiative corrections, and a bremsstrahlung factor. The bremsstrahlung factor itself only depends on the four-momenta of the particles taking part in the interaction, thereby making the approximation *more or less* independent of the underlying process. In the soft-photon region of phase space, this approximation, taking into account both real and virtual corrections, converges to an exact expression.
This convergence is utilised by the PHOTOS algorithm, revealing infrared and collinear singularities. The infrared divergences, introduced by expressions describing the emission of real and virtual photons, are cancelled out order-by-order, by defining a minimum photon energy (technical parameter XPHCUT). An integration over the directions of photons with energies below this cut-off turns the final formula into a infrared-regulator-free form. The fact that only photons with energies above the cut-off are actually created does not cause any harm, due to the finite energy resolution of the experiments. By default the cut-off XPHCUT, giving the energy fraction compared to the charged lepton, is set to 10^{-2} in the fixed order modes (1^{st}, 2^{nd} and 4^{th}) and 10^{-7} in the exponentiated mode[6]. Singularities in the collinear region of the phase space are regulated simply by the masses of the charged particle, taking part in the interaction.

The PHOTOS Algorithm

The PHOTOS algorithm for single photon emission originates from the MUSTRAAL MC algorithm [BKJ82][BKJ83]. This process-dependent algorithm was transformed into a process-independent one, by keeping only the photon emission kernel, but replacing interference terms, in processes where neutral particles decay into two charged particles of the same mass (e.g. $Z \to e^+e^-$), with approximations using a MC interference weight. Double, triple, quartic and exponentiated photon emission can be obtained by subsequent iteration of the bremsstrahlung kernel. In other words, PHOTOS only treats first order to full precision and then iterates on this with fitting weights to get higher orders.
While in the fixed-order modes the maximum number of photons is fixed and the probability for generating or not generating a photon is based on a binomial distribution and calculated in each iteration, in the exponentiated or multiple-photon mode a Poissonian distribution ($P_n = \frac{1}{n!}e^{-p}p^n$) is used to get the actual number of photons to be generated. Therefore the exponentiated mode is not limited to a maximum number of photons. This crude distribution,

[6]The choice of value for the XPHCUT parameter is due the stability of the algorithm. The exponentiated mode is slightly different and more stable, therefore the lower value.

resembling the expansion of an exponent, is also the reason for the name "exponentiated mode".

7.2.1 PHOTOS with ATHENA and ATLFAST

For the purpose of this thesis the PHOTOS MC algorithm was used as an *afterburner* using PYTHIA as the host generator. Event records created with PYTHIA were altered by PHOTOS according to the description above.
Within the ATLAS software environment ATHENA, the PHOTOS algorithm is used in the exponentiated mode, to yield most realistic results. As described in Section 5.8 the events created by PYTHIA and eventually modified by PHOTOS are passed on to the detector description and the reconstruction algorithms.
For reasons of consistency PYTHIA was also chosen as the host generator within the ATLAS fast simulation, ATLFAST. In difference to the full ATLAS software, the ATLFAST/PHOTOS environment allowed for choosing the mode/order PHOTOS is running in. Therefore fast simulation data could be produced for fixed order modes (1^{st}, 2^{nd} and 4^{th}) as well as for the exponentiated mode.
The ATLFAST/PHOTOS environment used for this analysis was initially provided by M. Boonekamp. As a part of the preparation of this study, I compared the output to values given by the PHOTOS authors [GW]. While the ATLFAST/PHOTOS environment was found to give the same results, similar tests of the generator level of the ATLAS software revealed some inconsistencies (see Appendix C.1).

7.3 Data Sets

The data used for this study consists of three different subsets. The first set is part of the computing system commissioning 11 (CSC11) sample, produced with the official data challenge 3 (DC3) joboption files using ATLAS software version 11.0.42. It contains fully simulated and reconstructed events of four different types ($W \to e\nu$, $Z \to ee$, $W \to \mu\nu$ and $Z \to \mu\mu$), generated with PYTHIA along with PHOTOS. The data was given in combined ntuples (CBNTs) with different statistics for all four event types. Table 7.2 states the statistics of this sample after selection, along with the number of identified charged leptons (e/μ) N_{icl}, the total number of FSR photons N_{FSR}, the total number of bremsstrahlung[3] photons N_{Brem}, the number of tracked charged leptons (e/μ) N_{tcl} and the number of charged leptons assigned to a cluster N_{clc}.
The moderate statistics in this sample are due to the very time consuming full simulation process, modelling all physics processes at the interaction point and throughout the whole detector (see Section 5.8.2).
The second subset is created in a fast simulation run using the ATLFAST/PYTHIA/PHOTOS environment and contains an initial number of 100000 events of each type ($W \to e\nu$, $Z \to ee$, $W \to \mu\nu$ and $Z \to \mu\mu$) and order (1^{st}, 2^{nd}, 4^{th} and exponentiated). Table 7.3 gives an overview on the statistics of this sample after event selection. It also shows the number of identified charged leptons (e/μ) N_{icl} and the total number of FSR photons N_{FSR} for each event type and order. By looking at the table, several expectations, such as no FSR photons in the 0^{th} order, more FSR photons emitted by electrons than by muons and clearly more

FSR photons in the exponentiated[7], can already be certified.
The third sample, produced in a private Toy MC based on information obtained from the first two subsets, contains 30 million initial events for each type and order.
For the first two subsets, the criterion for an event to be selected for the analysis was a transverse momentum of the leptons of more than 25 GeV (see Section 3.2). Events of the second and third sample were in addition split into barrel ($\eta < 1.3$) and end-cap ($1.6 < \eta < 2.4$) events, throwing away events within the crack region ($1.3 < \eta < 1.6$). The reason to exclude events from the crack region and at high η, is mainly due to detection inefficiencies.

Counter ↓ | Event type →	$W \to e\nu$	$Z \to ee$	$W \to \mu\nu$	$Z \to \mu\mu$
N_{ini}	17000	283300	19400	31200
N_{sel}	10062	175102	11340	19729
fraction of selected events	0.592	0.618	0.585	0.632
N_{icl}	10062	350204	11340	39458
N_{FSR}	727	28327	349	1732
ave. number of FSR photons per charged lepton	0.072	0.081	0.031	0.044
N_{Brem}	6195	212190	0	0
ave. number of Brem photons per charged lepton	0.616	0.606	-	-
N_{tcl}	9182	278764	10348	31642
N_{clc}	9157	277753	161	648

Table 7.2: Table showing the statistics of the fully reconstructed data set, taken from the CSC11 sample. Given are the number of initial events N_{ini}, the number of selected events N_{sel} (after cuts), the number of identified charged leptons (e/μ) N_{icl}, the total number of FSR photons N_{FSR}, the total number of bremsstrahlung[3] photons N_{Brem}, the number of tracked charged leptons (e/μ) N_{tcl} and the number of charged leptons assigned to a cluster N_{clc}[4].

7.4 Influence of Final State Radiation

The emission of real photons from the final state, in particular the electrons and muons in case of the observed leptonic decays of the W and Z boson, causes a drop in the energy of the leptons. This effect is illustrated for $W \to e\nu$ events in Figure 7.4, showing the distributions of the transverse lepton momentum p_T^l (left) and the transverse and invariant mass of the W boson, m_T^W (middle) and m_W (right), respectively. All plots show the values without (no index) and with FSR taken into account (index FSR or added). A decrease of the values due to the emission of FSR photons, can be observed in all three plots.
Figure 7.5 illustrates general properties of the FSR photons, like the fraction of events with a certain number of FSR photons N_{FSR}, the transverse momentum p_T^{FSR} and the direction relative to the emitting lepton ΔR. The properties are given for all considered orders in QED (0^{th}, 1^{st}, 2^{nd}, 4^{th} and exponentiated), represented by the different colours.
The aim of this analysis is to give a value for the systematic uncertainty in the W boson mass measurement, done by considering the wrong theoretical production model for FSR photons

[7]The increased number ob FSR photons in the exponentiated mode is due to the lower energy cut (XPHCUT), compared to the fixed-order modes.
[3]Here the term bremsstrahlung refers to the emission of electromagnetic radiation due to material effects.
[4]The clusters assigned to muons might be assigned due to signals from FSR photons.

Order	Event type → / Counter ↓	$W \to e\nu$	$Z \to ee$	$W \to \mu\nu$	$Z \to \mu\mu$
0^{th}	N_{sel}	60119	59231	60119	59231
	fraction of selected events	0.601	0.592	0.601	0.592
	N_{icl}	60119	118462	60119	118462
	N_{FSR}	0	0	0	0
	ave. number of FSR photons per charged lepton	-	-	-	-
1^{st}	N_{sel}	57614	54788	58899	56914
	fraction of selected events	0.576	0.548	0.589	0.569
	N_{icl}	57614	109576	58899	113828
	N_{FSR}	9287	20158	4661	10797
	ave. number of FSR photons per charged lepton	0.161	0.184	0.079	0.095
2^{nd}	N_{sel}	57698	54975	58934	57022
	fraction of selected events	0.577	0.550	0.589	0.570
	N_{icl}	57698	109950	58934	114044
	N_{FSR}	8565	18580	4589	10392
	ave. number of FSR photons per charged lepton	0.148	0.169	0.078	0.091
4^{th}	N_{sel}	57559	54891	58887	56925
	fraction of selected events	0.576	0.549	0.589	0.569
	N_{icl}	57559	109782	58887	113850
	N_{FSR}	8638	18342	4593	10290
	ave. number of FSR photons per charged lepton	0.150	0.167	0.078	0.090
exp	N_{sel}	57583	54948	58923	57062
		0.576	0.549	0.589	0.570
	N_{icl}	57583	109896	58923	114124
	N_{FSR}	42429	85995	22547	48349
	ave. number of FSR photons per charged lepton	0.737	0.783	0.383	0.424

Table 7.3: Table showing the statistics of the fast simulated data set containing 100000 initial events for each type ($W \to e\nu$, $Z \to ee$, $W \to \mu\nu$ and $Z \to \mu\mu$) and order (1^{st}, 2^{nd}, 4^{th} and exponentiated). Given are the number of selected events N_{sel} (after cuts), the number of identified charged leptons (e/μ) N_{icl} and the total number of FSR photons N_{FSR}.

(see Section 7.1). The uncertainty is obtained by measuring the stability of the effect, caused by FSR, against successive theory improvements. The PHOTOS algorithm, used to model the FSR effects (see previous sections), allows for fixed-order as well as exponentiated mode calculations, which represent the successive improvements of the theory.
To quantify the effect of FSR, the transverse lepton momentum p_T^l was chosen as the observable, since it is used directly and indirectly to measure the W boson mass (see Sections 3.2). The analysis is split into two substudies, with one being based on generator-level data only, whereas the other one includes detector information, based on the fully simulated and reconstructed data, mentioned above. Both analyses will be presented in the subsequent sections.

7.4.1 Influence at Generator Level

Due to the short production time, compared to full simulation, the data sample produced for this subanalysis, using the ATLFAST/PYTHIA/PHOTOS environment, contains data for four different fixed-order calculations and the exponentiated mode of PHOTOS (see Table 7.3). Therefore the influence of FSR could be modelled in five different modes, representing a

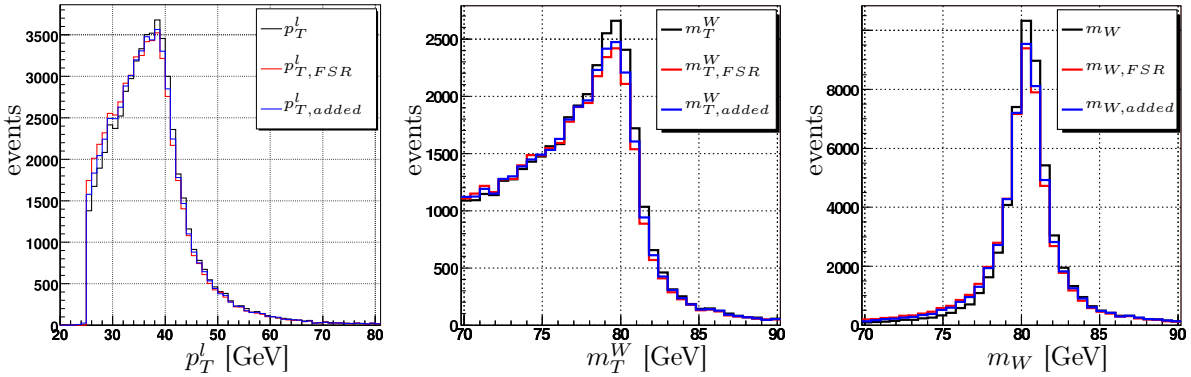

Figure 7.4: Figure showing the transverse momentum of the lepton (left), the transverse mass (middle) and the invariant mass (right), before (X) and after (X_{FSR}) FSR effects were added, for $W \to e\nu$ events. The value for the electron-like treatment (X_{added}, see next section), readding the energy of collinear photons, is also given in the plots (see Section 7.4.1).

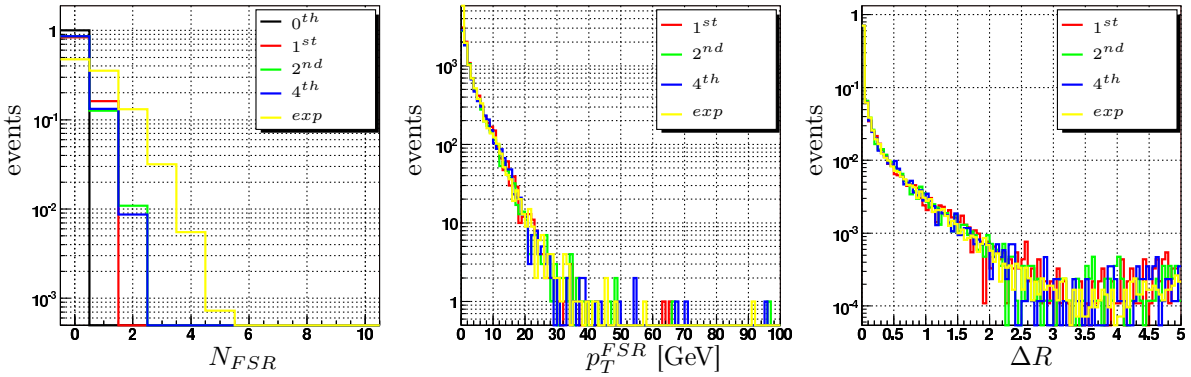

Figure 7.5: Figure showing the distributions of the number of FSR photons N_{FSR} emitted in an events, the transverse momentum p_T^{FSR} and the direction relative to the emitting lepton ΔR, for all orders (1^{st}, 2^{nd}, 4^{th} and exponentiated).

successive improvement of the theory, whereas the exponentiated mode should reflect reality the best. Still the study faces the drawback of not taking into account any possible detector effects.

In the event record, the transverse momentum of the particles involved in the interaction is stored before (p_T) and after ($p_{T,FSR}$) the PHOTOS MC algorithm eventually added FSR photons. An additional variable ($p_{T,added}$) represents the value obtained by re-summing the energy of the charged lepton with the energy of its FSR photons, emitted within a cone of $\Delta R = \sqrt{\Delta\phi^2 + \Delta\eta^2} < 0.07$ (corresponding to about 4°) around it (see Figure 7.5 (right)). This describes the fact that photons emitted (almost) collinear to the lepton will end up in the same cluster in the calorimeter and therefore not result in any energy difference. This so-called electron-like treatment, of course, only works for electrons, since muons are neither stopped nor

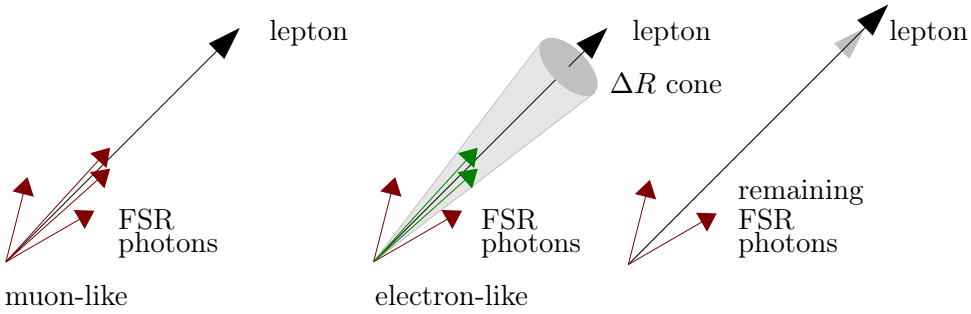

Figure 7.6: Muon-like (left) and electron-like (right) treatment. In the latter case the FSR photons falling into the ΔR cone, are re-added to the charged lepton (green, middle) and only the remaining ones are considered as FSR photons further on (right).

measured by the calorimeters[8]. Hence for muons, the so-called muon-like treatment ($p_{T,FSR}$) is used. An illustration of these treatments is given in Figure 7.6.

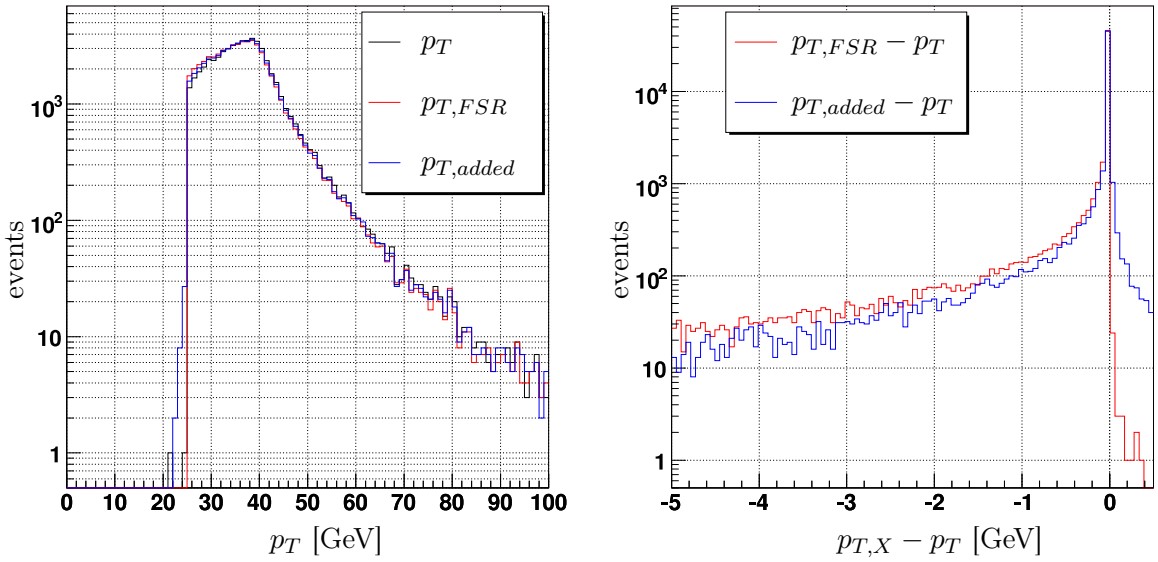

Figure 7.7: Figure showing the distributions of: p_T, $p_{T,FSR}$ and $p_{T,added}$ in exponentiated mode (left) and the residuals $p_{T,FSR} - p_T$ and $p_{T,added} - p_T$ (right) for $W \to e\nu$ events.

Taking the residual (e.g. $p_{T,added} - p_T$) of the electron/muon-like treated and the original value, one can determine the effect of FSR, by measuring the mean of these distributions. In Table 7.4 these mean residuals are given for all orders and event types. The residuals are zero at 0^{th} order (per definition) and stay pretty constant afterwards. An example, of the p_T distribution of $W \to e\nu$ exponentiated mode events, before and after FSR photons were added

[8]Muons leave a fraction of their energy in the calorimeters, but its hard to distinguish from noise and has to be taken into account in the reconstruction. It is considered negligible for the purpose of this work.

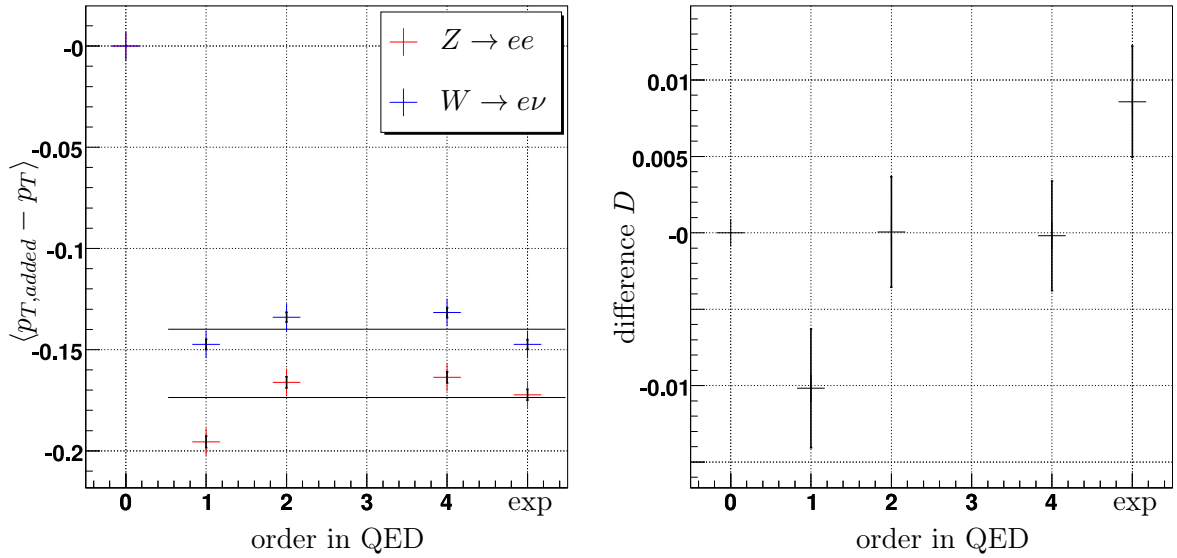

Figure 7.8: Figure showing the mean value of the $p_{T,added} - p_T$-distribution for $Z \to ee$ and $W \to e\nu$ events (left) and the differences (right), calculated using Equation 7.1, as a function of the order in QED. The points in the left plot correspond to the coloured (blue and red) values in Table 7.4. The fitted values correspond to the coloured (blue and red) values in Table 7.5.

(both electron and muon-like), is given in Figure 7.7 (left). The distributions of the residuals are shown in Figure 7.7 (right).
The next step of the analysis is to investigate how much the average transverse momentum is changed with increasing order in QED, reflecting an improvement of the theoretical model. Since only the difference between W and Z bosons is of interest, the two are subtracted the following way:

$$D(order) = X(Z, order) \cdot w - X(W, order) \tag{7.1}$$

The factor w, weighting Z relative to W boson events, is obtained by calculating the ratio of Z and W bosons, for the average effect over all orders containing FSR (1^{st}, 2^{nd}, 4^{th} and exponentiated). The four values are fitted with a constant, for both Z (c_Z) and W (c_W) bosons, and the weight for Z events w is obtained using $w = \frac{c_W}{c_Z}$. Exemplary this is shown in Figure 7.8 (left) for the electron-like treated $p_{T,added} - p_T$ residuals.
The RMS of the values used in the fits, along with the difference for both treatments and lepton types, are given in Table 7.5. Figure 7.8 (right) shows the weighted differences between the Z and the W boson values ($\langle p_{T,added} - p_T \rangle$), as a function of the PHOTOS modes (orders in QED).
The RMS of these values for different orders, characterising the stability, yields the final systematic in the measurement, given (underlined) in Table 7.5. The mean is per definition expected to be zero. For electrons (electron-like treatment), the uncertainty on the transverse momentum is 3.8 MeV, while for muons (muon-like treatment) the value turns out to be 2.4 MeV.
At leading order (see Equation 3.6), the effect on the W mass will be about twice the effect

on the transverse momentum, yielding 7.6 MeV for electrons and 4.8 MeV for muons. Due to the fact that no detector effects have been taken into account in this approach, these values represent the minimal uncertainties.

	$W \to e\nu$		$Z \to ee$	
Order	$p^l_{T,FSR}$	$p^l_{T,added}$		
0^{th}	0.000	0.000	0.000	0.000
1^{st}	-0.215	-0.147	-0.269	-0.196
2^{nd}	-0.191	-0.134	-0.221	-0.166
4^{th}	-0.190	-0.132	-0.218	-0.164
exp	-0.213	-0.147	-0.234	-0.172
	$W \to \mu\nu$		$Z \to \mu\mu$	
Order	$p^l_{T,FSR}$	$p^l_{T,added}$		
0^{th}	0.000	0.000	0.000	0.000
1^{st}	-0.104	-0.083	-0.144	-0.119
2^{nd}	-0.100	-0.080	-0.129	-0.111
4^{th}	-0.101	-0.080	-0.126	-0.106
exp	-0.107	-0.084	-0.136	-0.114

Table 7.4: Table showing the residuals (in GeV) of the transverse momentum of the lepton(s) p^l_T before and after FSR effects were added. The residuals are given for the electron-like treatment (X_{added}) and the muon-like treatment (X_{FSR}). The 0^{th} order QED description does not allow any FSR, therefore the residual yields zero.

		W	Z	difference D	
	property	mean	mean	mean [GeV]	RMS [GeV]
e	$p^l_{T,FSR}$	-0.202	-0.235	-0.00086	0.00586
	$p^l_{T,added}$	-0.140	-0.174	-0.00044	0.00383
μ	$p^l_{T,FSR}$	-0.103	-0.134	-0.00026	0.00239
	$p^l_{T,added}$	-0.081	-0.112	-0.00014	0.00151

Table 7.5: For both leptons (e, μ), this table shows the RMS of the values (1^{st}, 2^{nd}, 4^{th} and exponentiated) for both boson types (W, Z), along with the mean and its RMS for the difference, calculated using 7.1 and based on the residuals given in Table 7.4.

7.4.2 Influence at Detector Level

Full simulation, i.e. the full description of the physics effects in the detector, was only available for the exponentiated mode (standard mode for the full simulation chain). To still be able to compare the effect of the emission of real FSR photons at different orders of QED, this approach uses information from both, the fully simulated and the ATLFAST sample (see above).
The fully simulated data sample is used to extract the effect of a certain number of FSR photons emitted by a charged lepton on its transverse momentum. The effect is characterised by

Number of Photons $N_{FSR} \rightarrow$		0	1	2	3	$\geq$4
Detector Part $\downarrow$	Event Type $\downarrow$	$< R >$	$< R >$	$< R >$	$< R >$	$< R >$
barrel	$W \rightarrow e\nu$	-2.471	-6.935	-5.322	0.000	0.000
	$Z \rightarrow ee$	-2.603	-7.006	-9.335	-10.621	0.000
	$W \rightarrow \mu\nu$	-0.053	-5.109	-7.896	0.000	0.000
	$Z \rightarrow \mu\mu$	-0.110	-5.142	-5.896	0.000	0.000
endcap	$W \rightarrow e\nu$	-5.253	-8.201	-13.076	0.000	0.000
	$Z \rightarrow ee$	-5.390	-7.868	-9.562	-10.376	0.000
	$W \rightarrow \mu\nu$	-0.189	-4.646	-8.260	0.000	0.000
	$Z \rightarrow \mu\mu$	-0.310	-4.771	-8.299	0.000	0.000

Table 7.6: The residuals (R in GeV) of the transverse momentum before and after FSR photons were added, for all combinations of lepton and boson types, and numbers of FSR photons from zero to four or more (0,1,2,3,$\geq$4).

measurering the residual $p_{T,FSR} - p_T$ (R) between the transverse momentum before and after FSR photons were added. This is done for leptons measured in the barrel and in the end-cap separately, due to e.g. different detection efficiencies. The transverse momentum measurement is based on the track information stored in the data set. The residuals are measured for all combinations of lepton and boson types, and numbers of FSR photons from zero to four or more (0,1,2,3,$\geq$4), as shown in Table 7.6. The change in the transverse momentum is thereby expected to be proportional to the number of emitted FSR photons. Realistic distributions for the initial transverse momentum p_T, as well as η and ϕ, are also obtained from the full simulation sample.

The information extracted from the ATLFAST sample, contains the fractions of events with a certain number of FSR photons, for each event type and order in QED (0^{th}, 1^{st}, 2^{nd}, 4^{th} and exponentiated). These fractions are given in Table C.1.

In a Toy-MC, these two inputs are combined in a production of 30 million events for each type and order. Thereby the number of FSR photons to be *added* to each event is based on the information from the ATLFAST sample, whereas the change in the transverse momentum, according to this number, is based on the information from the fully simulated data set.

Following the same procedure as introduced in the previous section, one gets the mean residuals $\langle p_{T,FSR} - p_T \rangle$ as shown in Table 7.7 (following Table 7.4). Finally calculating the difference D one gets the results given in Table 7.8 (following Table 7.5).

It has to be mentioned that the result for electrons is only shown for reasons of completeness and does not reflect any reasonable estimation of the error. This is due to the fact that the emission of nuclear interaction bremsstrahlung photons throughout the detector, causes effects on the transverse momentum of the electron, similar to those of FSR photons. Due to the larger number of material caused bremsstrahlung photons compared to FSR photons, the effect of the latter ones is essentially smeared out, causing the large value. This superimposing of the FSR effects is also the reason for not considering the electron-like treatment (see previous section) in this substudy. A systematic uncertainty arising from nuclear interaction bremsstrahlung and therefore the material in the detector, is taken into account in the lepton reconstruction (see Table 7.1).

For muons (muon-like treatment), not suffering nuclear interaction bremsstrahlung effects, the

final systematic obtained in the detector level study turns out to be 7.2 MeV. At leading order (see Equation 3.6), the effect on the W mass will be about twice the effect on the transverse momentum, yielding 14.4 MeV.

Order	$W \to e\nu$	$Z \to ee$	$W \to \mu\nu$	$Z \to \mu\mu$
0^{th}	-2.474	-2.603	-0.084	-0.155
1^{st}	-2.597	-2.604	-0.086	-0.231
2^{nd}	-2.570	-2.604	-0.093	-0.228
4^{th}	-2.574	-2.604	-0.092	-0.227
exp	-2.904	-2.604	-0.247	-0.580

Table 7.7: Table showing the average residuals $p_{T,FSR} - p_T$ (in GeV) of the transverse momentum of the lepton(s) before (p_T) and after ($p_{T,FSR}$) FSR effects were added.

		W	Z	difference D	
	property	mean	mean	mean [GeV]	RMS [GeV]
e	$p^l_{T,FSR}$	-2.661	-2.604	0.06064	0.08092
μ	$p^l_{T,FSR}$	-0.129	-0.316	0.01354	0.00715

Table 7.8: For both leptons (e, μ), this table shows the RMS of the values (1^{st}, 2^{nd}, 4^{th} and exponentiated) for both boson types (W, Z), along with the mean and its RMS for the difference, calculated using 7.1 and based on the residuals given in Table 7.6. All values are given in GeV.

7.5 Results

In the generator level study it could be shown that the uncertainty due to FSR is of the order of 7.6 MeV for electrons and 4.8 MeV for muons. Note that in the derivation of these numbers no detector effects were taken into account, and therefore the values represent the minimal uncertainties, characterising pure FSR effects. Though, including the rough first order in the calculation and having the exponentiated mode behave slightly different, due to the different cut-off, this might be a conservative estimation. Therefore the errors might actually be slightly smaller. Still this sets a first level of the errors, which are expected to increase when considering detector effects.
Including detector effects, causes the FSR effects to be superimposed by similar effects, due to nuclear interaction bremsstrahlung, and therefore get *lost* in case of the electrons. On the other hand, muon events, hardly including any nuclear interaction bremsstrahlung, yield a value of about 14.4 MeV. This value still contains additional uncertainties, due to detector effects, and is therefore expected to be larger than the "true" uncertainty, due solely to FSR. Additional detector effects smear out the transverse momentum measurement and increase the spread of the residuals, thereby also increasing the spread/RMS of the total residuals at different orders.
To summarise, the systematic error due to considering the wrong theoretical model for FSR,

should be estimated based on the generator study, to about 8 MeV (5 MeV) for electrons (muons). The values from the generator study were considered more trustworthy, due to the fact that the weakest point in the analysis probably is the connection between the fully simulated and the fast simulation data in the detector study. In addition their conservative estimation compensates (at least partially) a possible increase due to the introduction of detector effects.

Chapter 8

Conclusion and Outlook

In the first study, describing the mapping and optimisation of the particle identification in the TRT, new methods, using additional, previously unused information have been introduced and validated. Using the time-over-threshold, and therefore dE/dx information as a separate method as well as a supplementation to the current method (counting high-threshold hits on track) led to improvements, especially in the low energy region (3 to 30 GeV). By introducing a likelyhood method for both the high-threshold and the low-threshold variables, the electron-pion separation could be improved by up to 300%. This increment mainly at low energies is of special interest for the tagging/identification of b-quarks and essential for the Higgs boson searches in these channels. Even though this maximal improvement is obtained only in the low energy region, there is still a significant gain at all energies examined in this study. This can be of importance for e.g. the identification of electrons in W boson decays.
By measurering the transition radiation onset, it could be shown that current MC does not match the data. Hence the measured onset-curve can be used for a precise tuning of the TRT simulation.
Due to errors in the reconstruction code, used for this study, the reconstruction efficiencies for magnetic-field runs were very low, yielding less reliable results for those setups. In a next iteration of this analysis, beyond the scope of this thesis, a new, corrected version of the ATLAS software is to be used. First checks with ATLAS software release 12.0.4 have shown improved results.
Another limitation of this study, due to missing data, is the parametrisation of the high-threshold hit probability. Having only two different beam line positions in the testbeam setup, did not allow for a precise study on the effect of material (dividing walls) on the TR build-up. By having a selection of different points and/or angles of incident, a possible parametrisation could have been investigated to much greater detail.
A second iteration of this analysis, planed for the near future, will also include the production of MC data sets corresponding to the real data, allowing for a cross-check of the methods and more important, a tuning of the TRT simulation algorithm.
This next iteration step will also include the converse approach of an electron rejection, since this is of importance to the reconstruction of taus, yielding a single charged pion in its decay. Thus its also of relevance to the Higgs search, due to the fact that the $h \to \tau\tau$-channel is right now the most promising one.
Still this analysis will be limited to the barrel part of the TRT and does not allow exact conclusion for the end-cap parts. Even within the barrel part, the given setup did not allow

for studies on the η-dependence.
Also planed for the near future and essential for the future usage of the methods, introduced in this study, is the implementation of required data bases and algorithms into the ATLAS reconstruction and analysis software framework.

The second analysis described the ATLAS potential for measuring the W boson mass, putting special emphasis on the systematic error done by considering the wrong theoretical model for QED radiative corrections. Of particular interest was the emission of real photons from the final state (Final State Radiation, FSR) in the leptonic decays, since it has the mayor impact. It could be shown that the uncertainty, due to this systematic effect introduced to the W boson mass measurement, is about 8 MeV (5 MeV) for electrons (muons), while the current estimate for the mass itself is (80.398±0.025) GeV [CDF07]. The estimated error is within the expected range of up to 10 MeV and does not interfere with the aimed total uncertainty on the W boson mass of less than 15 MeV (see Table 7.1).
If in a next step the total uncertainty on the W boson mass should be pushed below 10 MeV, this effect has to be investigated in fine detail, as the Higgs mass prediction, and thus the capability to reject the SM against e.g. a possible MSSM, crucially depends on these details. Still this study gives a first estimate, which could be improved by e.g. producing fully simulated and reconstructed data for all orders in QED. The estimate including the detector effects, could only be obtained in a roughly, utilising both fully simulated/reconstructed data and fast simulation data, because of the lack of this detailed data.
A general increment of the statistics might also allow to gain more information about the influence in the electron channels, which, in this analysis, was not possible, due to the superimposing nuclear interaction bremsstrahlung.
During the analysis, it has also been found that further checks of the ATLAS software environment, with special focus on the modelling of radiative corrections, have to be carried out.

Acknowledgements

Hopefully you are not just browsing through this chapter to look for your name or any credits you might have got. Because there is a lot more to look at in this thesis. A thesis that would not have been possible without the help of a number of people.

First of all, I wish to thank my supervisor Troels C. Petersen, basically for everything he did for me throughout the last two years. Heaps of things made you the main reason for my decision to write my thesis in Copenhagen. To summarise, I would like to quote something I also got from you, to be more specific, from your master thesis:

"It has been both a pleasure and an honour for me to be your student."

Secondly, I wish to thank my better half Heike, for her love and endless support and patience over the past years. What should I write more... "I just love you!"

I also wish to thank my family. My parents sepcially for making it at all possible for me to stay in Denmark and my sister for all the scientific advices. Thank you all for your support throughout the year.

Of course, I would also like to thank all the people from the HEP group for their criticism, their interesting and inspiring discussions and their support. Especially I would like to thank my second supervisor Jørgen B. Hansen, my advisor John R. Hansen and Chafik Driouichi (Thanks for all the Ntuples). It has been a pleasure working with all people in the HEP group. Thank you for the warm welcome, the possibilities you offered and the trust you had in me. These things have been major reasons for me to choose the field of High Energy Physics.

And last but not least, thanks to all my friends for their questions, criticism, ideas, jokes, support or just spending a relaxing evening with me... specially Gareth and Esben for proof-reading and/or being roomies.

And for those who understand...
PARTY PEOPLE JUNGLE BOOGIE
May the BOOGIE be with you!

Bibliography

[A+98] B. Abbott et al., *Measurement of the W boson mass*, Phys. Rev. D **58**(9), 092003 (Sep 1998). 3.2

[ATLa] ATLAS, *ATLAS Public Homepage*, The ATLAS Collaboration , http://www.atlas.ch. 4.1, 5.3

[ATLb] ATLFAST, *Atlas Fast Simulation Homepage*, http://www.hep.ucl.ac.uk/atlas/atlfast/. 5.8.4

[BB05] N. Besson and M. Boonekamp, *Determination of the Absolute Lepton Scale Using Z Boson DecaysApplication to the Measurement of MW*, (Nov 2005). 7.1

[BBP+07] M. Boonekamp, N. Besson, T. Petersen, E. Klinkby and S. Mehlhase, *Re-evaluation of the ATLAS potential for measuring m_W*, in preparation (2007). 7.1

[BKJ82] F. A. Berends, R. Kleiss and S. Jadach, *RADIATIVE CORRECTIONS TO MUON PAIR AND QUARK PAIR PRODUCTION IN ELECTRON - POSITRON COLLISIONS IN THE Z(0) REGION*, Nucl. Phys. **B202**, 63 (1982). 7.2

[BKJ83] F. A. Berends, R. Kleiss and S. Jadach, *MONTE CARLO SIMULATION OF RADIATIVE CORRECTIONS TO THE PROCESSES E+ E- → MU+ MU- AND E+ E- → ANTI-Q Q IN THE Z0 REGION*, Comput. Phys. Commun. **29**, 185–200 (1983). 7.2

[BKW98] U. Baur, S. Keller and D. Wackeroth, *Electroweak radiative corrections to W boson production in hadronic collisions*, Phys. Rev. D **59**(1), 013002 (Nov 1998). 7.2

[BMP83] V. Barger, A. D. Martin and R. J. N. Phillips, *Perpendicularev mass fromW decay*, Zeitschrift fÃ¼r Physik C Particles and Fields **21**, 99–101 (Mar 1983). 3.2

[Boo] M. Boonekamp, private communication with Maarten Boonekamp. C.1

[BW36] G. Breit and E. Wigner, *Capture of Slow Neutrons*, Phys. Rev. **49**(7), 519–531 (Apr 1936). 3.1

[Cab63] N. Cabibbo, *Unitary Symmetry and Leptonic Decays*, Phys. Rev. Lett. **10**(12), 531–533 (Jun 1963). 7

[CDF07] A. Kotwal (CDF Collaboration), *The First Run II Measurement of the W Boson Mass by CDF*, Joint Theoretical-Experimental Physics Seminar (Jan 2007). 2.29, 7.1, 8

[CKM+01] G. Corcella, I. G. Knowles, G. Marchesini, S. Moretti, K. Odagiri, P. Richardson, M. H. Seymour and B. R. Webber, *HERWIG 6.5: an event generator for Hadron Emission Reactions With Interfering Gluons (including supersymmetric processes)*, JHEP **0101**, 010 (2001). 5.8.1

[CS77] J. C. Collins and D. E. Soper, *Angular distribution of dileptons in high-energy hadron collisions*, Phys. Rev. D **16**(7), 2219–2225 (Oct 1977). 3.1

[CTEQ] C. Collaboration, *CTEQ - The Coordinated Theoretical-Experimental Project on QCD - Webpage*, http://www.phys.psu.edu/ cteq/. 3

[DGGK05] B. Di Girolamo, M. Gallas and T. Koffas, *ATLAS Barrel Combined Run in 2004 - Test Beam Setup and its evolutions*, EDMS Note **ATC-TT-IN-0001 406980** (2005). 6.1, 6.1

[Dri] C. Driouichi, private communication with Chafik Driouichi. 6.2

[DY70] S. D. Drell and T.-M. Yan, *Massive Lepton-Pair Production in Hadron-Hadron Collisions at High Energies*, Phys. Rev. Lett. **25**(5), 316–320 (Aug 1970). 3

[DY71] S. D. Drell and T.-M. Yan, *Partons and their applications at high energies*, Annals of Physics **66**(2), 578–623 (Aug 1971). 3

[F+98] Y. Fukuda et al., *Evidence for Oscillation of Atmospheric Neutrinos*, Phys. Rev. Lett. **81**(8), 1562–1567 (Aug 1998). 5

[FGM58] R. Feynman and M. Gell-Mann, Phys. Rev. **109**, 193–198 (1958). 2.1.1

[G+58] M. Goldhaber et al., Phys. Rev. **109**, 1015–1017 (1958). 2.1.1

[GEANT93] GEANT (Application Software Group, Computing and Networks Division Collaborations Collaborations), *GEANT - Detector Description and Simulation Tool*, CERN, 1993. 5.8.2

[Gla61] S. Glashow, Nuclear Physics **22**, 579–588 (1961). 2.1.2, 2.2

[Gol61] J. Goldstone, Nuovo Cimento **19**, 154 (1961). 2.2.1

[Gol06] P. Golonka, *Computer simulations in high energy physics: a case for PHOTOS, MC-TESTER, TAUOLA and at2sim*, PhD thesis, Polish Academy of Science, Krakow, 2006. 7

[GSW62] J. Goldstone, A. Salam and S. Weinberg, *Broken Symmetries*, Phys. Rev. **127**(3), 965–970 (Aug 1962). 2.2.1

[GW] P. Golonka and Z. Was, *PHOTOS tests*, http://piters.web.cern.ch/piters/MC/PHOTOS-MCTESTER/Results/results-heavy.html. 7.2.1, C.1

[GW06] P. Golonka and Z. Was, *PHOTOS Monte Carlo: a precision tool for QED correctionsin Z and W decays*, Eur. Phys. J. C **45**(1), 97–107 (Jan 2006), http://www.springerlink.com/content/f5438774n0m44l17. 5.8.1

[H+73a] F. Hasert et al., Phys. Lett. **46B 121** (1973). 2.1.1

[H+73b] F. Hasert et al., Phys. Lett. **46B 138** (1973). 2.1.1

[Hig66] P. W. Higgs, *Spontaneous Symmetry Breakdown without Massless Bosons*, Phys. Rev. **145**(4), 1156–1163 (May 1966). 2.2.1

[HM84] F. Halzen and A. Martin, *Quarks & Leptons: An Introduction Course in Modern Particle Physics*, John Wiley and Sons, Inc, 1984. 2.3, 2.2.1

[InD] InDetTBRecExample, Changelog of the InDetTBRecExample package, version 00-02-75. 6.2

[Kli06] E. Klinkby, *Systematic effects on the W mass measurements due to calibration and resolution of EtMiss*, ATLAS SM meeting 6. September (2006). 2

[KLLW81] J. E. Kim, P. Langacker, M. Levine and H. H. Williams, *A theoretical and experimental review of the weak neutral current: a determination of its structure and limits on deviations from the minimal $SU(2)_L \times U(1)$ electroweak theory*, Rev. Mod. Phys. **53**(2), 211–252 (Apr 1981). 10

[LE] LEP-EWWG, *The LEP Electroweak Working Group Homepage*, The LEP Electroweak Working Group , http://lepewwg.web.cern.ch/LEPEWWG/. 2.3, 2.2.3

[lep03] *Searches for the Standard Model Higgs Boson at LEP*, in preparation, to be submitted to Phys. Lett. B. (2003). 2

[LRY49] T. D. Lee, M. Rosenbluth and C. N. Yang, Phys. Rev. **75**, 905 (1949). 2.1.2

[LY56] T. D. Lee and C. N. Yang, Phys. Rev. **104**, 254–258 (1956). 2.1.1

[Mir92] E. Mirkes, *Angular decay distribution of leptons from W-boson at NLO in hadronic collisions*, Nucl. Phys. B **387**, 3–85 (1992). 3.1

[MP] S. Mehlhase and T. Petersen, *Particle Identification with the TRT - Webpage*, http://hep.nbi.dk/atlas/trt-pid.php. 6.2.2, 6.3

[MP06] S. Mehlhase and T. Petersen, *A probability based approach to PID in the TRT detector of ATLAS*, (2006). 6.2.2

[MRST00] A. D. Martin, R. G. Roberts, W. J. Stirling and R. S. Thorne, *Parton distributions and the LHC: W and Zproduction*, Eur. Phys. J. C **14**, 133–145 (2000). 3.2

[Nam60] Y. Nambu, *Axial Vector Current Conservation in Weak Interactions*, Phys. Rev. Lett. **4**(7), 380–382 (Apr 1960). 2.2.1

[Pau30] W. Pauli, W. Pauli's letter to the Radioactive Ladies and Gentlemen., 1930. 2.1

[PDG06] PDG (Particle Data Group Collaboration), *Review of Particle Physics*, Journal of Physics G **33**, 1+ (2006). 2.25, 2.26, 2.27, 2.29, 2.2.3, 3.1, 6.6

[Pet] T. C. Petersen, private communication with Troels C. Petersen. 7.1

[S+57] E. C. G. Sudarshan et al., The Nature of the Four-Fermion Interaction, Proc. of the Conference on Mesons and Newly-Discovered Particles, Padua-Venice, Sep 1957. 2.1.1

[Sjo] T. Sjostrand, *PYTHIA*, http://www.thep.lu.se/∼torbjorn/Pythia.html. 5.8.1

[SMS06] T. Sjostrand, S. Mrenna and P. Skands, *PYTHIA 6.4 Physics and Manual*, J. High Energy Phys. **0605**, 026 (2006), http://arxiv.org/abs/hep-ph/0603175. 5

[SvNV83] J. Smith, W. L. van Neerven and J. A. M. Vermaseren, *Transverse Mass and Width of the W Boson*, Phys. Rev. Lett. **50**(22), 1738–1740 (May 1983). 3.2

[TDR97] TDR (The ATLAS Inner Detector Community, CERN Collaboration), *Inner Detector – Technical Design Report*, volume I, The ATLAS Inner Detector Community, CERN, 30 April 1997. 5, 5.4, 6

[TDR99a] TDR (The ATLAS Collaboration, CERN Collaboration), *ATLAS detector and physics performance – Technical Design Report*, volume II, The ATLAS Collaboration, CERN, 25 May 1999. 2.2.3, 3.2

[TDR99b] TDR (The ATLAS Collaboration, CERN Collaboration), *ATLAS detector and physics performance – Technical Design Report*, volume I, The ATLAS Collaboration, CERN, 25 May 1999. 3.2, 4.1, 4.2, 5, 5.2, 5.8, 5.9

[TKTB01] R. M. Thurman-Keup, A. V. Kotwal, M. Tecchio and A. Byon-Wagner, *W boson physics at hadron colliders*, Rev. Mod. Phys. **73**(2), 267–306 (Apr 2001). 2.2.3, 2.2.3

[UA183] *Experimental observation of isolated large transverse energy electrons with associated missing energy at* $\sqrt{s} = 540GeV$, Phys. Lett. B **122**, 103–116 (1983). 2.2.3

[UA283] *Observation of single isolated electrons of high transverse momentum in events with missing transverse energy at the CERN* $\bar{p}p$ *collider*, Phys. Lett. B **122**, 476–485 (1983). 2.2.3

[W+57] C. Wu et al., Phys. Rev. **105**, 1413–1415 (1957). 2.1.1

[Wei67] S. Weinberg, Phys. Rev. Lett. **19(21)**, 1264–1266 (1967). 2.2.3

Index

Part IV

Appendix

Appendix A

The Standard Model

$$\sigma_1 = \begin{pmatrix} 0 & 1 \\ 1 & 0 \end{pmatrix} \qquad \sigma_2 = \begin{pmatrix} 0 & -i \\ i & 0 \end{pmatrix} \qquad \sigma_3 = \begin{pmatrix} 1 & 0 \\ 0 & -1 \end{pmatrix} \qquad \sigma_\pm = \tfrac{1}{2}(\sigma_1 \pm i\sigma_2)$$

Table A.1: The Pauli matrices $\sigma_i, i = 1, 2, 3$ and the *step-up* and *step-down* operators $\sigma_\pm$.

$$\Phi' = U(\xi)\Phi = \begin{pmatrix} 0 \\ \frac{v+H(x)}{\sqrt{2}} \end{pmatrix} \quad , \quad U(\xi) = e^{i\frac{\boldsymbol{\xi}\cdot\boldsymbol{\sigma}}{v}} \tag{A.1}$$

$$l'_L = U(\xi) l_L \quad , \quad e'_R = e_R \quad , \quad q'_L = U(\xi) q_L \quad , \quad u'_R = u_R \quad , \quad d'_R = d_R \tag{A.2}$$

$$\left(\frac{\boldsymbol{\sigma}\cdot\mathbf{W}'_\mu}{2}\right) = U(\xi)\left(\frac{\boldsymbol{\sigma}\cdot\mathbf{W}_\mu}{2}\right)U^{-1}(\xi) - \frac{i}{g}\left(\partial_\mu U(\xi)\right)U^{-1}(\xi) \quad , \quad B'_\mu = B_\mu \tag{A.3}$$

$$\frac{\sigma_{NC}(\nu q \to \nu q)}{\sigma_{CC}(\nu q \to l q')} \sim f\left(\sin^2\theta_w\right) \tag{A.4}$$

Appendix B

Analysis on Combined Test Beam

B.1 Tables

Name	Corresponding variable(s) in the CBNT
Cher	`Cher2`
	in TileRec/h1000 tree
EMF1	`cl_eemb1_tb_em[0]`
	normalised by the beam energy
HadF	`cl_etileb0_topo[0]+cl_etileb1_topo[0]+cl_etileb2_topo[0]`
	normalised by the beam energy
LArF	`cl_eemb0_tb_em[0]+cl_eemb1_tb_em[0]+cl_eemb2_tb_em[0]+cl_eemb3_tb_em[0]`
	normalised by the beam energy
MuTag	`MuTag`
	in TileRec/h1000 tree
StrawID	`10000*(trk_Trt_layer[0][hit]+3*trk_Trt_phisector[0][hit])`
	`+100*trk_Trt_strawlayer[0][hit]+trk_Trt_straw[0][hit]`

Table B.1: Variable names used in this thesis and their corresponding names and calculation in the used data sets (CBNT).

Energy in GeV		2	3	5	9	20	50	80	100	150	180	350
Var.	PID	Cut on variable										
EMF1	$e >$	0.24	0.25	0.26	0.24	0.20	0.18	0.16	0.14	0.13	0.12	0.11
	$\pi <$	0.08	0.10	0.10	0.10	0.08	0.06	0.05	0.05	0.05	0.05	0.05
	$\mu <$	0.10	0.10	0.10	0.05	0.04	0.03	0.02	0.02	0.02	0.02	0.02
LArF	$e >$	0.55	0.62	0.64	0.66	0.70	0.72	0.74	0.77	0.79	0.80	0.82
	$\pi <$	0.45	0.45	0.45	0.45	0.50	0.55	0.60	0.65	0.45	0.40	0.30
	$\mu <$	0.25	0.15	0.12	0.10	0.05	0.03	0.03	0.03	0.03	0.03	0.03
HadF	$e <$	0.03	0.02	0.02	0.01	0.01	0.01	0.01	0.01	0.01	0.008	0.008
	$\pi >$	–	–	–	–	0.01	0.01	0.01	0.01	0.01	0.008	0.008
	$\mu >$	–	–	–	0.15	0.07	0.03	0.02	0.015	0.012	0.008	0.004
	$\mu <$	–	–	–	0.35	0.25	0.12	0.09	0.07	0.06	0.055	0.050
Cher	$e >$	630	635	640	640	640	–	–	–	–	–	–
	$\pi, \mu <$	625	630	635	640	640	–	–	–	–	–	–
MuTag	$e, \pi <$	460	460	460	460	460	460	460	460	460	460	460
	$\mu >$	480	480	480	480	480	480	480	480	480	480	480

Table B.2: Non-TRT separation variable cut values. Shown are the cut values for the different non-TRT separation variables and particle types at each energy. They are obtained iteratively, and aim for purities better than 0.2%.

Variable	Energy in GeV								
	2	3	5	9	20	50	80	100	180
ε^{π} EMF1	0.895	0.926	0.908	0.986	0.927	0.844	0.813	0.868	0.933
ε^{π} LArF	0.934	0.927	0.935	0.980	0.946	0.966	0.981	0.994	0.958
ε^{π} HadF	1.000	1.000	1.000	0.583	0.808	0.881	0.887	0.949	0.975
ε^{π} Cher	0.554	0.797	0.939	0.988	0.929	1.000	1.000	1.000	1.000
β_e EMF1	0.007	0.008	0.005	0.000	0.003	0.007	0.012	0.016	0.002
β_e LArF	0.031	0.018	0.015	0.002	0.010	0.006	0.005	0.002	0.001
β_e HadF	0.591	0.607	0.537	0.417	0.192	0.119	0.113	0.051	0.025
β_e Cher	0.435	0.196	0.057	0.012	0.071	1.000	1.000	1.000	1.000
ε^{e} EMF1	0.937	0.954	0.938	0.910	0.957	0.921	0.892	0.932	0.842
ε^{e} LArF	0.955	0.939	0.942	0.894	0.995	0.989	0.995	0.994	0.960
ε^{e} HadF	0.967	0.983	0.994	0.998	0.998	0.997	0.998	0.996	0.982
ε^{e} Cher	0.930	0.926	0.915	0.898	0.920	1.000	1.000	1.000	1.000
β_{π} EMF1	0.004	0.004	0.003	0.004	0.002	0.002	0.002	0.002	0.004
β_{π} LArF	0.010	0.005	0.001	0.001	0.001	0.002	0.001	0.002	0.003
β_{π} HadF	1.000	1.000	1.000	0.002	0.002	0.003	0.002	0.004	0.018
β_{π} Cher	0.059	0.064	0.076	0.100	0.079	1.000	1.000	1.000	1.000
e purity (10^{-6})	8.43	2.07	0.15	0.00	0.00	0.05	0.02	0.03	0.03
π purity (10^{-6})	17.13	9.53	4.07	0.01	0.04	1.39	1.91	0.95	0.24

Table B.3: Signal and background efficiencies for the non-TRT separation variable cuts. The numbers are calculated from cutting on all other variables than the one in question. The two bottom rows show the purity of the electron and pion samples, if there were no correlations between the variables.

Variables	EMF1	LArF	HadF	Cher	MuTag
			Pions		
EMF1	–	0.30-0.48	-0.27-0.08	-0.02-0.02	-0.02-0.02
LArF		–	-0.58-0.07	-0.04-0.02	-0.01-0.01
HadF			–	-0.04-0.01	-0.02-0.00
Cher				–	-0.45- -0.34
MuTag					–
			Electrons		
EMF1	–	0.08-0.50	-0.08-0.02	-0.02-0.02	-0.01-0.01
LArF		–	-0.11-0.02	0.00-0.05	-0.04-0.04
HadF			–	-0.01-0.01	-0.02-0.01
Cher				–	-0.06- -0.01
MuTag					–

Table B.4: Non-TRT separation variables linear correlation. In general the uncertainty is 0.02.

E (GeV)	2	3	5	9	20	50	80	100	180
e	-0.03	-0.03	-0.02	-0.03	0.06	0.11	0.12	0.18	0.26
π	0.21	0.08	0.04	0.04	0.02	0.06	0.07	0.08	0.13

Table B.5: Linear correlation factors between p_{HT} and p_{ToT} for pions and electrons.

B.2 Distributions at 2 GeV

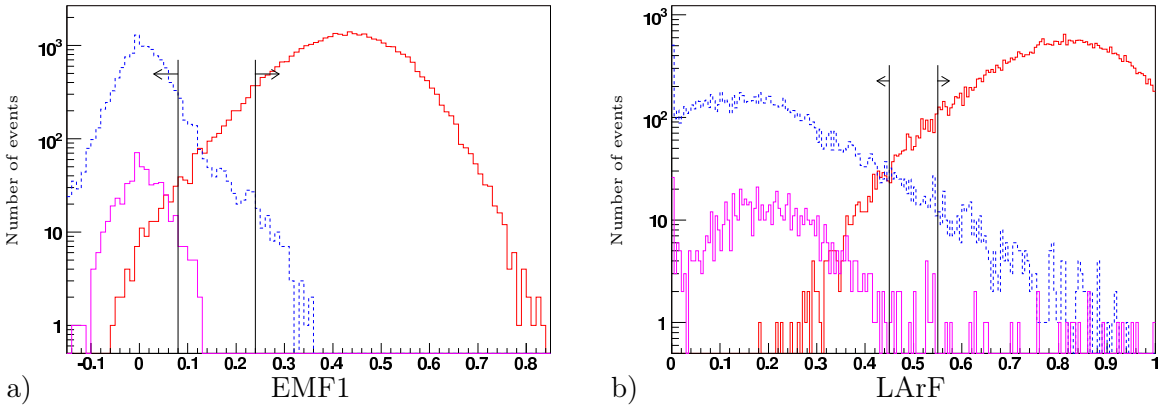

a) b)

Figure B.1: Distribution of the fraction of energy deposited a) in the first sampling (EMF1) and b) the entire cluster (LArF) in the Liquid Argon calorimeter at 2 GeV. Each curve is obtained by applying cuts to the three other separation variables. The cuts on the variable shown are indicated with vertical lines and arrows. [π: dashed blue, e: solid red, μ: solid violet]

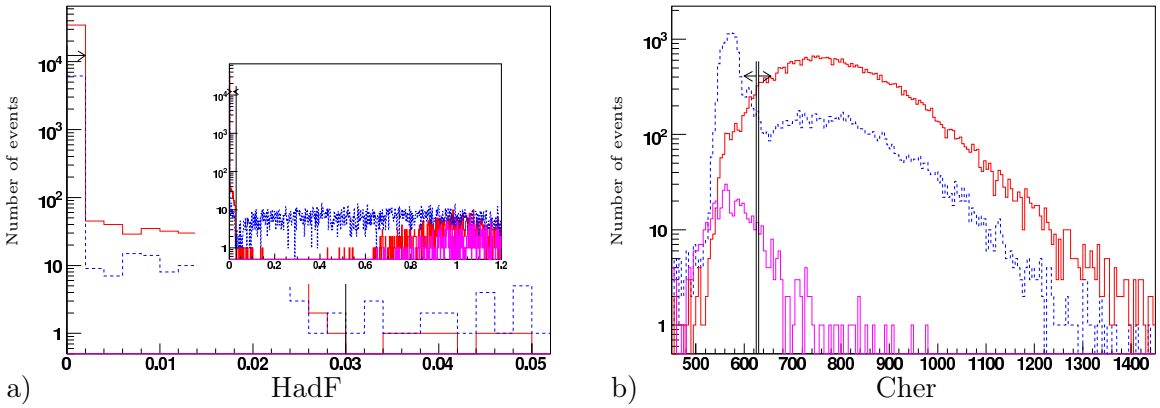

a) b)

Figure B.2: Distribution of a) the energy fraction in the Tile calorimeter (HadF) and b) the Cherenkov variable (Cher) at 2 GeV. Each curve is obtained by applying cuts to the three other separation variables. The cuts on the variable shown are indicated with vertical lines and arrows. [π: dashed blue, e: solid red, μ: solid violet]

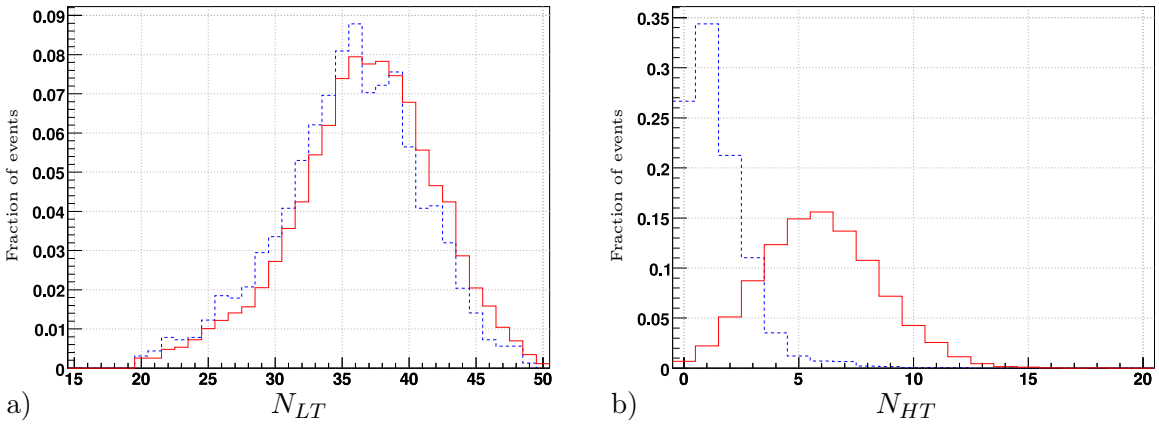

a) b)

Figure B.3: Distribution of number of LT and HT hits on tracks at 2 GeV. a) Number of LT hits on track, b) Number of HT hits on track [π: dashed blue, e: solid red]

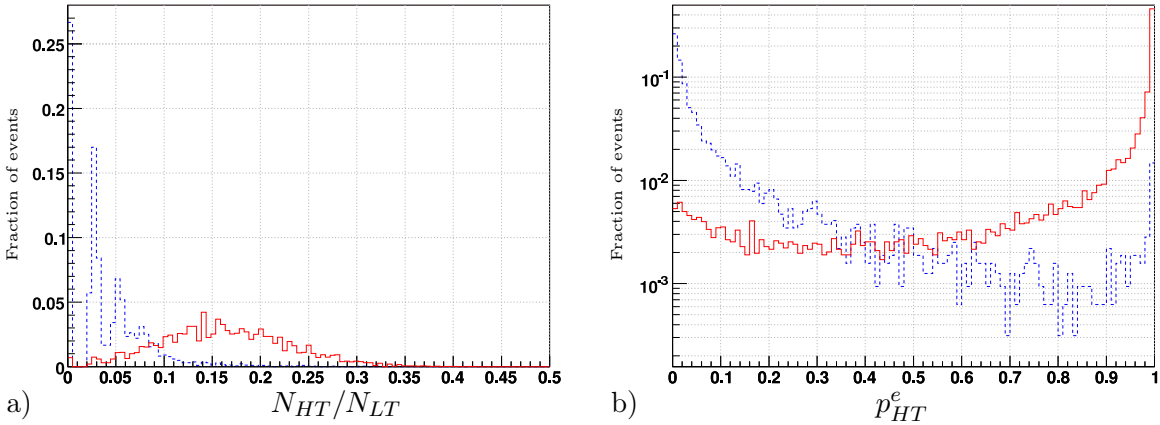

a) b)

Figure B.4: Distribution of a) N_{HT}/N_{LT} and b) likelihood variable using the HT information for electrons and pions at 2 GeV. [π: dashed blue, e: solid red]

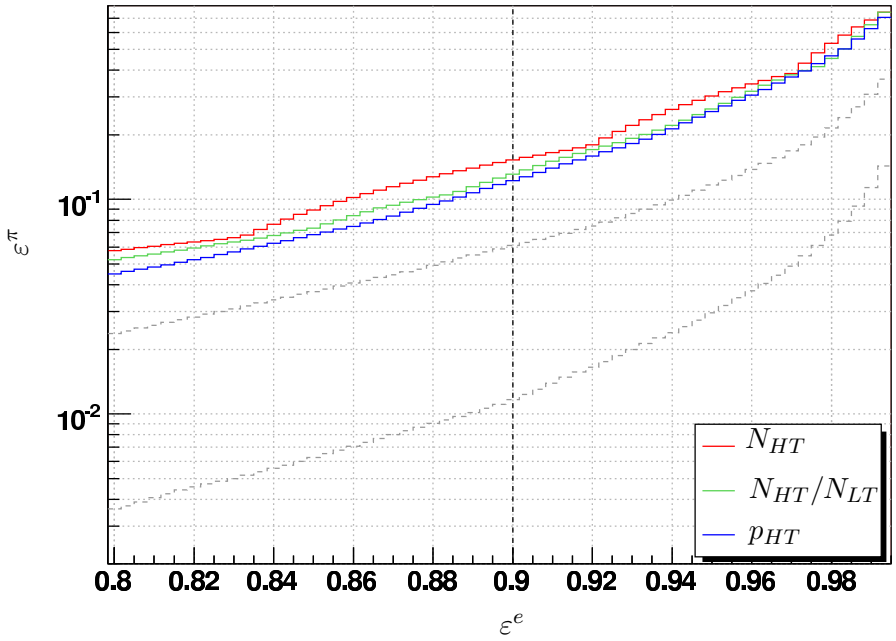

Figure B.5: π-efficiency over e-efficiency for HT methods at 2 GeV. The grey lines represent 2 and 2.5σ separation.

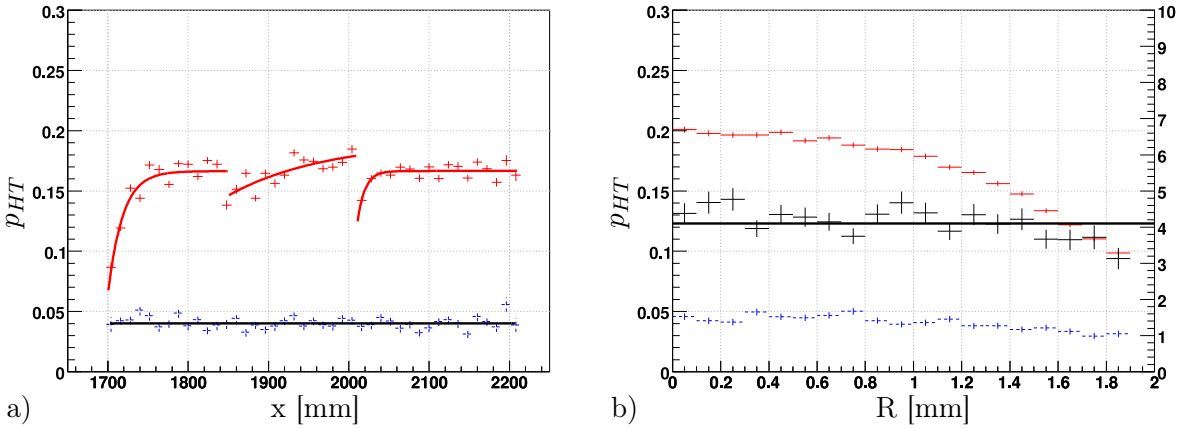

Figure B.6: Geometric dependency of the HT probability at 2 GeV, a) as a function of x (depth in the detector). $\frac{\chi^2}{N_{Dof}}(e) = \frac{123.6}{10}, \frac{74.5}{10}, \frac{37.6}{14}$. $\frac{\chi^2}{N_{Dof}}(\pi) = \frac{61.4}{42}$. b) as a function of R (distance track-anode). $\frac{\chi^2}{N_{Dof}}(\pi) = \frac{38.4}{18}$. [$\pi$: dashed blue, e: solid red, ratio between e and π: black]

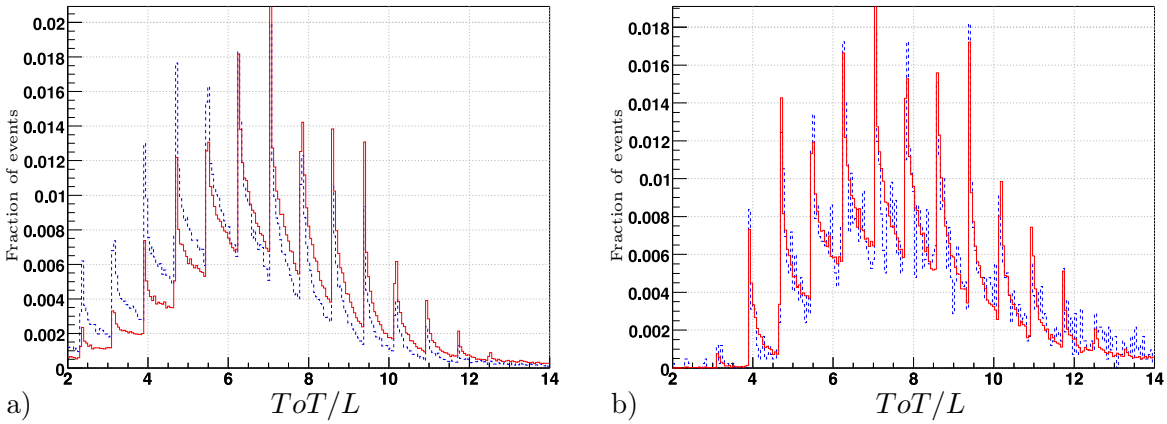

Figure B.7: ToT normalised by the length the track traversed through the straw for straws a) without and b) with a HT hit for electrons and pions at 2 GeV. As can be seen, the straws with a HT hit does not carry any more separation power in the ToT variable (i.e. the electron and pion curves are the same). The jagged structure is due to the discrete ToT values. [π: dashed blue, e: solid red]

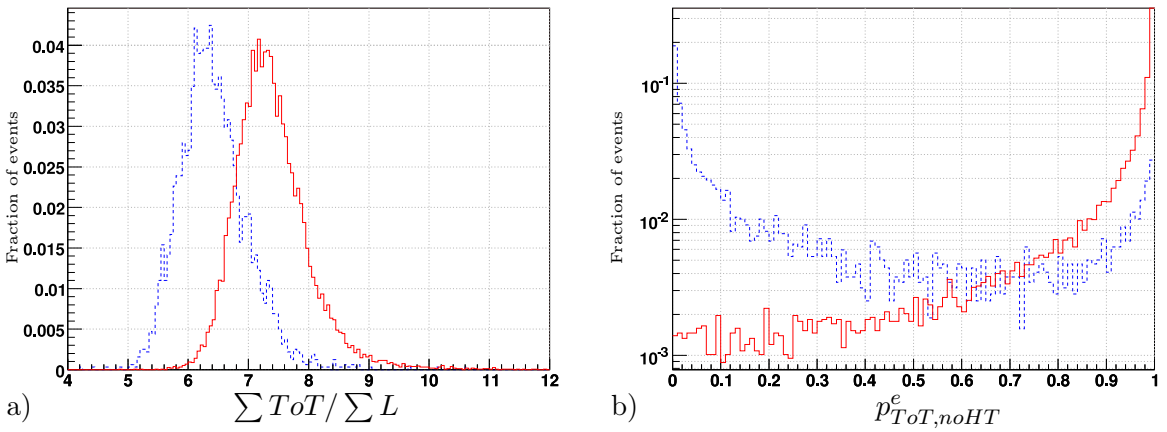

Figure B.8: a) ToT sum of all hits on track normalised by the sum of all L (length of track in straw), and b) probability for being an electron using a HT likelihood method for electrons and pions at 2 GeV. [π: dashed blue, e: solid red]

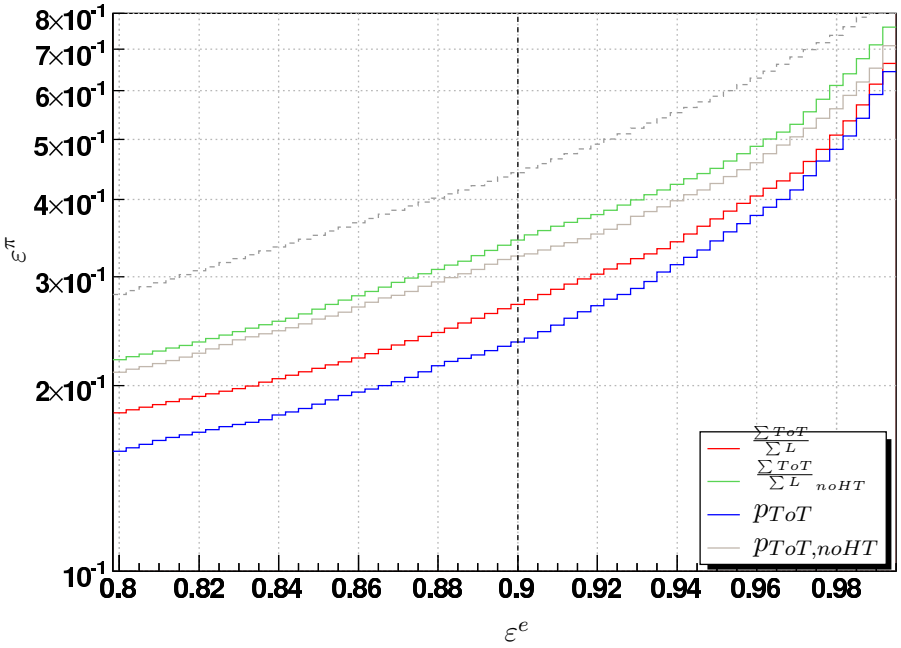

Figure B.9: π-efficiency over e-efficiency for ToT methods at 2 GeV. The grey line represents 1σ separation.

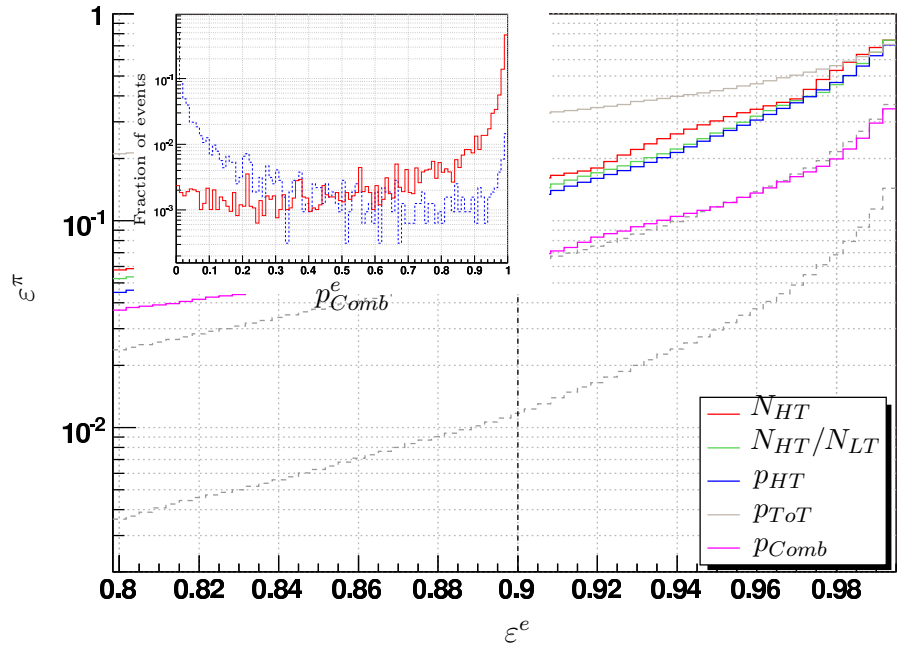

Figure B.10: Distribution of the p^{e}_{Comb} (insert) and π-efficiency over e-efficiency plot for all methods at 2 GeV. The grey lines represent 2 and 2.5σ separation.

B.3 Distributions at 180 GeV

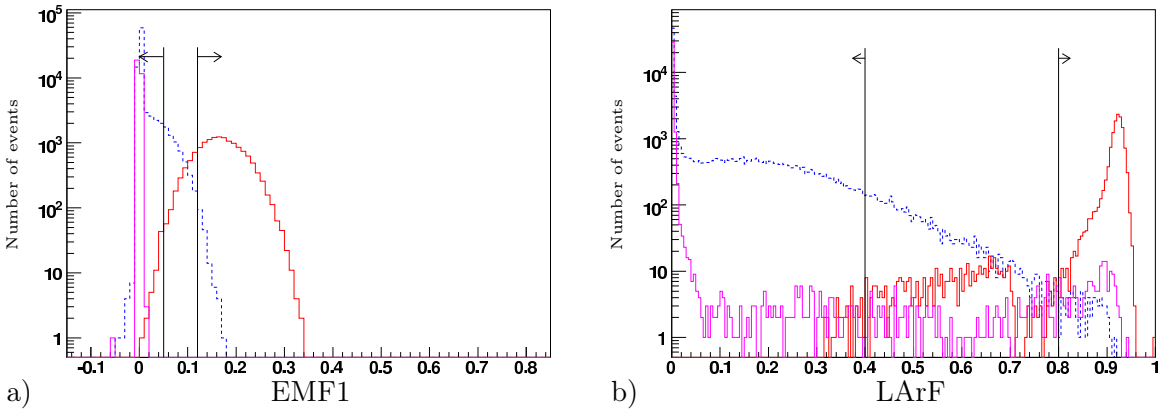

Figure B.11: Distribution of the fraction of energy deposited a) in the first sampling (EMF1) and b) the entire cluster (LArF) in the Liquid Argon calorimeter at 180 GeV. Each curve is obtained by applying cuts to the three other separation variables. The cuts on the variable shown are indicated with vertical lines and arrows. [π: dashed blue, e: solid red, μ: solid violet]

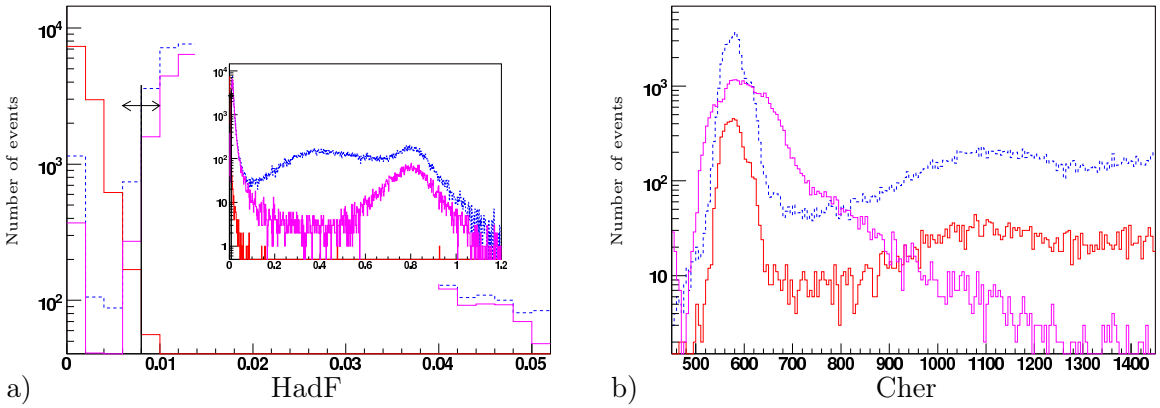

Figure B.12: Distribution of a) the energy fraction in the Tile calorimeter (HadF) and b) the Cherenkov variable (Cher) at 180 GeV. Each curve is obtained by applying cuts to the three other separation variables. The cuts on the variable shown are indicated with vertical lines and arrows. [π: dashed blue, e: solid red, μ: solid violet]

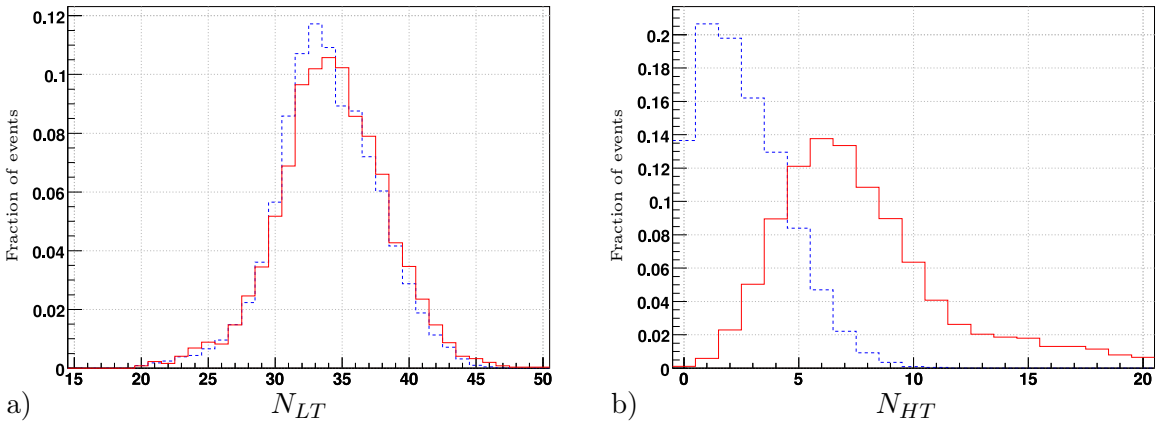

Figure B.13: Distribution of number of LT and HT hits on tracks at 180 GeV. a) Number of LT hits on track, b) Number of HT hits on track [π: dashed blue, e: solid red]

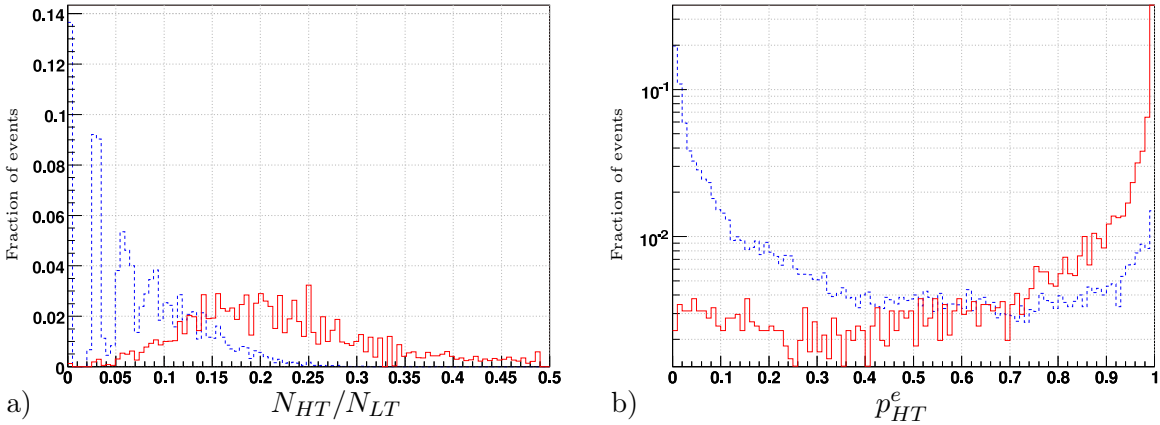

Figure B.14: Distribution of a) N_{HT}/N_{LT} and b) likelihood variable using the HT information for electrons and pions at 180 GeV. [π: dashed blue, e: solid red]

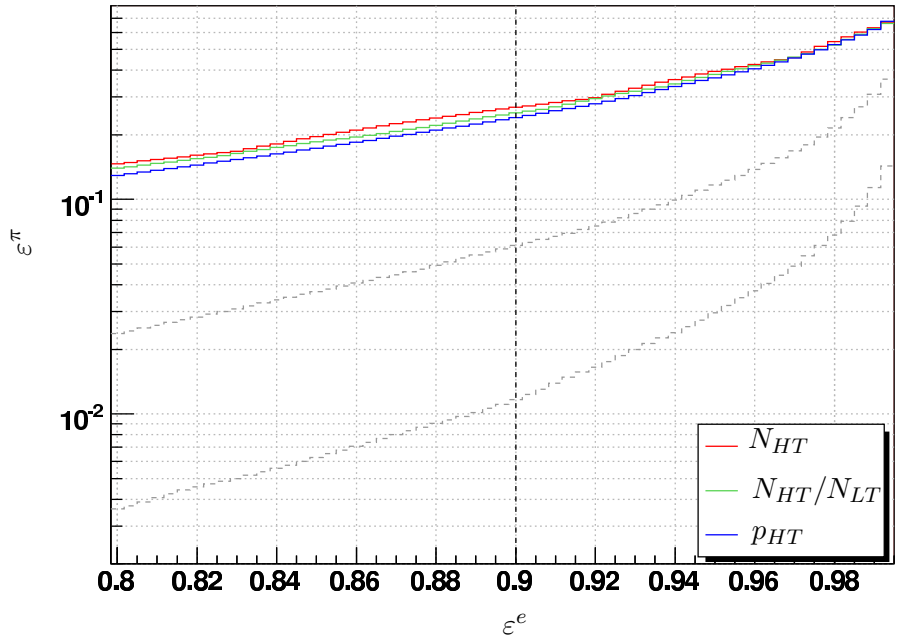

Figure B.15: π-efficiency over e-efficiency for HT methods at 180 GeV. The grey lines represent 2 and 2.5σ separation.

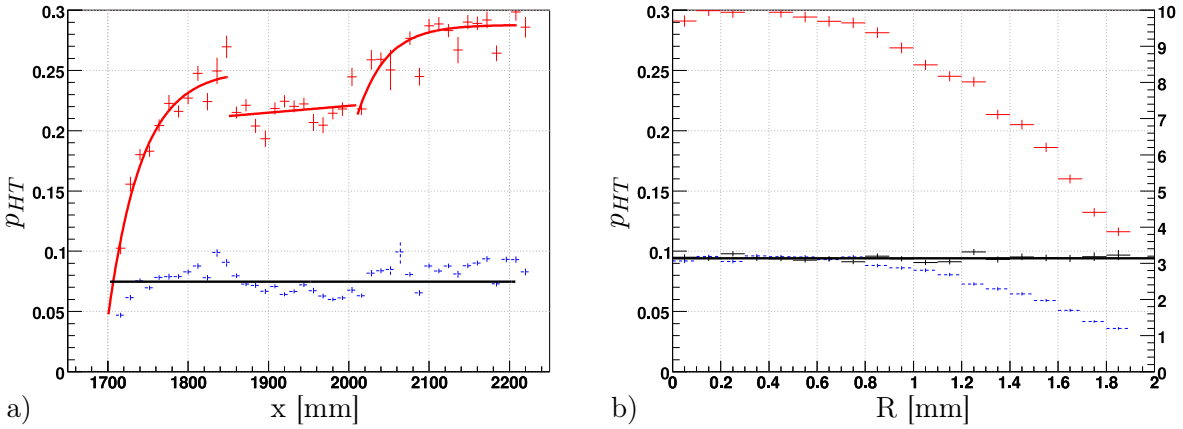

Figure B.16: Geometric dependency of the HT probability at 180 GeV, a) as a function of x (depth in the detector). $\frac{\chi^2}{N_{Dof}}(e) = \frac{33.0}{9}, \frac{38.3}{10}, \frac{53.8}{14}$. $\frac{\chi^2}{N_{Dof}}(\pi) = \frac{1205.1}{41}$. b) as a function of R (distance track-anode). $\frac{\chi^2}{N_{Dof}}(\pi) = \frac{15.4}{18}$. [$\pi$: dashed blue, e: solid red, ratio between e and π: black]

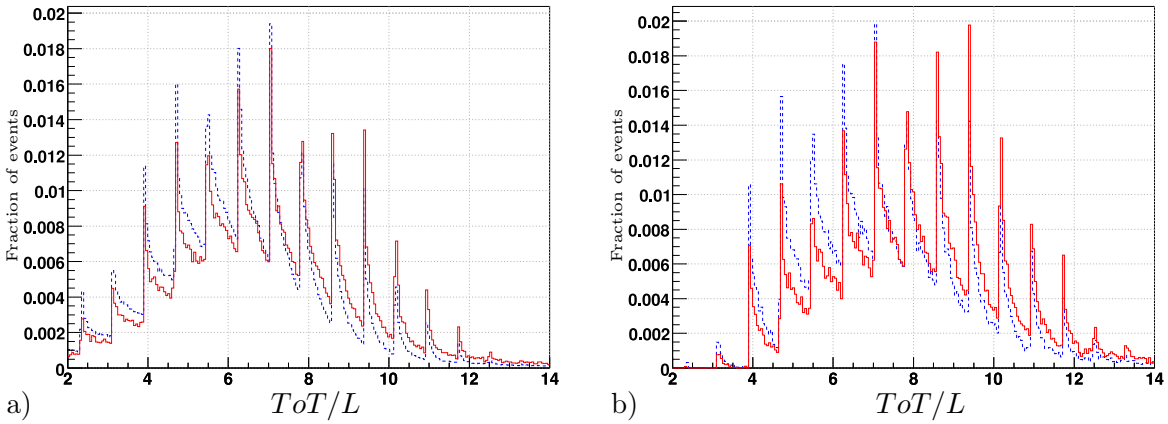

Figure B.17: ToT normalised by the length the track traversed through the straw for straws a) without and b) with a HT hit for electrons and pions at 180 GeV. As can be seen, the straws with a HT hit does not carry any more separation power in the ToT variable (i.e. the electron and pion curves are the same). The jagged structure is due to the discrete ToT values. [π: dashed blue, e: solid red]

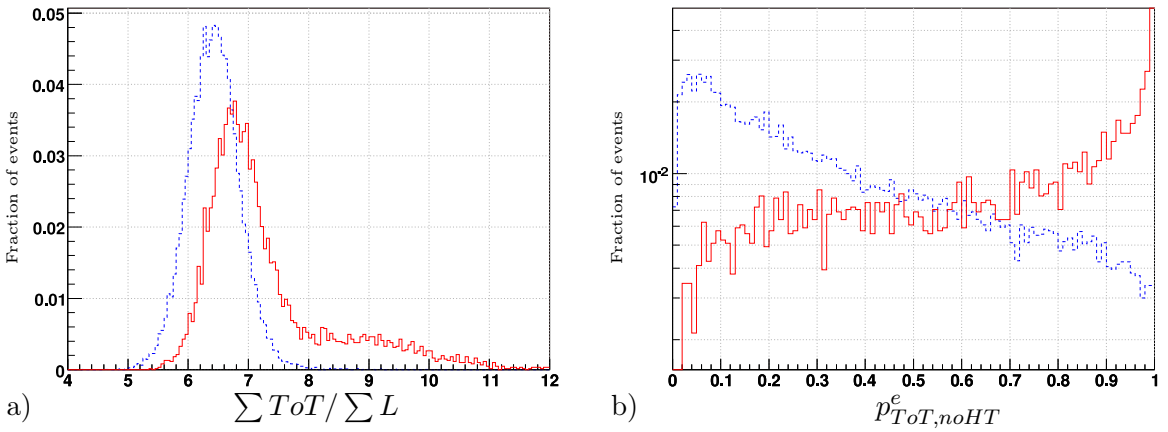

Figure B.18: a) ToT sum of all hits on track normalised by the sum of all L (length of track in straw), and b) probability for being an electron using a HT likelihood method for electrons and pions at 180 GeV. [π: dashed blue, e: solid red]

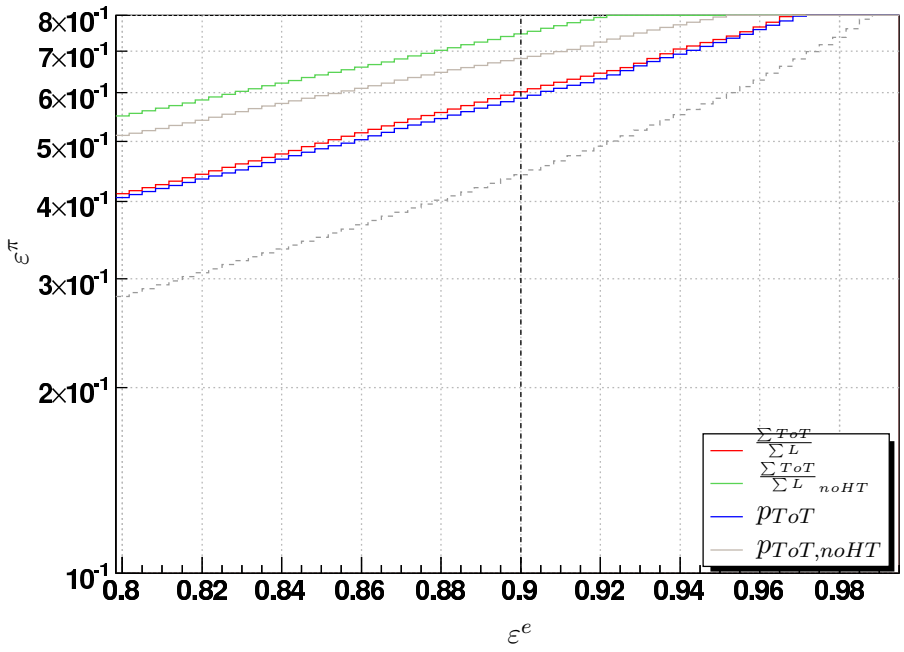

Figure B.19: π-efficiency over e-efficiency for ToT methods at 180 GeV. The grey line represents 1σ separation.

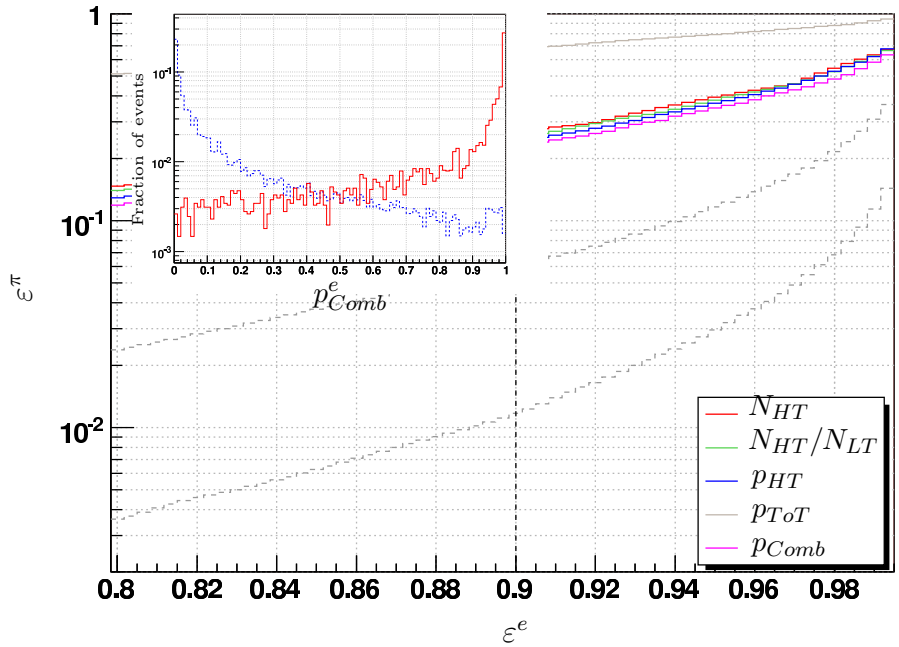

Figure B.20: Distribution of the p^{e}_{Comb} (insert) and π-efficiency over e-efficiency plot for all methods at 180 GeV. The grey lines represent 2 and 2.5σ separation.

Appendix C

Analysis of the ATLAS W Boson Mass Measurement Potential

C.1 Comparison of PHOTOS Environments

The purpose of this small study was to validate the ATLFAST/PHOTOS as well as the ATHENA/PHOTOS environments, used for the fast and full simulation, respectively. The former one, provided by M. Boonekamp, has been checked [Boo] against values provided by the PHOTOS authors [GW] and was found to agree well. In the test th fraction of events, containing zero, one and two or more FSR photons above a certain threshold were counted. The "one-photon event" will have to have one (and only one) photon of energy larger than the threshold. If there are more than one such photons, the event is of the "two-photon" type. In case there are more than two photons of energy larger than the threshold, then only the two most energetic photons are considered, and the remaining ones are treated as if they did not pass the threshold. All test were carried out in the exponentiated mode of PHOTOS for $Z \to \mu\mu$ and $W^+ \to \mu\nu$ events, using a threshold of 10 GeV (see [GW] for details).
In a second step, a similar comparison was performed between the ATLFAST/PHOTOS and the ATHENA/PHOTOS environment, again in exponentiated mode, but applying the standard selection of parameters used for the full simulation. In this case the only restriction on the energy of the photons is given by the XPHCUT variable, describing the fraction of the lepton energy, the photons can take. In the exponetiated mode this is set to 10^{-7}. After first test these numbers do not agree to full extend, therefore a further investigation of this needed, and ongoing. The fractions of events with a certain number of FSR photons N_{FSR}, for each event type and order, obtained from the ATLFAST/PHOTOS environment are given in Table C.1.

		N_{FSR}					
Event type	Order	0	1	2	3	4	5
$W \to e\nu$	0^{th}	1.000	-	-	-	-	-
	1^{st}	0.839	0.161	-	-	-	-
	2^{nd}	0.862	0.127	0.011	-	-	-
	4^{th}	0.859	0.132	0.009	0.000	0.000	-
	exp	0.477	0.354	0.131	0.032	0.006	0.001
$Z \to ee$	0^{th}	1.000	-	-	-	-	-
	1^{st}	0.921	0.079	-	-	-	-
	2^{nd}	0.925	0.072	0.003	-	-	-
	4^{th}	0.925	0.073	0.003	0.000	0.000	-
	exp	0.682	0.261	0.050	0.006	0.001	0.000
$W \to \mu\nu$	0^{th}	1.000	-	-	-	-	-
	1^{st}	0.813	0.187	-	-	-	-
	2^{nd}	0.845	0.141	0.014	-	-	-
	4^{th}	0.844	0.144	0.011	0.000	0.000	-
	exp	0.456	0.360	0.139	0.036	0.007	0.001
$Z \to \mu\mu$	0^{th}	1.000	-	-	-	-	-
	1^{st}	0.905	0.095	-	-	-	-
	2^{nd}	0.913	0.082	0.004	-	-	-
	4^{th}	0.913	0.083	0.003	0.000	0.000	-
	exp	0.654	0.277	0.060	0.008	0.001	0.000

Table C.1: Table showing, for each event type and order, the fraction of events with a certain number of FSR photons N_{FSR}.